J. Tominaga T. Nakano

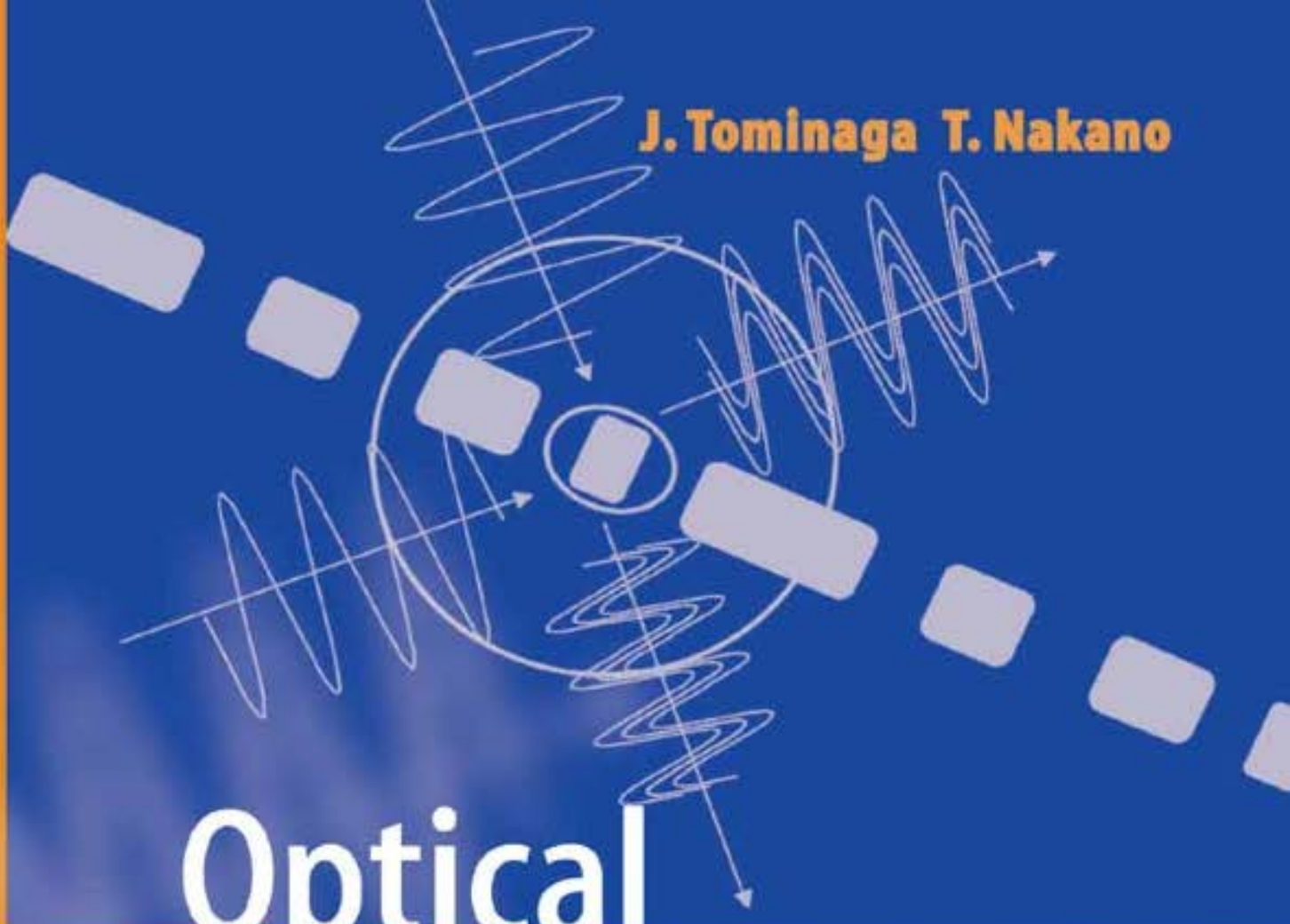

Optical Near-Field Recording

Science and Technology

Springer

Optical Near-Field Recording

J. Tominaga T. Nakano

Optical Near-Field Recording

Science and Technology

With 106 Figures

Springer

Professor Junji Tominaga, Head of Laboratory
Dr. Takashi Nakano
Centre for Applied Near-Field Optics Research (CAN-FOR)
National Institute of Advanced Industrial Science and Technology (AIST)
Tsukuba Central Research No. 4
1-1-1 Higashi, Tsukuba-City, 305-8562 Japan
E-mail: j-tominaga@aist.go.jp

Library of Congress Control Number: 2004107787

ISBN 3-540-22128-X Springer Berlin Heidelberg New York

Springer is a part of Springer Science+Business Media.

springeronline.com

Printed in Germany

Typesetting and prodcution: PTP-Berlin, Protago-TEX-Production GmbH, Berlin
Cover design: *design & production* GmbH, Heidelberg

Printed on acid-free paper SPIN: 10859972 57/3141/YU 5 4 3 2 1 0

Preface

Optical disc industry is one of the successful businesses in the world, and huge amounts of discs and drives have been spread all over the world. More than a billion discs are produced and distributed every year. Since the first optical discs – Laser Discs and Compact Discs (CD) – were shipped in the early 1980s, they have rapidly dominated the world music market, and DVDs will replace the video-tape market in the near future. The optical disc and drive technologies consist of the most advanced and integrated systems with regard to optics, physics, chemistry, mathematics, electronics, mechanics and related subjects; a huge number of scientists and engineers have engaged in the research and development of the systems. One of the key factors of the development of the optical disc systems, of course, results in the availability of cheap, stable, and reliable semiconductor laser units. Now, you can store data up to 4.7 GB on a single side of the 12-cm DVD, and in the near future, blue laser technology will allow storage of more than 20 GB on the same size disc. We should not however forget the other core technologies such as focusing the beam on the surface of a spinning disc precisely, and encoding and decoding digital data. The data capacity of optical discs has increased from 0.65 GB to 25 GB by the year 2003, and we certainly believe it will continue to increase with new technologies. Although the principle of optical recording and readout depends mostly on optics, the technology is now closing to the theoretical limit of the capacity. Focusing a laser beam into a small spot with a diameter as small as 1 µm by the combination of several lenses, the readout head can detect and separate two different marks that are about half the spot size. In a CD, the spot size is 1.0 µm and the minimum mark size is 0.8 µm as determined by a red laser (780-nm wavelength). In a DVD, on the other hand, the spot size is focused by 0.6 µm, and the mark size is approximately 0.4 µm. In a next generation DVD using a blue laser, the spot is further squeezed by 0.3 µm around and the minimum mark is less than 0.2 µm. The available technologies so far depend on the development of new shorter-wavelength semiconductor lasers and sophisticated lenses, also known as "far-field optics." They are, however, closing in on the limit of the resolution due to the diffraction limit.

This book *Science and Technology for Optical Near-Field Recording* discusses the introduction of advanced science and technology to overcome the resolution limit with the help of new technology called "near-field optics."

The optical near-field is a special electromagnetic field that cannot propagate a long distance (unlike optical waves), but trapped very close to an object surface. Such non-propagating field has sometimes been called surface plasmon polaritons or simply surface plasmons. Their existence was discovered in the early 1900s, but its characteristics were not well understood. Their unique properties were not deeply examined until near-field scanning optical microscopes (NSOMs) were designed in the 1980s, thanks to the development of the scanning tunneling microscope (STM) and scanning atomic force microscope (AFM). First application of NSOM to optical recording was carried out in the early 1990s, when the potential for super-storage density was confirmed.

This text book first summarizes in brief several core technologies used in the current CD and DVD optical disc systems in Chap. 2, where the background of optical data storage, several techniques to increase storage densities, and the present limit of the resolution are described. In Chap. 3, the basic principle of optical near-field and surface plasmons, and several methods to generate the fields are explained theoretically and experimentally. Computer-simulated graphics may help your further studies. In Chap. 4, new approaches to realize super-density optical data storage with near-field optics are described. In particular, our discussion is focused on the flying-head system, a specially designed lens system called "solid immersion lens," and a thin-film technique called "Super-RENS." These three novel technologies have been proposed since the 1990s; the techniques are still amateur but the background science and technologies will provide many helpful new ideas in your future studies. In Chap. 5, the other applications of near-field optics and surface plasmons are introduced.

Finally, we wish to thank Dr. Claus Ascheron for supporting our book project. We would like to especially acknowledge: Prof. N. Atoda, who was the former director of advanced optical memory group of National Institute of Interdisciplinary Research (NAIR). We also specially wish to thank to Mr. H. Fuji of Sharp R&D division, and Mr. T. Kikukawa of TDK R&D center for the great support in Chap. 2. Finally, we wish to thank all members of CAN-FOR of AIST: Drs. T. Fukaya, M. Kuwahara, C. Mihalcea (now at Seagate Technology, U.S.A.), D. Büchel (now at Seagate Technology, U.S.A.), J.H. Kim (now at Samsung Electronics, Korea), T. Shima, and Ms. H. Fukuda.

Tsukuba, March 2004

Junji Tominaga
Takashi Nakano

Contents

1 Introduction

Since the first shipment of compact disc (CD) players in 1982, CDs have rapidly spread worldwide. Before the invention of CDs, gramophone discs and music tapes had widely been available as the media for entertainment and recording voice and music broadcast from radio stations. You may remember that you had to take care of the surfaces of the gramophone discs carefully, making sure you do not scratch or damage the surface every time you loaded the records on the player. With CD players, the discs are loaded automatically, and you can enjoy your favorite music randomly and repeatedly without any worries. With recent advances, you can even record your music and make your original CD at home. All these friendly media technologies have become available mostly due to the development of cheap semiconductor lasers as well as advances in integrated optics, precision engineering, mathematics, physics, material science and chemistry. The CD is one of the most technologically advanced inventions that have continued to evolve. Remember that you could not fully use the data capacity of 200 MB in your hard disc (HD) drive in the 1980s for either business or personal use; however, CD, digital versatile disc (DVD), and CD-rewritable (CD-RW) drives were installed in standard models of laptop computers by 2001. If you have a digital camera, you can save your high-quality pictures and easily make your original photo-album with a CD-recordable (CD-R) drive at home. Amazingly, the market price of a copy of CD-R is now less than half a US dollar! You can store more than 200 images and more photos in a CD-R. In the mean time, users have gradually learned by themselves ways to utilize such huge-density media for the last 10 years. For the demands, the scientists and engineers in optical data storage challenged to record 2-hr movies in a CD size disc; this is now available as DVD that has a storage capacity of 4.7 GB. Thanks to the cheap and high-power lasers and shorter-wavelength lasers, optical data storage technology has advanced for the last 20 years. In the near future, new DVDs with a blue laser beam (405 nm) will be widely available. The available data capacity will be increased by more than 20 GB on a single surface, in which 2-hr high-definition TV movies are easily and smoothly stored. Figure 1.1 introduces the history of optical discs from 1982, and it is expected that the optical data storage capacity at the research level is going to reach 100 GB or more in future.

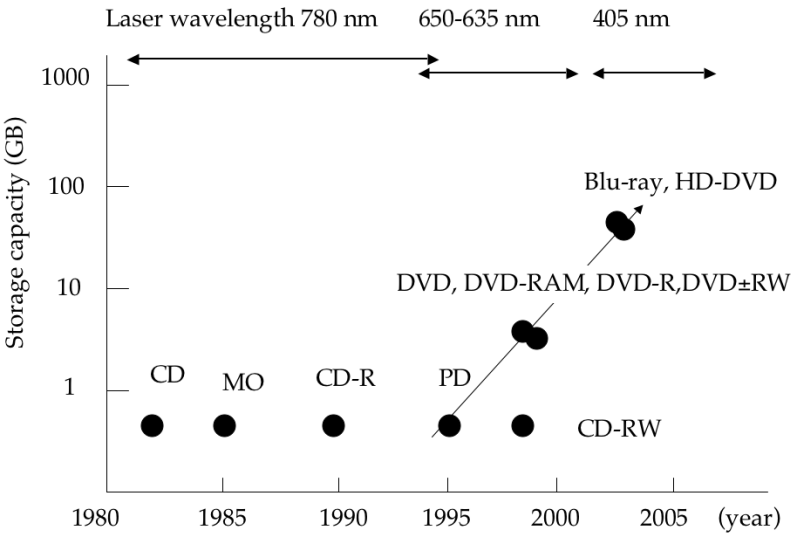

Fig. 1.1. The history of optical data storage after the compact disc (CD) was developed. The top numbers are laser wavelengths used for readout and recording. The term MO represents the disc using magneto-optical recording layer; CD-R using organic dye; and PD, CD-RW, DVD-RAM, DVD-RW using optical phase-change alloys. DVD-9 means the disc consisting of double layered and structure. Blu-ray and HDD are the next generation high-density discs that use blue laser

Optical data storage, especially optical discs, have several advantages over the other data storage media. First, the production cost per byte is very cheap because of molding injection methods. The production time of a CD is less than 5 sec. Second, the discs are all removable and exchangable between all CD or DVD drives available in worldwide (interchangeability is specified among production companies). Third, the access speed is faster than that of tape media, although it is slower than that of HD. However, the optical head has full space to protect the crash to the disc surface: approximately 3 mm. In HD, in contrast, the space is less than 100 nm, which requires very strict control of the flying magnetic head; sometimes the head crash occurs and all or parts of your important data and documents are lost forever. Unfortunately, you cannot remove the disc and exchange to new one by yourself. Back to the optical disc, the recording marks or data pits are safely protected by a thick, plastic cover layer, and the archival life time is better than that of HD. Therefore, CD and DVD families are much more user-friendly. Figure 1.2 shows many different science and technologies used in production.

From the successful story of optical data storage so far, everybody may dream that the optical storage science and technology will easily overwhelm the 100 GB capacity and soon enter the TB region. In reality, however, the optical data storage industry has reached the theoretical and technological

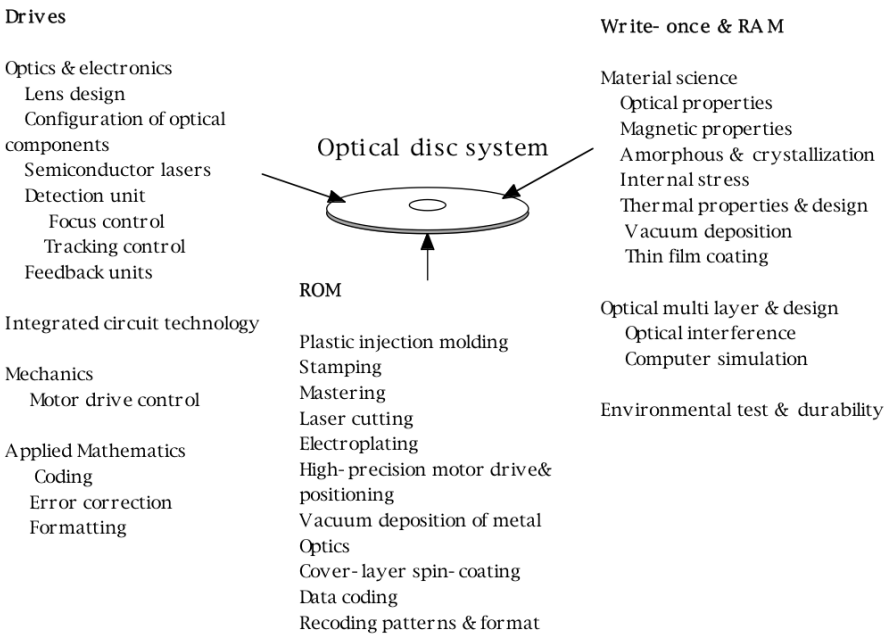

Fig. 1.2. Science and technologies related to optical data storage industry

limitation because of the lack of new technologies using laser unit with an even shorter wavelength ($< 405\,\text{nm}$). The space between the optical head and medium surface is getting narrower and shorter by further increasing the storage density. Unfortunately, optical storage is now exposed to the competition of the other storage systems and the advantages are gradually diminishing. Without new breakthroughs in optical science and technology in the next 5 years, the optical storage industry will cease to advance [1, 2].

In order to overcome the fatal problems in the optical data storage, "near-field optics" and its related application have been proposed for the last decade; several ideas were examined theoretically and experimentally. So, what is "near-field optics" and how is it different form "far-field optics," which is applied to the current optical data storage? How does the near-field play and behave in the optical disc? How can you control the near-field light in data storage? Answering all these questions is the main focus of this book. In the following chapter, you first learn the basic principle of the current optical storage system and the limit of the conventional recording resolution.

2 Summary of Optical Data Storage and the Future Trend

2.1 Resolution Limit and Frequency Characteristics of Optical Storage

An optical disc system requires high-precision readout of recorded pits or marks by a focused laser beam spot. Here, let's consider an optical system consisting of two lenses with the same numerical aperture (NA) and a transparent screen with a sinusoidal pattern as shown in Fig. 2.1. Using the same NA in both lenses, we can assume that a signal obtained behind the second lens is the same as the reflected one observed in front of the first lens. In general, the transmitted screen pattern is not exactly the same as the original and the obtained shape depends on the lens characteristics, after passing through the lens. It is called "optical transfer function" (OTF)" and is a complex function that includes phase information. The square of OTF is called "modulated transfer function" (MTF). OTF is given by a mutual correlated function, but we deal with the self-correlated function in this case because of the same NA used for both lenses. It is simply represented by the frequency characteristics with two circles with a same diameter, as shown in Fig. 2.2. The OTF is thus expressed by a cross section of the two circles mathematically. Here, assuming x_0 as the spatial cut-off frequency, it is

$$H(x) = \frac{2}{\pi}\left\{\cos^{-1}\frac{x}{x_0} - \frac{x}{x_0}\sqrt{1-\left(\frac{x}{x_0}\right)^2}\right\}$$

$$H(x) = 0 \tag{2.1}$$

$$x_0 = 2NA/\lambda \tag{2.2}$$

for $x \leq x_0$ and for $x > x_0$.

If the disc rotation speed is the same as that of the CD ($\nu = 1.25\,\mathrm{m/s}$), the real cut-off frequency is $x_0\nu = 1.44\,\mathrm{MHz}$ by using $\lambda = 780\,\mathrm{nm}$ and $\mathrm{NA} = 0.45$. Therefore, if you apply much higher frequency to the disc readout and recording, no readout signal is observed; this is called the optical diffraction limit. The diffraction limit thus determines the data storage capacity of the disc. This is the fatal issue on developing super-high density optical data storage systems of the next generation.

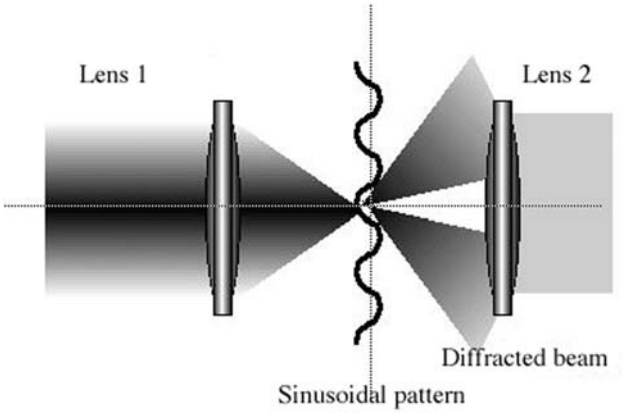

Fig. 2.1. Two lenses with the same NA are placed and the incident beam through the lens 1 is focused on the sinusoidal pattern. The light is diffracted backward (or reflected) and then detected by the lens 2.
Two diffracted angles depend on the sinusoidal pitch, wavelength and NA, finally resulting in the diffraction limit

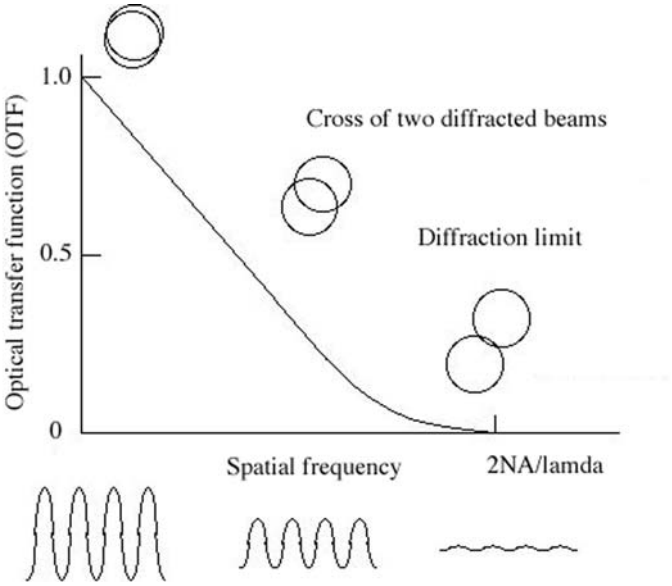

Fig. 2.2. Optical transfer function (OTF) is determined by the two diffracted circle crossing. If the pattern is uniquely flat, two circles are merged.
As the pattern is finer, the diffracted angle is bigger, and then finally they are separated in front of the second lens thus marking the diffraction limit. The finer patterns beyond the diffraction limit are no longer reproduced [3, 4]

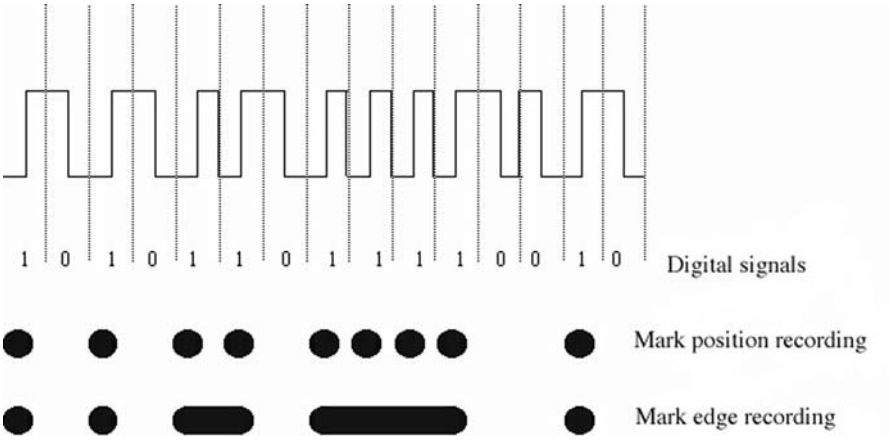

Fig. 2.3. Relationship between digital signals and recording mark patterns using mark position recording and mark edge recording

2.2 Background of Optical Data Storage

In this section, following the background concept of digital recording, we study the basic system of optical storage technologies through a CD system.

2.2.1 Digital Marks and Recording Code

The digital recording in optical data storage seems to be easily understood by corresponding 1 and 0 to a pit and blank, respectively. As shown in Fig. 2.3, for example, when information bits consisting of 101011011110010 are recorded in an optical disc, one may imagine that the pits correspond to 1 and the blanks to 0.

Hence, for example, when a mark comes in a focused laser spot, the signal polarity becomes +; on the other hand, when a blank area comes in, the polarity becomes −. This is the simplest and old digital recording and readout method in optical data storage. However, one may soon notice that the pattern is inconvenient due to the OTF being limited by high frequent response, as shown in Fig. 2.2. In order to reproduce the mark sequences with high OTF, the optical system needs to open a wide time gate to reproduce each pit and blank. If the mark length is short and each mark is placed close together in an internal clock time, it is very hard to discriminate the mark and blank with the high OTF. As a result, the noise and cross-talk increase as well as the time jitter. In order to detect the mark signal in the mark position recording, a slice level is set to the reflection voltage from the pickup unit. Hence, one may select the left or right point at the cross sections. If the mark size is rigidly determined, the time shift between the left point and the reflection peak (the pit center) is always constant. This method is very simple

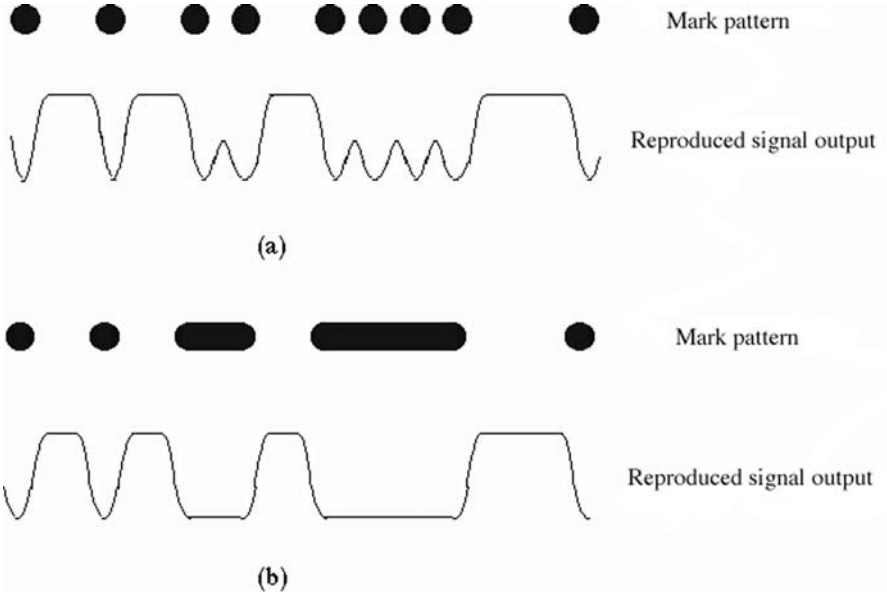

Fig. 2.4. a–b. Recording pit patterns and reproduced optical signals. **a** Mark position recording. **b** Mark edge recording. As the marks are in proximity in **a**, the output OTF becomes small and the mark position recording is not suitable for higher-density recording

but the recording density is not substantially increased by reducing the pit size because of the reduction of the OTF. The mark position recording was used at the early stage of optical data storage but was soon replaced by mark edge recording (Fig. 2.3).

In order to increase recording density, mark edge recording was proposed, and now it has been widely applied in comparison with mark position recording. Each bit is attributed to the transition of reflectivity between a mark and blank. As a mark has two edges in the front and rear, it means that a mark has two bits. Although at a glance, using mark edge recording seems to double the density in comparison with mark position recording, it is not actually true and depends on data coding. To detect the transition point, usually, a double differential method is applied. The differential value at the transition has always a maximum, and evaluating the second differentials gives a parity of + or −. The relationship of the mark edge recording between bit and binary digit is depicted in Fig. 2.4. Besides the two methods, partial response recording is also picked up in optical recording as one of the most advanced technologies.

In optical recording, (2,7) RLL or (1,7) RLL modulation codes is usually used. Here, run-limited length (RLL) determines the minimum and maximum lengths of a series of 0 s. In (2,7) RLL, for example, the minimum run of 0 is

Table 2.1. (2,7) RLL data and code bits

Data	Code bits
10	0100
11	1000
0000	100100
010	001000
011	000100
0010	00001000
0011	00100100

00, and the maximum is 0000000. Therefore, there is no 101 or 1000000001 in (2,7) RLL. On the other hand, a 101 of the code length is allowed in (1,7) RLL. The data and corresponding code bits in (2,7) RLL are summarized in Table 2.1.

In all combinations of code bits in Table 2.1, as you can see, there exists no series of 1000000001 or 101. Assuming a time between each bit as $0.5\,T$, the minimum time detecting the next pit followed by the first pit that passed through the detector is $1.5\,T$, on the other hand, the maximum time length is $4\,T$. When (2,7) RLL code is applied to mark position recording, the time interval detecting a bit is thus set to $\pm T/4$. If a mark is detected successfully in the time interval, the recorded data is reproduced but with light scattering noise and jitter shifted from the clock time. Comparing (1,7) RLL and (2,7) RLL codes, (1,7) RLL is more suitable for high-density recording. As already mentioned, the detection time interval in (2,7) RLL is $T/2$, but $2T/3$ in (1,7) RLL. Thus, the window size is 1.33 times as long as that of (1,7) RLL. In addition, available maximum frequency in (1,7) RLL is $3\,T/8$, while it is $T/3$ in (2,7) RLL. Therefore, the recording code has to be selected and determined, depending on the characteristics of recorded marks, so that the best performance is derived in each system.

When the recorded mark is reproduced by an optical pickup, the output signal is obtained as a reflection of the corresponding voltage from the photo detectors installed in the pickup. Although a series of the mark reflections is transformed by using a recording code, the typical pattern is depicted in Fig. 2.5.

As shown in Fig. 2.5, in the mark position recording with (2,7) RLL code, the minimum length between adjacent marks is limited at $1.5T$. In such a case, the OTF becomes the minimum among the mark combinations, and more detection errors occur in comparison at the other positions. In order to avoid the errors, error correction codes are additionally introduced in a series of the data code, and errors are powerfully corrected under a rigid rule between the correction code and the recording code.

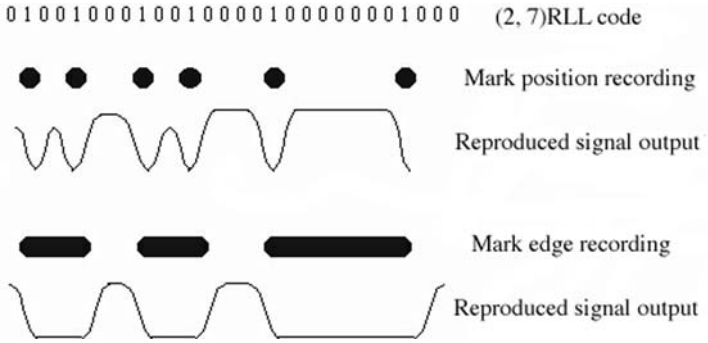

Fig. 2.5. A comparison of (2,7) RLL code recording and its recorded mark patterns with mark position recording and mark edge recording

In general, the quality of an output signal reproduced by an optical pickup is estimated by signal-to-noise ratio (SNR). The signal is the real output voltage with signal and noise usually comes not only from the pickup unit itself, but also from the recording medium. The signal intensity depends on the readout laser power; internal optical loss in the pickup, disc, and recording film; and the sensitivity of the photo detectors. On the other hand, the total noise is mainly due to the laser beam, disc and medium, and the electrical circuit. In addition, the noise from mark jitters, cross talk between adjacent recorded tracks, and servo-errors are also considered. Usually, SNR is estimated in dB scales using SNR = 20 log (signal/noise). Besides SNR, sometimes carrier-to-noise ratio (CNR), the signal intensity ratio at an observing frequency to the noise, is also used. In general, optical data storage systems require SNR > 25 dB or CNR > 40 dB to reproduce the signals with high-quality levels.

2.2.2 Error Correction for Readout

After the recording code is determined and data is recorded in an optical disc, then you have to read out and reproduce the recorded code to the original data by an optical pickup head.

In a CD, for example, the amplitude of an acoustic wave is divided into 16 binary bits ($2^{16} = 65{,}536$) at a sampling frequency of 40 kHz = 25 µs. The acoustic system usually has two channels (L and R), thus the number of digits reproduced in a second is huge and at least equal to

$$40\ (\text{kHz}) \times 16\ (\text{bits}) \times 2\ (\text{channel}) = 1.28 \times 10^6\ \text{bit/s}\,.$$

In addition to the bits, the system needs additional bits for the error corrections and coding. Approximately 2 M bit/s is required altogether. In order to decode from the reproduced signals to the original ones, strong error correction and specific signal modulation systems are necessary. For

Table 2.2. Relationship between α's power and shared binary digits

α 's power	polynominal expression	Shared digits
0	0	0000
1	1	0001
α	α	0010
α^2	α^2	0100
α^3	α^3	1000
α^4	α^3+1	1001
α^5	$\alpha^3+\alpha+1$	1011
α^6	$\alpha^3+\alpha^2+\alpha+1$	1111
α^7	$\alpha^2+\alpha+1$	0111
α^8	$\alpha^3+\alpha^2+\alpha$	1110
α^9	$\alpha^2+\quad 1$	0101
α^{10}	$\alpha^3+\alpha$	1010
α^{11}	$\alpha^3+\alpha^2+1$	1101
α^{12}	$\alpha+1$	0011
α^{13}	$\alpha^2+\alpha$	0110
α^{14}	$\alpha^3+\alpha^2$	1100

example, a long sequence of same binary digits (1111 ... or 00000 ...) sometimes induce tracking errors or miss counting of the digit numbers. As the wave amplitude is divided into 2^{16} numbers, one-digit miscounting may generate fatal errors in the readout because the difference between (0000000000000001) and (0000000000000011) may be small, but the difference between (0000000000000001) and (0100000000000001) is very big! In a CD, an error-correction code called "cross interleaved Reed–Solomon code" (CIRC) is applied to correct random and burst errors efficiently. Instead of dealing with 8-bit CIRC, the 4-bit case (Galois Field 2^4, GF(2^4)) provides more information to illustrate the CIRC's role, and here, we limit our discussion on dealing with $2^4 = 16$ binary numbers against $2^8 = 256$ numbers in a CD.

In CIRC, all the numbers must belong to a closed group in which adding or multiplying two elements will always produce a third element in the group, and the inverse of a number creates another number of the group. In addition, we introduce a polynominal equation $f(x)$ such that

$$f(x) = x^4 + x^3 + 1\,. \tag{2.3}$$

Hence, α is defined as the solution of (2.3). According to Table 2.2 (here, the original element of α is fixed to 0010), all the 4 bits numbers correspond to the polynomials of α [3].

Now, assuming 4 different data strings (A, B, C, and D) each consisting of 4-bit number and additional 2 error-correction 4-bit numbers: the parity (P and Q) and the Reed-Solomon code is defined to satisfy the following two equations:

$$\begin{aligned} A + B + C + D + P + Q &= 0 \\ \alpha^5 A + \alpha^4 B + \alpha^3 C + \alpha^2 D + \alpha P + Q &= 0 \end{aligned}$$

Hence, P and Q are the solutions of the above equations. That is,

$$P = \alpha^{13} A + \alpha^6 B + \alpha^7 C + \alpha^{12} D$$

and

$$Q = \alpha^7 A + \alpha^8 B + \alpha^{13} C + \alpha D\,.$$

The calculation is done by Mod (2).

Now, we deal with 4-bit sequential data: $ABCDPQ$ and then reproduce them optically, for example. Assuming that the reproduced data contain errors somewhere in A, B, C, D, P or Q, we label the reproduced data as A', B', C', D', P', and Q' because we do not identify which 4-bit data include errors. The summations above are then represented by S_1 and S_2:

$$S_1 = A' + B' + C' + D' + P'' + Q'$$

and

$$S_2 = \alpha^5 A' + \alpha^4 B' + \alpha^3 C' + \alpha^2 D' + \alpha P' + Q'\,.$$

If the optical pickup successfully reproduces all the signals, then of course $S_1 = 0$ and $S_2 = 0$. However, if the reproduced data include errors, S_1 and S_2 are not equal to 0. Now, we assume each error pattern is represented by E_i ($i = A$, B, C, D, P and Q) such that S_1 and S_2 can be written as

$$\begin{aligned} S_1 &= A' + B' + C' + D' + P' + Q' \\ &= (A + E_A) + (B + E_B) + (C + E_C) + (D + E_D) \\ &\qquad +(P + E_P) + (Q + E_Q) \\ &= E_A + E_B + E_C + E_D + E_P + E_Q \end{aligned}$$

and

$$\begin{aligned} S_2 &= \alpha^5 A' + \alpha^4 B' + \alpha^3 C' + \alpha^2 D' + \alpha P' + Q' \\ &= \alpha^5 (A + E_A) + \alpha^4 (B + E_B) + \alpha^3 (C + E_C) \\ &\qquad +\alpha^2 (D + E_D) + \alpha (P + E_P) + (Q + E_Q) \\ &= \alpha^5 E_A + \alpha^4 E_B + \alpha^3 E_C + \alpha^2 E_D + \alpha E_P + E_Q\,. \end{aligned}$$

Here, 6 different cases where errors in A' to Q' are considered and separated into,

(1) A' has errors: $S_1 = E_A$, $S_2 = \alpha^5 E_A$, thus, $S_2 = \alpha^5 S_1$
(2) B' has errors: $S_1 = E_B$, $S_2 = \alpha^4 E_B$, thus, $S_2 = \alpha^4 S_1$
(3) C' has errors: $S_1 = E_C$, $S_2 = \alpha^3 E_C$, thus, $S_2 = \alpha^3 S_1$
(4) D' has errors: $S_1 = E_D$, $S_2 = \alpha^2 E_D$, thus, $S_2 = \alpha^2 S_1$
(5) P' has errors: $S_1 = E_P$, $S_2 = \alpha E_P$, thus, $S_2 = \alpha S_1$
(6) Q' has errors: $S_1 = E_Q$, $S_2 = E_Q$, thus, $S_2 = S_1$

Let's try an example with $A = (1001)$, $B = (1001)$, $C = (0010)$, and $D = (1110)$, then $P = (1011)$ and $Q = (0111)$ obtained from Table 2.2. We assume the recorded data is 1001 1001 0010 1110 1011 0111. But if the reproduced data consists of 1001 1011 0010 1110 1011 0111 sequences, then

$$S_1 = \alpha^4 + \alpha^5 + \alpha + \alpha^8 + \alpha^5 + \alpha^7 = \alpha$$

and

$$S_2 = \alpha^5\alpha^4 + \alpha^4\alpha^5 + \alpha^3\alpha + \alpha^2\alpha^8 + \alpha\alpha^5 + \alpha^7 = \alpha^3 + \alpha + 1 = \alpha^5 .$$

Thus, $S_2 = \alpha^4 S_1$. This is the case (2) and $E_B = S_1 = \alpha^5$. Accordingly, B' must be corrected as $B' + E_B = \alpha^5 + \alpha = \alpha^3 + 1 = \alpha^4 = (1001)$. Finally, the reproduced signal is corrected. Therefore, in conclusion, as the number of the additional bits for the error correction is increased, more errors can be corrected by the CIRC method. In an actual CIRC of GF(2^8, Table 2.1 is further expanded to α^{254} and 8-bit codes.

So far, we have learned how the digital signals are recorded and reproduced safely by using digital sequences with the error correction. The following case though has higher probabilities of errors; that is for example, 10000000 00000000 00000000 00000000 00100000. Each piece data is reproduced optically by synchronizing the internal clock with the external clock in a CD drive. However, the long sequence of the same digit, 0 or 1, may generate a time difference and miscounting the bit numbers. In order to avoid such a situation, each 8-bit signal is matched to 256 patterns without long sequences of the same bit by using 14 bits as shown in Table 2.2. This is called "eight to fourteen modulation" (EFM). In addition, 3 different digits – (000), (010), and (001) –, are used at each connection of the 14 bits. As shown in Fig. 2.6, the CD signal has + and − parity. The parity is exchanged at 1 and held at 0. Using the connection codes, three different patterns are considered, but one of them is selected to reduce the total parities to the minimum by the next connection. In EFM, the minimum bit, $T_{\min}$ (or $3\,T$) consists of 1001, and the maximum $T_{\max}$ ($11\,T$) of 100000000001. No longer or shorter bit is allowed in a CD system like the (2,7) RLL code. Therefore, CD pits are constructed of 9 different length pits: $3\,T$, $4\,T$, $5\,T$, $6\,T$, $7\,T$, $8\,T$, $9\,T$, $10\,T$, and finally $11\,T$ against the internal clock.

As shown in Fig. 2.2, the readout signal modulation is described by the MTF function. Increasing the frequency leads to higher density recording and the MTF rapidly decreases and finally reaches 0 at $2\,\mathrm{NA}/\lambda$. In CD family discs, parity changes are detected and transferred into differential impulses.

Table 2.3. Parts of the transition table of EFM

01100100	01000100100010
01100101	00000000100010
01100110	01000000100100
01100111	00100100100010
01101000	01001001000010
01101001	10000001000010
01101010	10010001000010
01101011	10001001000010
01101100	01000001000010
01101101	00000001000010

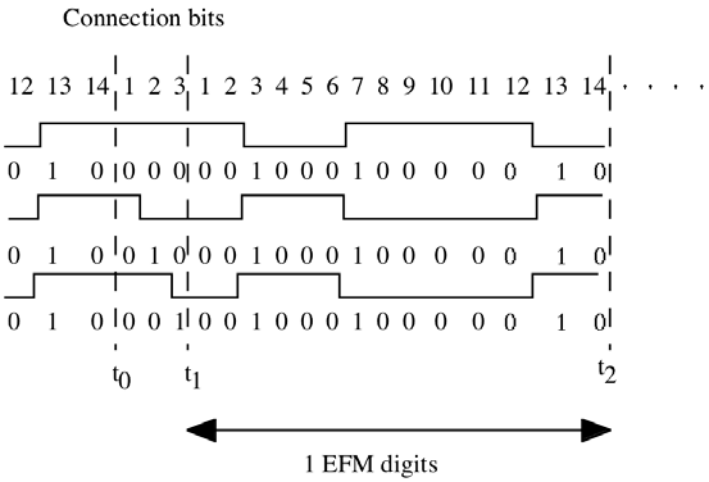

Fig. 2.6. EFM signals and its connection by 3 digits: (000), (100), (010), and (001). In this figure three patterns are allowed and (100) is prohibited because the 10(100) connection takes less time than $T_{\min}$ of the EFM codes

When the impulses are reproduced as the electrical ones, however, they are not transformed as step functions but as functions with slopes due to the Fourier transformation without higher spatial frequencies beyond the diffraction limit. As a result, a series of CD signals are observed as a superimposed signal consisting of $3\,T$ to $11\,T$, and it is called "eye pattern (Fig. 2.7)." Eye pattern and EFM are also common in writable CD (CD-R) and rewritable CD (CD-RW).

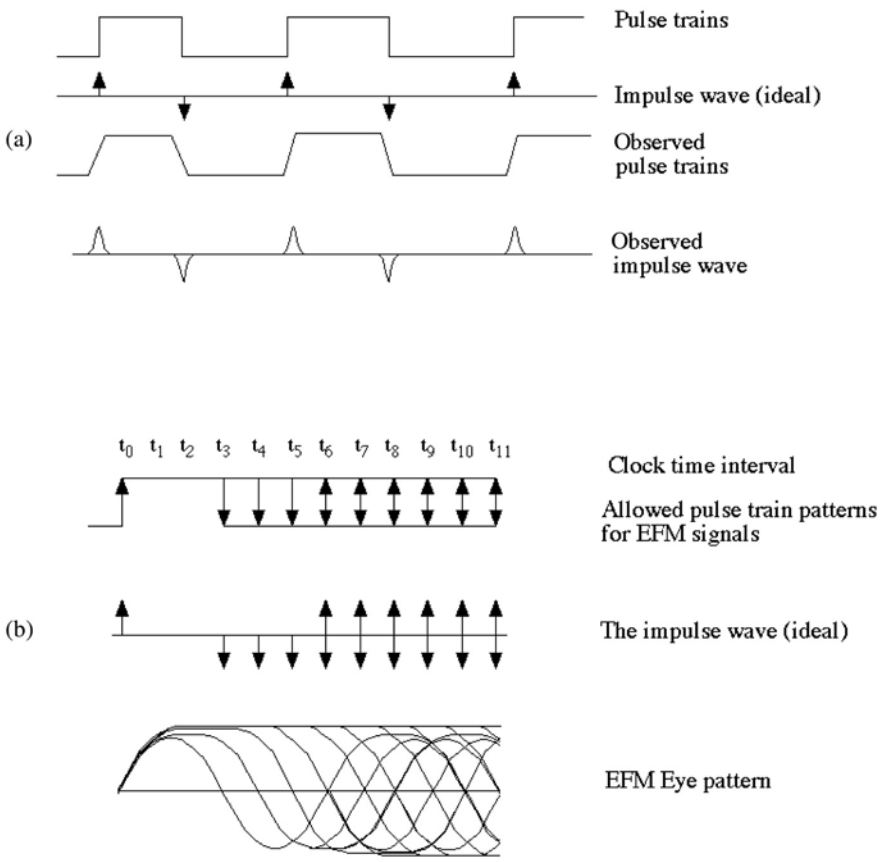

Fig. 2.7. a–b. The mechanism of CD signal reproduction. **a** The recorded pits are optically transformed by MTF and produces impulses. **b** The impulses are transformed to EFM eye pattern. If the two impulses are in proximity of each other, MTF becomes small and the eye pattern image is crashed

2.2.3 Compact Disc System

Recently available CD-Rs and CD-RWs are both families of CD. Figures 2.8 and 2.9 depicts the schematic structure of a typical CD system. A CD is made of a polycarbonate plastic substrate with a reflection layer (Al alloy) and data pits are pre-fabricated on the substrate surface. An optical head, on the other hand, consists of a semiconductor laser tip, several lenses, beam-splitters, and photo-detectors. The laser beam is focused on the disc surface through the substrate (thickness = 1.2 mm) by a voice-coil actuator. The disc usually spins at 200 to 500 cycles per minute, and most advanced CD-ROMs now rotate 4 to 12 times as fast as CDs. With the exception of magneto-optical (MO) discs, optical storage belonging to CD or DVD families do not rotate

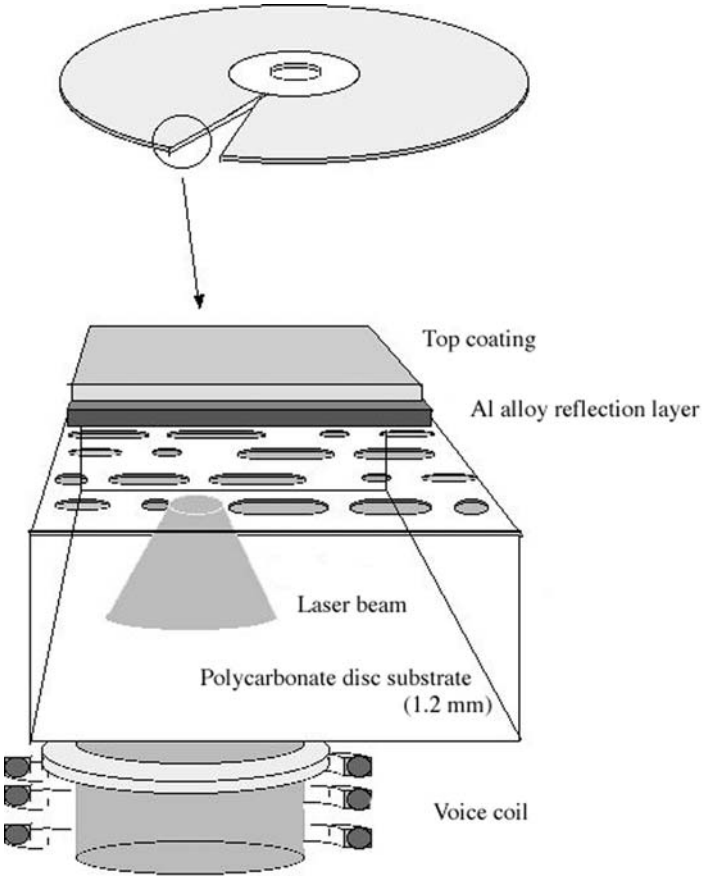

Fig. 2.8. The structure of a CD. A polycarbonate substrate is normally used and data pits are pre-fabricated on the surface by photolithograpy and mastering technique. The surface is then covered with an Al alloy thin film to reflect the incident laser beam. The beam is focused by the objective lens (NA = 0.45 in CD) and produce a spot on the surface with a diameter of 1.0 µm. Correcting the focus spot on the surface in the disc rotation, the focus lens position is always controlled by the voice coil actuator to within ±2 µm

at constant angular velocities (CAV), but at constant linear velocities (CLV) to maintain the same data density from the disc's inside to outside region.

Although CDs are produced by a molding method in high precision, once a CD is loaded in the drive, the spindle center and the disc center are not usually coincident with each other. As each recorded track of CD is separated by a distance of 1.6 µm, the focus spot crosses over several tracks during a disc rotation. This signal is observed as a tracking error signal (see Fig. 2.10). Therefore, a tracking servo system is required to hold the laser spot on one track. The focusing point determines the resolution and signal

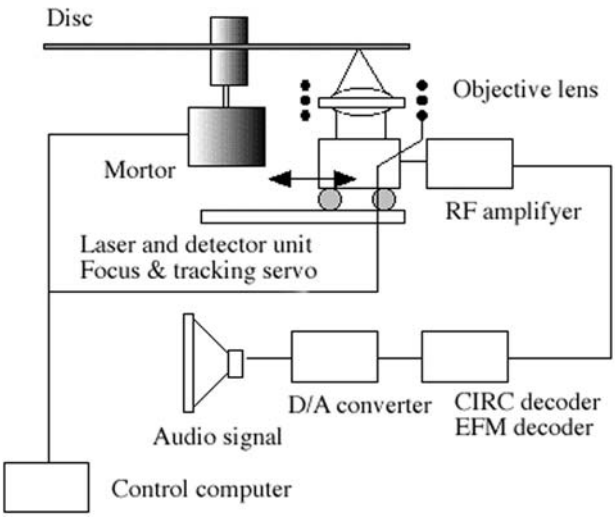

Fig. 2.9. In a CD system, the disc rotation speed is controlled to hold the same linear speed from the inside to outside (constant linear velocity, CLV). The focusing and tracking signals from the pickup unit are tracked by a computer. The reflected signals from the disc pits are then amplified and transferred to the CIRC and EFM decoder and finally sent to D/A converter

intensity of the data reproduction, on the other hand. Focusing depends on $\lambda/2(\mathrm{NA})^2 = \pm 2\,\mu\mathrm{m}$ (in DVD, $\pm 0.5\,\mu\mathrm{m}$), and the disc surface is always swinging up and down within the range of less than $\pm 0.5\,\mathrm{mm}$ by the rotation. Thus, the focusing and tracking have to be highly controlled by each servo system (focus servo and tracking servo) as shown in Figs. 2.11 and 2.12. The laser beam, which is elliptically oriented at the aperture of the tip, is reformed to a circular by a pair of prisms, and is finally focused to a 1.0μm spot with the objective lens. The prefabricated pits covered with an Al thin film scatter the incident beam: the reflection drops from the pits are detected as signals. Here, the pit depth is very important for expanding the reflection difference between the pits and flat surface. In order to obtain maximum optical-phase difference, the depth is set to approximately 100 nm and is nearly equal to a quarter wavelength of the laser beam ($\lambda = 780\,\mathrm{nm}$) while taking the refractive index of the substrate into consideration. The reflected beam is sent to the 4-divided photo detector through several optical devices such as beam splitters. More than 80% reflection is obtained at the flat surface and less than 20% from the pits. The reflection difference is analyzed as the MTF of the signals. Hence, the total intensity becomes the total signal gain, and the difference between the total intensities of two detectors is used for the tracking servo control, as shown in Fig. 2.11.

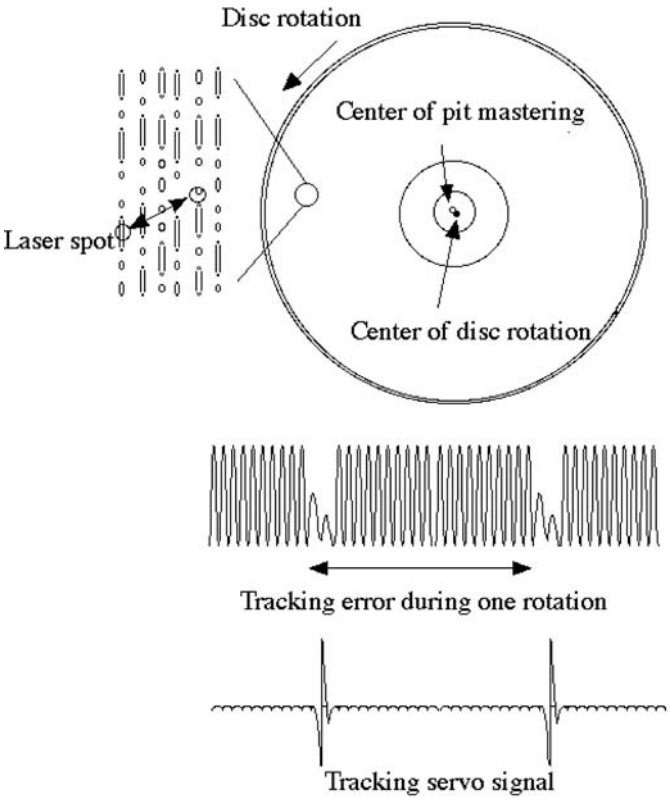

Fig. 2.10. Tracking error signal and servo-control in CD and recordable CD discs. The tracking error is generated by a small difference of the mastering center and the disc center

The photo detector used in an optical disc drive is usually divided into 4 channels, A, B, C, and D. Although several focusing servo systems and tracking systems have been proposed and have actually been used in CD and DVD, as in Fig. 2.11, a method using a cylindrical lens is depicted here. The cylindrical lens is slightly offset from the optical axis to two focusing points on the detector. At the best focusing point, the intensity of each channel detector is set to equal: $(A + D) - (B + C) = 0$. When the focusing point slightly shifts in the vicinity of the condition, $(A + D) - (B + C)$ is no longer zero. The servo system may manipulate the difference to zero in order to obtain the best focusing point. On the other hand, in tracking servo, the intensity difference of $(A + B) - (C + D)$ may be controlled by the diffraction characteristics from the pit, as shown in Figs. 2.10 and 2.11c. In early CD drives produced in the 1980s, the optical pickup module was quite robust and expensive, the unit has become much smaller and cheaper now, however.

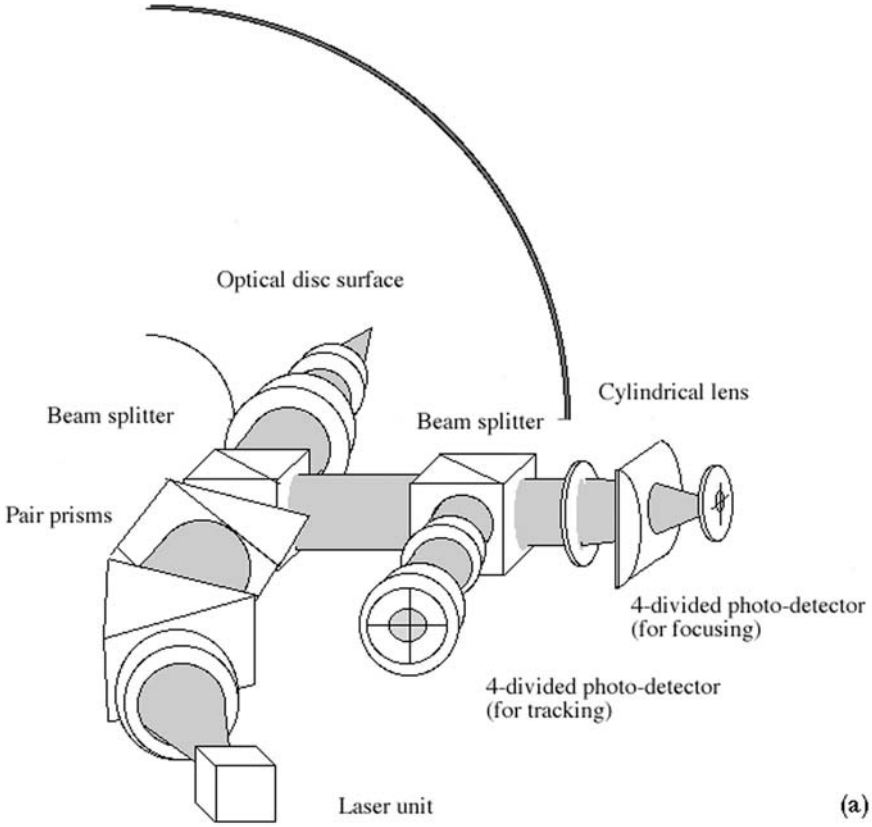

Fig. 2.11a. Optical pickup system to read out data pits. Hence, the cylindrical lens is used for focusing and the push-pull method for tracking error detection

2.2.4 Optical Pickup Heads

An optical disc system basically consists of an optical head and a storage disc. The pickup head is generally designed to derive the maximum performance from the storage disc. The role of the optical head is to focus the laser beam on a disc surface with a spot size defined by the theoretical diffraction limit. The head has to detect reflected light coming back from the disc and transfer the optical signal to an electrical one at the same time. Additionally, the head plays a role in guiding the laser beam along pre-fabricated pit trains or a groove. In order to attain the performance, in general, the optical head has to be at least composed of a semiconductor laser unit, grating, beam splitters, objective lens, and 4-divided photo-detectors. As shown in Fig. 2.13, an optical pickup head of CD is now very simplified. Figure 2.11a shows a complicated optical head used in early CD drive. The laser beam is highly elliptical at the facet and the beam shape had to be improved by inserting

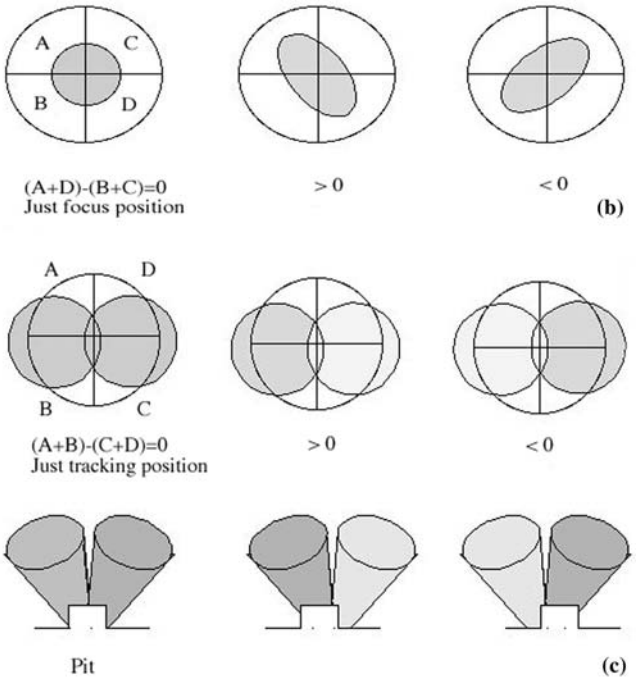

Fig. 2.11. b Focusing error detection by 4-divided photodetector. **c** Tracking error detection

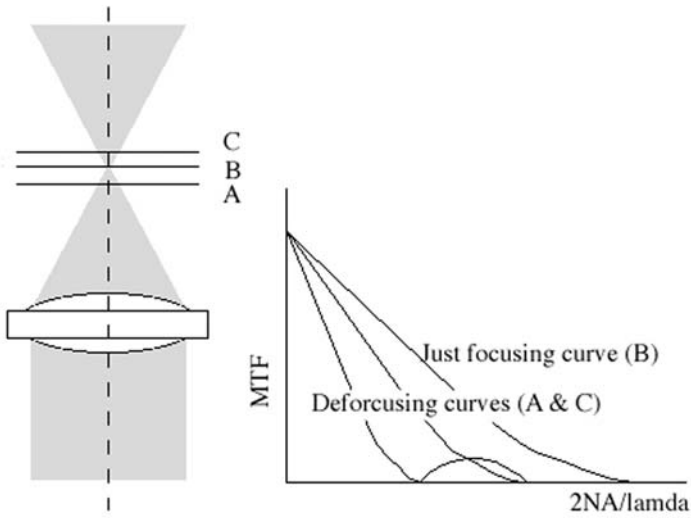

Fig. 2.12. Relationship between the focusing point and the MTF. In defocus positions, the theoretical resolution is not obtained

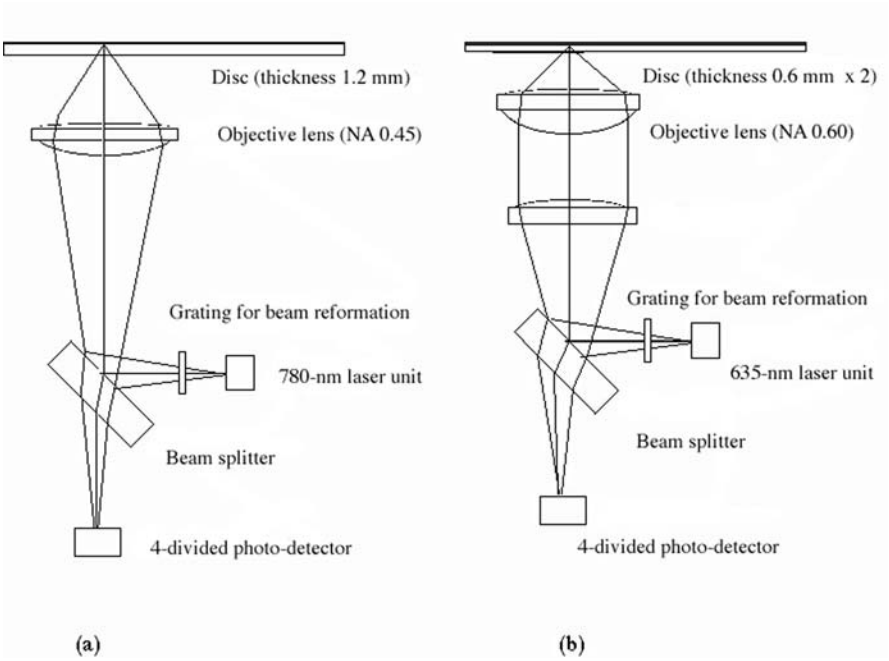

Fig. 2.13. a–b. Optical pickup heads of CD and DVD systems. **a** CD. **b** DVD

double prisms, for example, in early CD pickups. However, the components in a current CD drive are simplified and the beam shape is reformed by the combination of a beam-splitter plate and an objective lens. In Fig. 2.13b, an optical head of DVD systems is also depicted. To reduce the astigmatic error on the focus point, a collimator lens is inserted behind the objective lens.

2.2.5 Disc Mastering and Molding

The recording films and disc designs of CDs and DVDs have mostly influenced the optical properties and rewritable characteristics. In a CD, a series of $3T$ to $11T$ signals of the EFM are first cut in a photopolymer film spin-coated over a very flat glass disc by short wavelength laser beams. Applying electroplating technique, a metal master disc is then formed. Using the master, many stumpers (copies) are produced and subsequently polycarbonate disc are stumped by an injecting molding technique. In order to increase reflectivity, an Al alloy is usually deposited by a dc or rf sputtering method in a vacuum chamber. Finally, a cover layer is spin-coated on the film (Fig. 2.14). In a CD or CD-ROM, the durability of the metal alloy plays an important role in the reflectivity and the reproduced signal characteristics. Finally, it should not be forgot that the successful CD fabrication strongly depends on the advance of the high-precision injection molding technology. Now the pro-

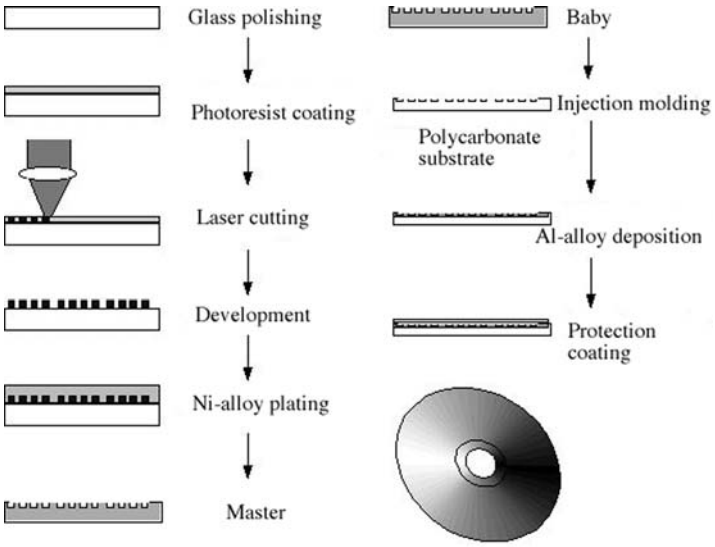

Fig. 2.14. Fabrication method of optical discs. The data pits are cut precisely by a mastering system with a UV laser source. Thus, the recording densities of CDs and DVDs are deeply related to the cutting laser wavelength and the high NA lens

duction line can make a copy in about 5 seconds or less! In addition, once a master disc is produced, you can make more than 50,000 copies of the disc.

2.2.6 Multilayer Designing of Recordable Disc

In a CD, the pit depth determines the phase difference resulting in the MTF change between the pit and the other flat area. In a recordable disc, however, several layers are multi-stacked in order to obtain not only the maximum reflection change between recorded marks and the non-recorded area, but also, the best thermal condition during recording as well. In the former objectives, several computer simulation techniques for calculating the reflection from the optical multilayer are usually used. A simple technique is to use a matrix method [5]. Electromagnetic field E and H of the boundary conditions of m-th and $(m-1)$-th layers in a multilayered stack are simply given by

$$E^{+}_{m-1} = [E^{+}_{m} \exp(\mathrm{i}\delta_m) + r_m E^{-}_{m} \exp(-\mathrm{i}\delta_m)]/t_m \tag{2.4}$$

and

$$E^{-}_{m-1} = [r_m E^{+}_{m} \exp(\mathrm{i}\delta_m) + E^{-}_{m} \exp(-\mathrm{i}\delta_m)]/t_m \tag{2.5}$$

Hence, E_m, E_{m-1}, r_m, δ_m, and t_m are electric field on m-th layer and that of $(m-1)$-th layer, reflectivity, phase difference, and transmissivity of m-th

layer, respectively. The suffix + and − express incoming and reflecting waves at a layer boundary. Magnetic waves H_m and H_{m-1} are also expressed with the same ways. In the case of the multilayers, the recurring relationship is described by the matrix form

$$\begin{pmatrix} E_{m-1} \\ H_{m-1} \end{pmatrix} = \begin{bmatrix} \cos\delta_m & \dfrac{\mathrm{i}}{\mu_m}\sin\delta_m \\ \mu_m \sin\delta_m & \cos\delta_m \end{bmatrix} \begin{pmatrix} E_m \\ H_m \end{pmatrix} .$$

Thus, for an N-layer stack,

$$\begin{pmatrix} E_0 \\ H_0 \end{pmatrix} = \prod_{m-1}^{N} M_m \begin{pmatrix} E_N \\ H_N \end{pmatrix} ,$$

where

$$M_m = \begin{bmatrix} \cos\delta_m & \dfrac{\mathrm{i}}{\mu_m}\sin\delta_m \\ \mu_m \sin\delta_m & \cos\delta_m \end{bmatrix}$$

and

$$\begin{pmatrix} E_N \\ H_N \end{pmatrix} = \begin{pmatrix} 1 \\ \mu_{\mathrm{sub}} \end{pmatrix} E^{+}_{\mathrm{sub}}$$

Consequently, reflection R and transmittance T are obtained as

$$R = \left| \frac{\mu_0 E_0 - H_0}{\mu_0 E_0 + H_0} \right|^2$$

and

$$T = \frac{4\mu_0\, \mu_{\mathrm{sub}} \left| E^{+}_{\mathrm{sub}} \right|^2}{\left| \mu_0 E_0 + H_0 \right|^2} \tag{2.6}$$

Hence, $\mu_m = n_m/\cos\theta_m$ is for the p-component of polarization and $\mu_m = n_m \cos\theta_m$ for the s-polarization. The term δ_m is defined as $2\pi n_m d_m \cos\theta_m/\lambda$. Also, n_m is the film refractive index and d_m is the thickness, and θ_m is the incident angle of the beam (see Fig. 2.15). E_0 and H_0 are electric and magnetic fileds at 0-th layer.

Now, the matrix calculation, including the imaginary part of each layer's refractive index, is easily carried out by commercially available mathematical software. The crystalline and amorphous reflection curves of optical phase-change disc are shown in Fig. 2.16, for example. The second ZnS-SiO_2 layer film thickness is given by the x-axis. As shown in Fig. 2.16, it is easily understood that approximately 30 nm is the best value for the film thickness to obtain the maximum modulation: $(R_{\mathrm{c}} - R_{\mathrm{a}})/R_{\mathrm{c}}$.

Here, R_{c} and R_{a} mean reflectivity of the crystalline area and amorphous marks, respectively. Following the simulation, the recording film thickness is determined (Fig. 2.17). That is, it is found that the thickness to obtain the

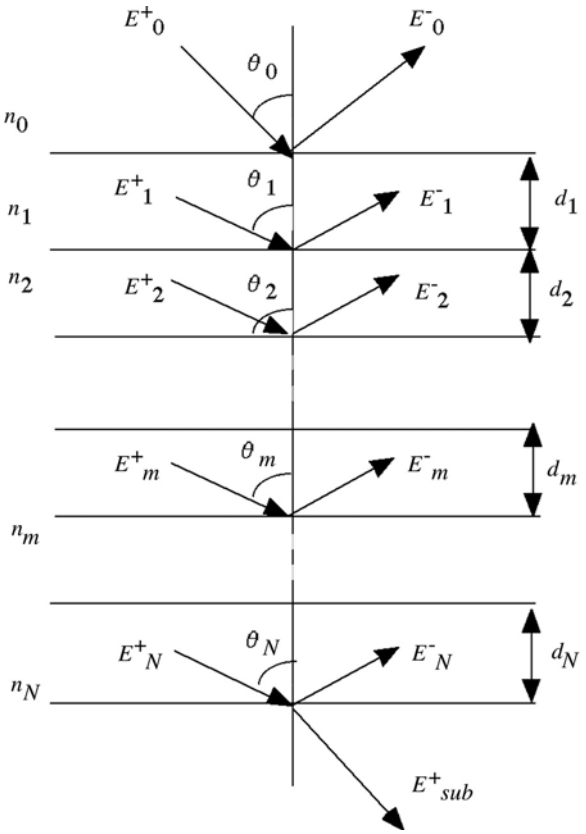

Fig. 2.15. Multilayer stacks and reflection & transmission

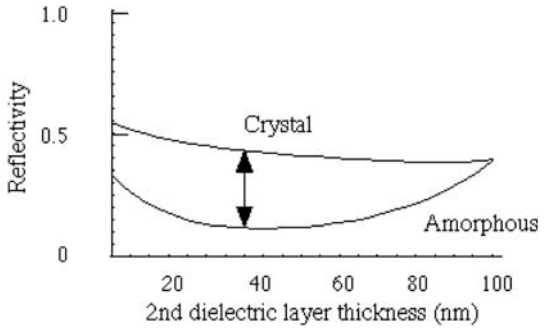

Fig. 2.16. The computer-estimated reflection change between amorphous and crystalline state in DVD-RAM. The simulation was carried out in the structure PC/ZnS-SiO_2 (100 nm)/$Ge_2Sb_2Te_5$ (20 nm)/ ZnS-SiO_2 (x-nm)/Al arroy (100 nm). In the simulation, the incident beam (633 nm) is a plane wave and normal to the surface

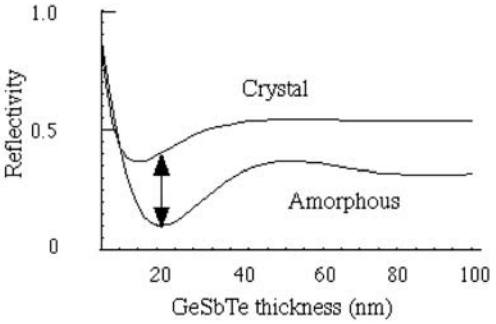

Fig. 2.17. The second ZnS-SiO_2 layer's thickness is fixed at 30 nm, and instead the recording layer thickness is changed. The simulation structure is thus PC/ZnS-SiO_2 (100 nm)/$Ge_2Sb_2Te_5$ (x nm)/ ZnS-SiO_2 (30 nm)/Al arroy (100 nm)

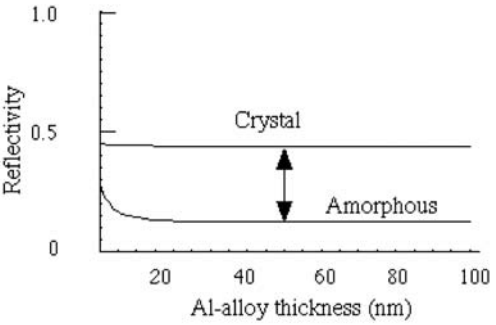

Fig. 2.18. The Al alloy thickness is changed. The simulation structure is thus PC/ZnS-SiO_2 (100 nm)/$Ge_2Sb_2Te_5$ (20 nm)/ ZnS-SiO_2 (30 nm)/Al alloy (x nm)

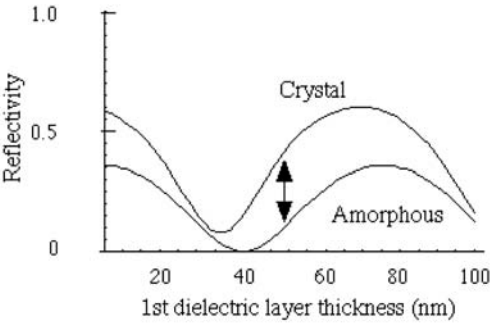

Fig. 2.19. The first ZnS-SiO_2 layer's thickness is changed. The simulation structure is thus PC/ ZnS-SiO_2 (x nm)/$Ge_2Sb_2Te_5$ (20 nm)/ ZnS-SiO_2 (30 nm)/Al alloy (100 nm)

maximum MTF is 20 nm. As the recording film thickness increases beyond 40 nm, the optical interference of the crystalline curve is eliminated because of the large imaginary index of refraction of the phase-change material. On the other hand, the amorphous curve shows the interference by about 70 nm. When the thickness of Al alloy is thinner than 30 nm, the modulation becomes smaller (Fig. 2.18). However, the heat sink effect is more important to determine the thickness and usually it is fixed at 100 nm. The first ZnS-SiO_2 layer thickness is only used to adjust the total reflection, but a little to consider the thermal damage to the polycarbonate substrate (Fig. 2.19). In the real and more complex simulation, the diffraction effect from the grooves is also included.

2.2.7 Organic Dye Disc

Due to strong customer demand, write-once recording CD, CD-R, and rewritable or erasable CD, CD-RW, have rapidly been spread worldwide for the last few years. The manufacture of CD-Rs is one of the successful applications of organic materials to optical data storage [6, 7]. The substrate disc of CD-R and CD-RW are mostly the same as a CD, except for the groove depth. Grooves are cut on the disc surface for the laser beam guiding for recording and readout, instead of using pre-mastered pits in a CD. The groove depth of a CD-R is much deeper than that of a CD-RW because the refractive indices of the organic dyes are relatively smaller than that of metal or metal alloys (phase-change materials) used in a CD-RW. The depth is approximately 80 nm to 120 nm in a CD-R. The groove width is the same pitch as that of a CD: 1.6 µm. The fabrication method of the substrate discs is the same as that of a CD, and the dye film is spin-coated. After drying the dye, a thin metal reflector is deposited by dc sputtering, and finally a protection layer is covered (Fig. 2.20). The total reflection from the disc is more than 70% , and the MTF is about 60%. The dye has a special light absorption coefficient in a region of the laser wavelength (780 nm). Focusing the laser beam with a high power (more than 7 mW) in comparison with the readout power, the dye molecular is decomposed or melted, resulting in the formation of fragment molecules and a gas bubble with a different refractive index. Consequently the reflection greatly decreases by 20% or less. The thickness of the dye is determined so that the reflection and the MTF are optimized. The dye viscosity and spin-coating speed are both important factors. A CD-R has several advantages in comparison with other writable optical discs: the production is relatively easy and the media cost is greatly reduced. However, CD-R has a fatal disadvantage against the inorganic recording film because of the narrow absorption edge over wavelength. In the history of optical data storage, the wavelength applied to recording and readout has been shorter and shorter—from 780 nm to 650 nm and from 635 nm in DVD to 405 nm in the next generation DVD-blue system. Therefore, as the new system with a shorter wavelength is intro-

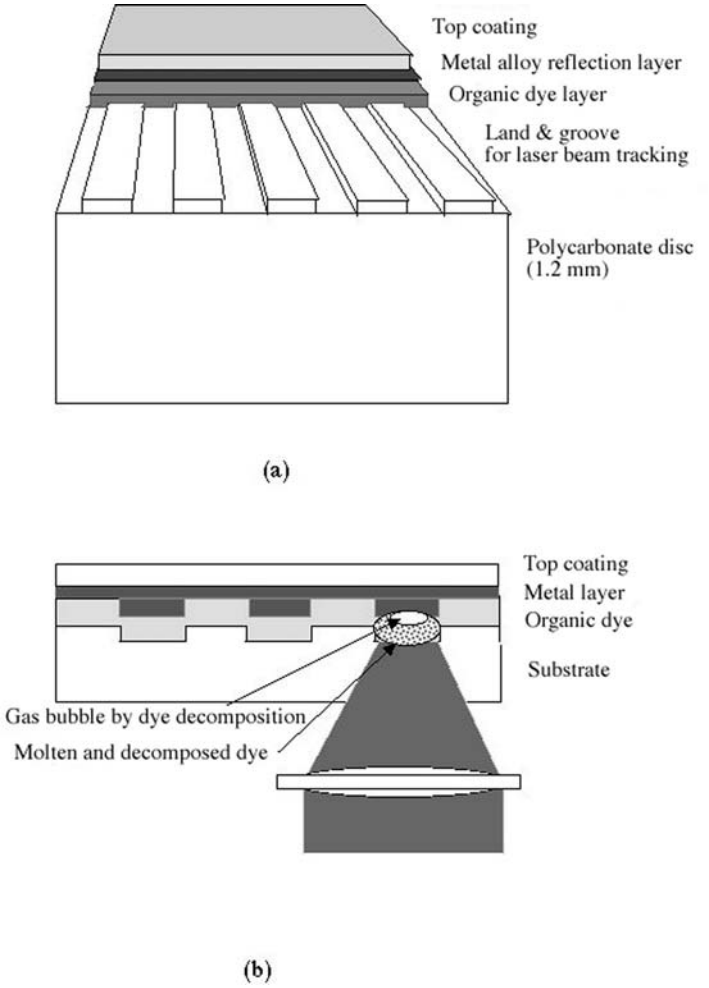

Fig. 2.20. **a** CD-R structure. **b** Pit formation mechanism

duced, the old dye's refractive index no longer fixed to the new drive system, resulting in holding two laser pickups for both old and new discs.

2.2.8 Inorganic and Metal Alloy Disc

CD-RW and MO discs are composed of inorganic alloy thin films as the recording layers. Although the MO disc was commercialized first, the phase-change optical disc CD-RW is now more common in storage market because of the compatibility with CD-R and CD drive infrastructures. In an MO disc, a slight light polarization difference is detected as a signal, and the effect is due to the Kerr effect of the magnetic thin film of the TbFeCo alloy. The

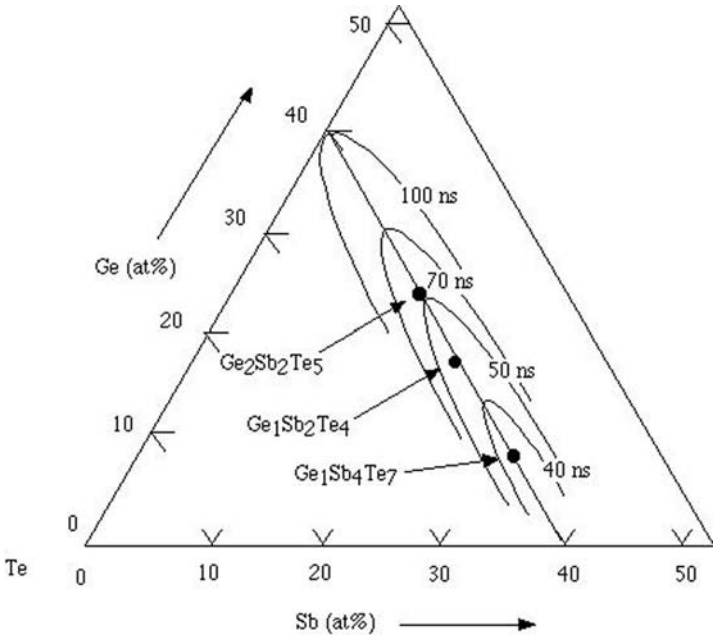

Fig. 2.21. Crystallization time of GeSbTe ternaly system. Reprinted by permission of the publisher, [9]

detail of MO disc is recently well summarized in *The Physical Principle of Magneto-Optical Recording* by Masud Mansuripur [8]. Therefore, in this book we focus on optical phase-change (PC).

The base of PC recording was born in the early 1970s, by Ovshinsky's ovonic memory due to a great refractive index change of chalcogenides in between amorphous and crystalline states. Soon after the first invention, more applicable alloys in PC recording were discovered: GeTe. The transition temperature from the as-deposited amorphous to crystalline states was quite low (155°C), however. Then Sb was further doped into the alloy, and finally a series of GeSbTe alloys were invented to increase the transition temperature and rewritability. The recording materials used in DVD-RAM are mostly close to the composition of the binary system of Sb_2Te_3 and GeTe. In particular, $Ge_2Sb_2Te_5$ is the most suitable alloy for PC recording. Beside the composition, $GeSb_4Te_7$ and $GeSb_2Te_4$ are also available. The relationship between the composition and the crystallization time is shown in Fig. 2.21.

As the Ge composition increases, the crystallization speed increases. Recently, the Sn-doped GeSbTe alloy has been studied to further increase the transition speed for high data transfer rate.

Besides GeSbTe eutectic alloys, another alloy, AgInSbTe, has also been developed in rewritable PC disc, CD-RW and DVD-RW for the last decade. The alloy is a complicated system whose detail characteristics have been

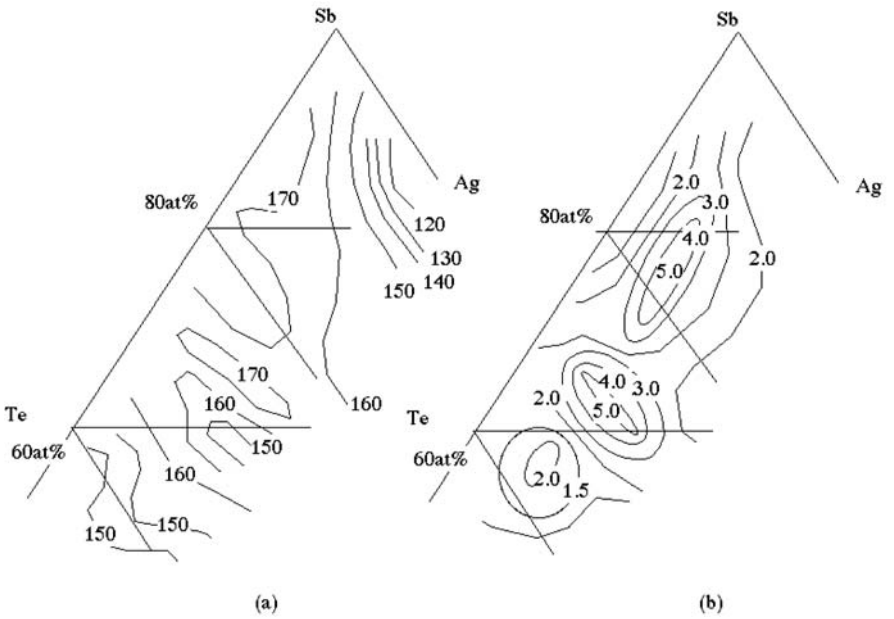

Fig. 2.22. a–b. Phase diagram of AgInSbTe alloy. Hence, In composition is fixed at 2.5 at%. **a** Transition temperature (°C) from sputtered as-deposed (amorphous) to crystalline state. **b** The activation energy (eV) [10]

difficult to understand for the first 5 or 6 years after it was first reported. However, the mechanism has gradually been elucidated that Sb mostly dominates the crystallization speed and Ag plays a role of the rewritability. Now, $Ag_{11}In_4Te_{28}Sb_{57}$ has been applied to commercial CD-RW as the typical and practical alloy composition. As the Sb ratio increases, the crystallization speed increases further; but the transition temperature decreases at more than 65 at% (Fig. 2.22). To improve the thermal stability of the AgInSbTe alloy, it was found recently that a small amount of Ge greatly improves the stability [10].

In PC recording, at first, the recording film has to be crystallized for rewritable use, before shipment. Due to of the amorphous state of the as-deposited film, the procedure is required by using a highly elliptical laser beam. The crystalline state of PC films is more stable than that of the amorphous state. The amorphous state, however, is one of the stable states in free energy, by which the film is transformed into the state through rapid cooling after the molten state. Along the cooling curve, a molten amorphous state is held at even less than the crystalline temperature (T_c) through the glass transition temperature (T_g). Therefore, controlling the cooling speed by multiple laser patterns, the state of the PC films is switched between the amorphous and crystalline state. In CD-RWs, DVD-RAMs, and DVD-RWs,

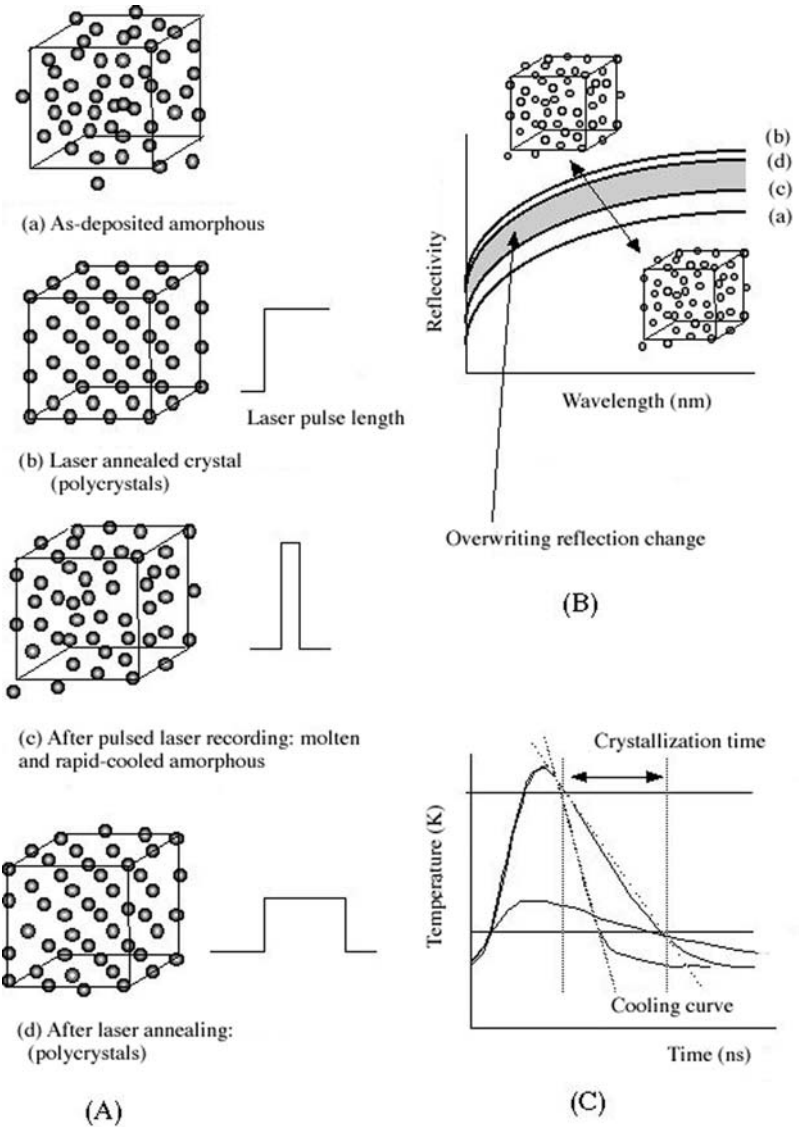

Fig. 2.23. a–d. The structure transition of PC recording film. The as-deposited PC film is usually in amorphous state **a** and once the state has to be crystalized by a bulk laser system **b**. Controlling the laser pulse length and power, which increases the temperature more than the film melting point (T_m), a new amorphous state is generated **c**. As the power decreases so that the temperature drops below T_m and the pulse time is kept longer than the intrinsic crystallization time (t_c), the amorphous state returns to the polycrystaline state **d**. The recording power level and erasing (crystallization) power level are unified in a recording pulse trains for overwriting. In a PC disc system, a cooling speed of more than 10 K/ns is required to produce the amorphous state

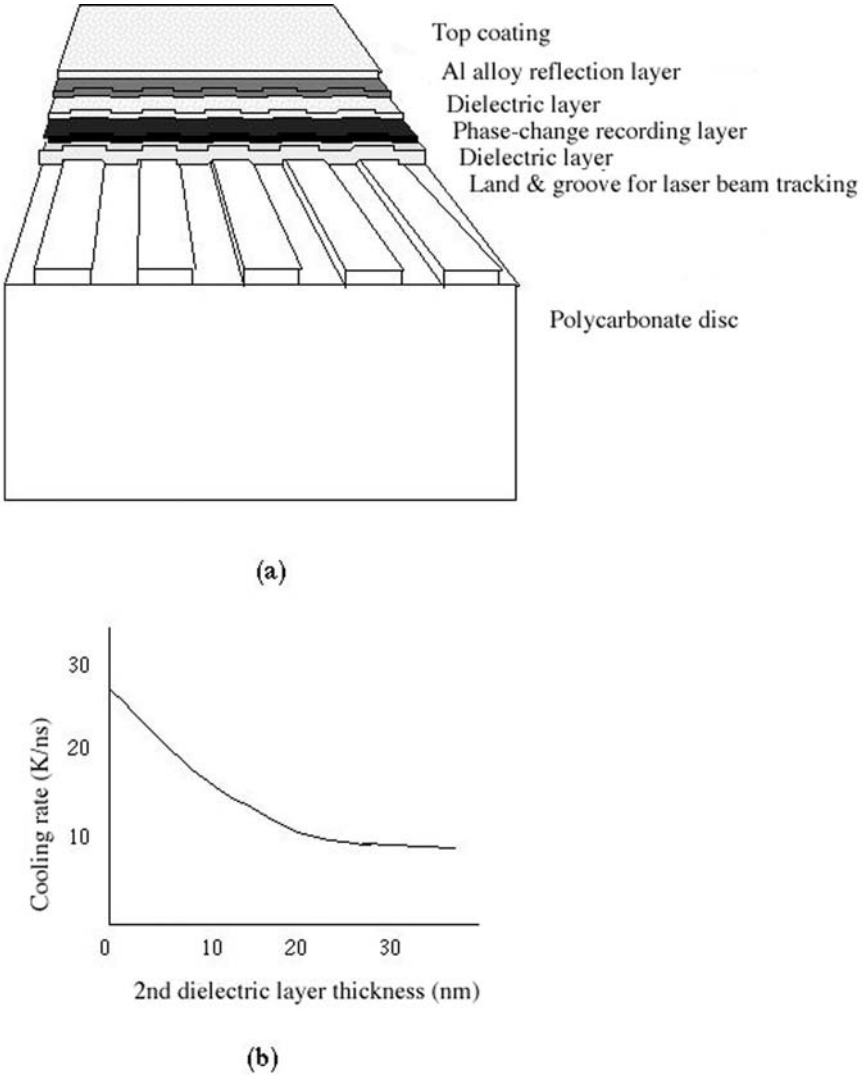

Fig. 2.24. The PC disc structure **a** and cooling rate as a function of the second protection layer thickness **b**

3 different multi power levels are adapted to directly overwrite new marks over the old ones (Figs. 2.23 and 2.24).

In PC recording, overwriting was the fatal disadvantage in comparison with that of MO disc. For a long time, the main reason has been believed to be the thermal segregation of the alloy composition or gas voids generated in the film. This suggestion is not always true, but it gradually became clear that the thermal diffusion of free S atoms weakly-bonded to Zn or Si in ZnS-SiO_2 films, which are typically used as the protection layers, is the main factor that limits the overwriting cycles. To prevent the S diffusion into the GeSbTe layer, GaN layers are additionally inserted between the ZnS-SiO_2 layer and the recording layer [11]. Then the PC overwriting now exceeds more than 500,000 cycles. In AgInSbTe alloy, on the other hand, the S diffusion is more sensitive than that of GeSbTe because the formation enthalpy of Ag_2S is more stable than any other compounds with Ge and Sb. In the alloy, as the amount of Ag is approximately 10 at% , the compound formation greatly damages the overwriting. In order to block the S diffusion, a small amount of Ce is doped in the ZnS-SiO_2 layer, instead of using a GaN layer. The inserted Ce produces the most stable compound with S in the formation enthalpy [12]. Thus, as the free S atoms are completely blocked, the overwriting was greatly improved from only 3,000 to more than 300,000 cycles (Fig. 2.25). More recently, the thermal stability of AgInSbTe alloys was also strengthened by doping Ge. Using the new alloy AgInSbTeGe, a surprising data transfer rate of more than 200 Mbps was obtained for the first time in optical data storage.

In GeSbTe and AgInSbTe alloys, there exists a large difference between the recording and erasing mechanism [13]. In GeSbTe, nucleation mostly dominates its erasing characteristics. First, a small nuclei of the crystal is generated in the amorphous recorded mark, and the numbers determined the crystallization time. Therefore, the front of the crystal region moves from the mark inside to outside. In AgInSbTe, on the other hand, the crystallization process is dominated by crystalline growth rather than nucleation. As a result, the erasing process starts from the mark outside to inside: the amorphous mark is squeezed by the surrounding crystalline region (Fig. 2.26). Therefore, for further high-density recording, it is believed that the later characteristics are more suitable because it involves fabrication of much smaller amorphous marks.

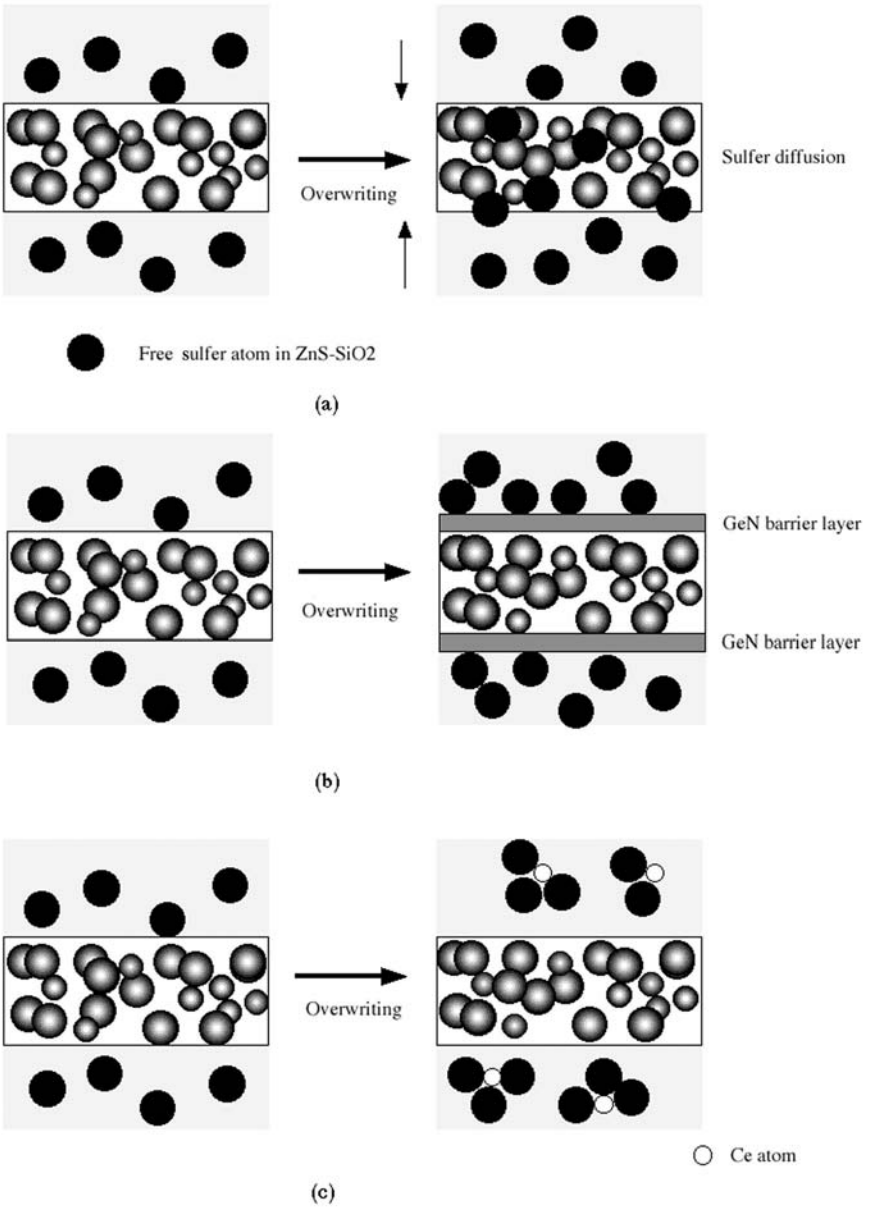

Fig. 2.25. a–c. Thermal damage of PC recording by overwriting and its improving methods. **a** Free sulfur atoms gradually invade the recording layer by thermal diffusion of overwriting, resulting in the composition change. **b** Typical method to protect the S diffusion by inserting GeN layers. **c** Another method by doping Ce atoms in the ZnS-SiO_2 layers to trap the S diffusion by the chemical affinity of Ce-S

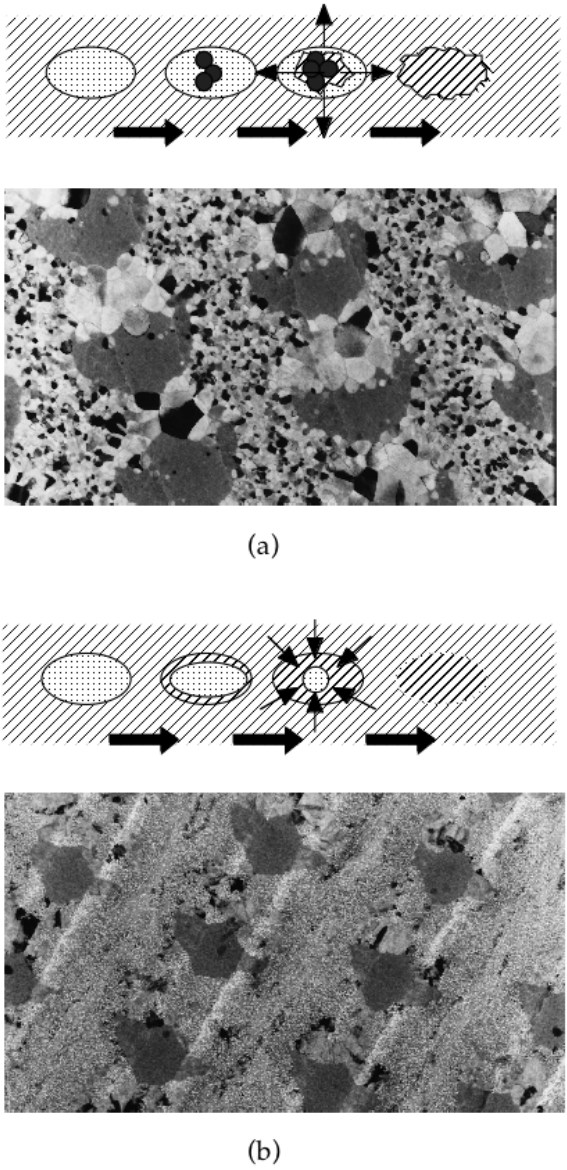

Fig. 2.26. a–b. Different crystallization mechanism (*top*) in GeSbTe and AgInSbTe alloy, and the actual recorded mark shapes after overwriting.(*bottom*). **a** GeSbTe case. **b** AgInSbTe case. In GeSbTe, the nucleation process dominates the crystallization process; on the other hand, crystalline growth dominates the process in AgInSbTe alloy. For high-density recording, AgInSbTe alloy may be much more preferable because of the effect of self-erasing mark squeezing. (Courtesy of TDK Corp)

2.3 Several Approaches Towards Ultra-High Density Optical Recording

2.3.1 Beyond DVD

Optical recording density depends on the focused spot size of a laser beam, as described in Sect. 2.2.1. The beam size (d) on the optical disc is determined by the wavelength (λ) and lens numerical aperture (NA), where $d > \lambda/(2NA)$; therefore, the resolution of the minimum mark is the half of d as already been discussed. In a CD, λ is 780 nm and NA is 0.45. Thus the minimum mark size was specified at 900 nm. In a DVD, on the other hand, λ is 635 nm and NA is 0.6; thus the minimum size of the mark is about 400 nm. In the upcoming new DVD system using 405-nm blue laser, NA is further increased by 0.85; the minimum mark will be approximately 140–160 nm. As NA increases, the space between the bottom of the lens and the medium surface narrows and it is less than 1.0 mm in the blue-laser system. Finally, as NA reaches 1.0, the bottom contacts the recording film. At the moment, we have no cheap laser unit emitting wavelength shorter than 405 nm. If we pursue far-field optics and its technology, the recording density is saturated by 20–30 GB in a 12-cm disc.

In order to further increase the recording density, several new approaches have been studied and proposed for the last 10 years. A simple but promising way is to stack multiple recording layers normal to the disc surface. However, as the recording layer usually has a light absorption coefficient, a three- or four-layer stack will be the limit using this method. Furthermore, the production cost will be very high because of the adjustment of the center position of each layer and depth focusing problems. The maximum recording density will be close to 80–100 GB per disc surface.

In MO recording, the magnetic super-resolution (MSR) technique has widely been studied and partly realized in new MO drive systems [8, 14–16]. Several MSRs have been proposed so far: front aperture detection (FAD), central aperture detection (CAD), magnetic amplifying MO system (MAMMOS), and domain wall displacement detection (DWDD). All these MSR methods typically use two or three MO layers with different magnetic corrections and Curie temperatures. For example, in a FAD system, by controlling the laser power, a switching layer with a high magnetization due to a transition-metal-rich phase, but a low Curie temperature in comparison with the recording layer, plays a role of cutting the exchange coupling between the writing and recording layer. As an external magnetic field is applied, the temperature of the laser spot exceeds the Curie temperature of the switching layer, and then the exchange coupling is eliminated. The readout layer feels the external magnetic field and the magnetization direction turns toward the external field. This effect seems to play a role in partly masking the magnetic area for the readout. As a result, a smaller magnetic domain beyond the reso-

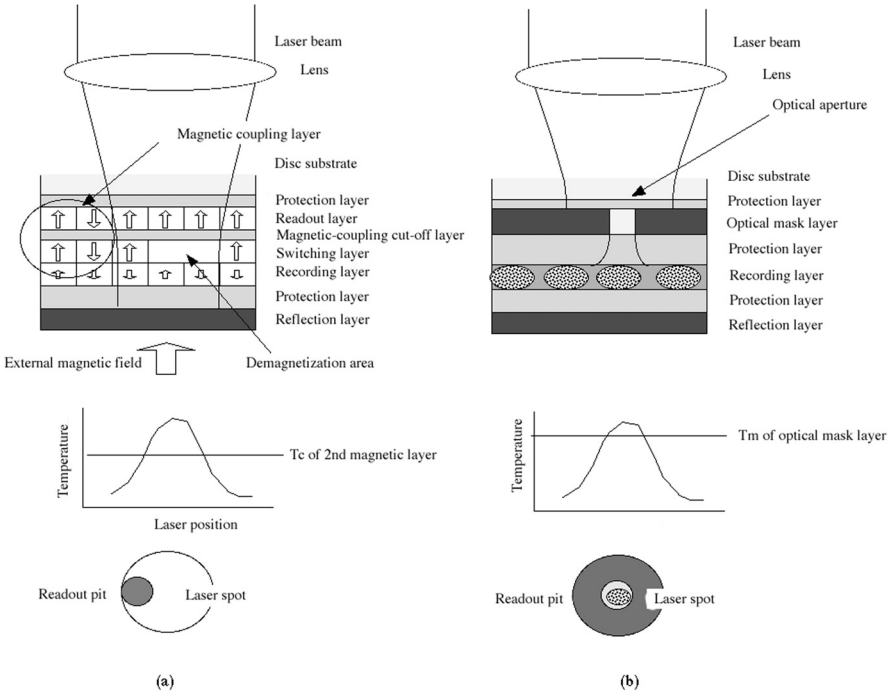

Fig. 2.27. a–b. Super-resolution techniques using magnetic mask layer (**a**) and optical mask layer (**b**). The term T_c is Curie temperature and T_m is melting point of the layer

lution limit is obtained by controlling the laser beam power and temperature (Fig. 2.27).

Following MSR technologies, optical super-resolution (OSR) technology was proposed in the mid 1990s [17] where the PC recording layer was used as the mask layer. By focusing the laser beam, the mask layer (GeSbTe alloy) absorbs the light energy and the temperature increases. As the temperature approaches the melting point, the atomic mobility of the alloy increases, and then the crystalline state becomes amorphous. As described, the PC alloy shows a big change of the refractive index between the two states. The imaginary index of the amorphous state is 1 or 2 smaller than that of the crystalline state; the change plays a role in an optical window. By controlling the laser power, the window size is decreased in the laser spot size, as determined by the diffraction limit. The part outside of the window block reflects the laser beam: the optically generated small window thus determines the resolution. This technology is very simple and needs no magnet used in MSR. This OSR technology is discussed in more detail in later chapters with the combination of near-field recording.

The third method is multilevel recording. In CDs and DVDs, the binary bit is encoded and decoded as information signals. In multilevel recording, each pit or mark position is fixed, but the size of the mark has a multicode.

Unfortunately, even using the above new techniques based on far-field optics, the achievable storage density will be saturated by 100 GB. We have to anticipate a new optical principle that can overcome the far-field limitation. This is the area of near-field optics and the focus of this book.

2.3.2 The Characteristics Requirement for Optical Near-Field Recording

In optical near-field recording, much small marks (< 200-nm) are going to be recorded and read out by several different optical probes which are fixed above the recording medium (< 100 nm). Although the principle characteristics of optical near-field recording will be discussed in a later chapter, we want to note here that the near-field light cannot propagate beyond 100 nm, and the intensity exponentially reduces against the distance. According to the specific characteristics and the need to obtain higher data transfer rate, the medium surface has to be ultimately flat in comparison with the current recordable DVDs or CDs. In a CD or DVD, the substrate disc is mostly composed of polycarbonate plastic; the disc surface fluctuates by spinning. A glass substrate will be more suitable but expensive. Furthermore, materials, which generate a volume deformation after the recording, should be eliminated from the candidates. Thirdly, the materials should hold large optical contrast in the vicinity of the recording: refractive index, transparency, birefractive index, and so on, because the near-field signal is generally very weak in comparison with that of the far-field readout. Near-field optical recording will not be performed, until all these issues are cleared technically. We are going to discuss several scientific approaches and technologies of near-field recording proposed over the last 10 years in the following chapters.

3 Basic Theory of Optical Near-Field and Surface Plasmon Polaritons

In this chapter, we deal with the basic principles and theories of optical near-field and its characteristics, focusing on applications optical recording. First, Fourier optics is introduced which is intuitively understandable, and then the more precise treatment using a numerical simulation method called "Finite-Difference Time-Domain" (FDTD) is described to further help the understanding of near-field optical recording.

3.1 Basic Theory of Optical Near-Field, Surface, and Local Plasmons

The "optical near-field" is an electromagnetic field generated around an object, on which light wave is radiated. When you watch something interesting, your eyes usually identify it by the light reflected from the surface. The light field is called "optical far-field," which propagates in the space between the object and a detector (eyes). Most of all optical phenomena and the applications are usually based on the far-field optics. Technologies used in optical data storage up to now are not exceptional. Optical near-field, in contrast, is a non-propagating electromagnetic field and the intensity exponentially decays normal to the surface. The area in which the field exists is usually limited to less than 100 nm, but the field itself is not observed in our usual life because of the non-propagating characteristics. However, the optical near-field has a unique characteristic in that it generates over surfaces of all materials small or big, and the size is not constrained by the diffraction limit discussed in Chap. 2. Therefore, using optical near-field, in principle, we can read out very small marks or pits beyond the diffraction limit of the far-field optics.

Near-field optics is not new physics, and was first reported by Synge in 1928. The characteristics of small optical apertures were theoretically analyzed and treated by Bethe in 1944. In microwave, the analysis is easier than that of visible light because several metals are available as an electrically perfect conductive surface, and the experiments are much more suitable and easier for fabrication and treatment in micron- or cm-size. The study and experimental treatment in optical region had little progress until the fabrication methods of nanometer-size near-field probes (aperture and scattering center) and their precise control systems were developed, thanks to the invention of

scanning tunneling microscopes and atomic force microscopes. Since the first scanning near-field optical microscope (SNOM) was invented by Lewis and Pohl in 1984, a great number of experiments have flowered and several unique characteristics have been discovered. Now, although the research gradually trends to the manipulation of atoms and molecules, ultra-high density optical data storage and several other photonic applications are also actively studied.

Unfortunately, the theoretical studies of optical near-field had made little progress because of the difficulties dealing with a perfect conductive metal surface in optics; obtaining the analytical solutions was very hard. Instead, the studies with Fourier optics had been carried out prior to further detail analysis, but the analysis was intuitively understandable; the behaviors included optical many-body problems and its scattering have gradually been elucidated. In order to analyze the experimental results more precisely and in detail, several self-consistent field analysis in electromagnetic field have been proposed by directly solving the Maxwell's equation, using finite element analysis, multiple-multipole (MMP) method, and finite-difference time-domain (FDTD) method, for example. Recently, The FDTD analysis has widely been available rather than the other methods. In this chapter, let's first focus on the Fourier analysis giving several intuitive concepts of near-field optics, followed by the FDTD treatment later.

Assuming an optical grating and incident light beam normal to the surface, here, we consider the behaviors of the localized electromagnetic field and optical near-field in terms of Fourier optics. The optical grating is a tool consisting of narrow grooves fabricated on a glass surface, from which the incident light is diffracted. The width between the adjacent grooves is usually patterned with a size lager than the incident light wavelength, and the diffracted light is depicted in Fig. 3.1a. The diffracted angle depends on the width of the grating, and the light is diffracted with more broad angles, as the width becomes narrower (Fig. 3.1b). Finally, the diffracted lights run over the surface of the grating and only the direct reflected and transmitted lights are observed beyond the threshold width (Fig. 3.1c). As the light energy has to be preserved before and after the threshold, however, the part of the energies has to exist somewhere on the surface in the system. This is the evanescent wave or surface plasmon polariton (we will only use the term surface plasmons hereafter) and it sometimes has complicated electromagnetic field interactions with the grating pattern. The existence of the surface plasmons is indirectly observed as an energy loss of the total incident wave because the electromagnetic wave vector k_z becomes an imaginary number; the wave propagation $\exp(-ik_z z)$ becomes a real number and then rapidly decreases with z. How can the surface plasmons be retrieved outside the grating as a far-field light? Let's bring another grating with a different grating width and put it just above the first grating at a distance of less than the incident light wavelength (λ). Then, in addition to the direct reflected and transmitted lights, several different diffracted lights are released as well. The effect is called "evanescent coupling," which is a primary device for exchanging optical near-field with far-field technology.

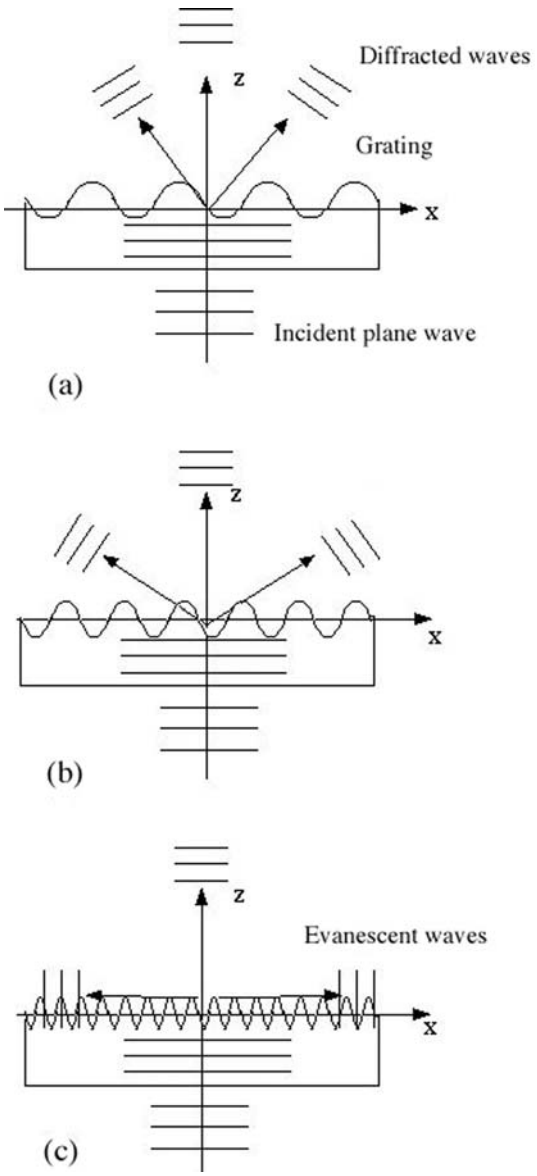

Fig. 3.1. a–b. Light diffraction by grating. As reducing the grating pitch from **a** to **b**, the diffraction becomes steep and finally the diffracted wave runs over the surface **c**. This is called evanescent wave

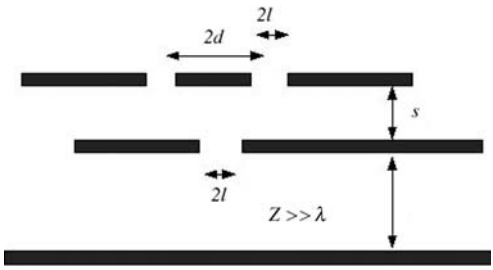

Fig. 3.2. Two-screens model for the Fourier treatment of near-field coupling

In actual cases, the analysis is more complicated. The system including a small optical aperture or a surface with, for example, marks of a specific shape recorded in optical data storage, has to be considered as a combination consisting of many different gratings with different width and spatial frequency. For example, let's assume a system with two different screens close to each other [18–20]. Hence, one screen has a small hole and the second screen has two holes, as shown in Fig. 3.2. First, we have to transform the structures with step functions (hole) in the Fourier optics. The step function of a hole is normally expressed by $\sin(x)/x$. The electromagnetic field on the first screen with two slits is transformed into E_1 and

$$E_1(k_x, z = 0) = 4E_0 \cos k_x d \frac{\sin k_x L}{k_x} \tag{3.1}$$

Hence, the second screen position is taken as $z = 0$, and the two slit distance and the hole diameter are l and d, respectively. E_0 is the incident electromagnetic field. Here, the propagated light field $E_d(x, z = Z)$ towards z direction is described by

$$E_d(x, z = Z) = \frac{1}{2\pi} \int_{-\infty}^{+\infty} \mathrm{d}k_x \exp(-k_x x) E_1(k_x, z = 0) \exp\left[-\mathrm{i}(k^2 - k_x^2)^{1/2} Z\right] \tag{3.2}$$

In far-field optics and normal optical microscope system, Z is far longer than the light wavelength used and one may think about the integration range between $-\omega/\mathrm{c}$ and $+\omega/\mathrm{c}$ because the term $\exp[-\mathrm{i}(k^2 - k_x^2)^{1/2} Z]$ beyond the range becomes real and is rapidly eliminated; the optical near-field is thus the contribution from the outer integrated region. Now, closing in the second screen to the first one with a hole by a distance $s (s < \lambda)$, the near-field integrated term becomes large and effective, and is convoluted as the coupling field. Finally, we can derive the following equation:

$$E_d(x, y = Z) = \frac{1}{(2\pi)^2} \int_{-\omega/c}^{+\omega/c} \mathrm{d}k_x \exp(-k_x) \exp[-\mathrm{i}(k^2 - k_x^2)^{1/2}(Z - s)]$$
$$\times \int_{-\infty}^{+\infty} \mathrm{d}k'_x 4E_0 \cos k'_x d \frac{\sin k'_x L}{k'_x} \exp[-\mathrm{i}(k^2 - k_x'^2)^{1/2} s]$$
$$\times 2 \cos k'_x \mathrm{d} \frac{\sin(k_x - k'_x)l}{k_x - k'_x} \exp(+\mathrm{i}(k_x - k'_x)X)\,. \tag{3.3}$$

The light passing through the first screen generates the field coupling and it is scattered by the second set of slits. In the second term, the spatial frequencies beyond k_x gives the contribution with real exponential term which rapidly reduces as s increasing s; however, the contribution is now a quite large because of the small s is less than λ. As s is smaller, the contribution from $k > k_x$ becomes large. It is the same as if the near-field aperture is close to the surface via SNOM or other technical methods, where the resolution is improved. This is the explanation and basic principle of the resolution improvement by using near-field optics can be explained in terms of Fourier Optics (Fig. 3.3).

The computer simulation based on this principle is now easily programmed by Mathematica$^{\mathrm{TM}}$ or other programs. The simulation results are very simple but educative to understand the behaviors of near-field and its scattering.

In Figs. 3.4 to 3.7, two mark patterns are Fourier transformed and the second screen with a slit moves over the behind the first screen with a constant space d. In the case of $s = 0$ (two screens are in contact), mostly the same pattern of the recorded marks are reproduced. As s increases, however, the edges of each mark are vague and two clear edges are no longer obtained.

By comparing Figs. 3.4 and 3.5, we can see the resolution characteristics in near-field readout. That is, the resolution mostly depends on the observing aperture size and the space d. In Fig. 3.4, the resolution is obtained by $d \sim 2\lambda$, but $1/2\lambda$ in Fig. 3.5. Following the simulations, then, the distance of the slits in the first screen is reduced to the ratio of 1:1. The simulated results are more interesting (Figs. 3.6 and 3.7). Now, the resolution of two slits is no longer obtained even at $1/10\lambda$. In order to improve the resolution, the slit size of the second screen has to be further reduced by 1/5, and the result is shown in Fig. 3.7. Therefore, it is understood that at least the aperture size should be a quarter or less in comparison with the mark size in near-field readout.

As we have learned, the Fourier treatment is very convenient and intuitively understandable, but it consists of scalar calculations. This means that the analysis cannot be applied to more real systems dealing with vector elements, polarization, and multiscattering.

Following the basis of the Fourier analysis of optical near-field and surface plasmoms, let's briefly discuss the experimental methods to generate surface

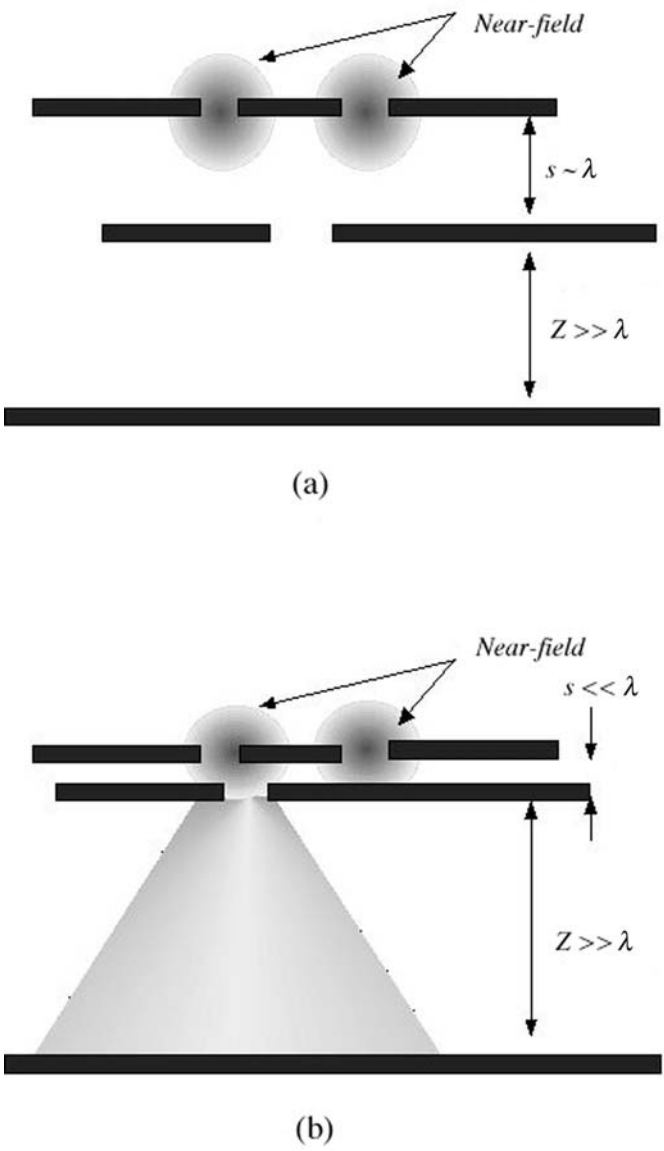

Fig. 3.3. a–b. Intuitive image of near-field coupling of two screens with small slits or apertures. **a** $s \sim \lambda$, the near-field cannot couple with a slit of the second screen. **b** $s \ll \lambda$ the near-field is scattered by the slit and propagated

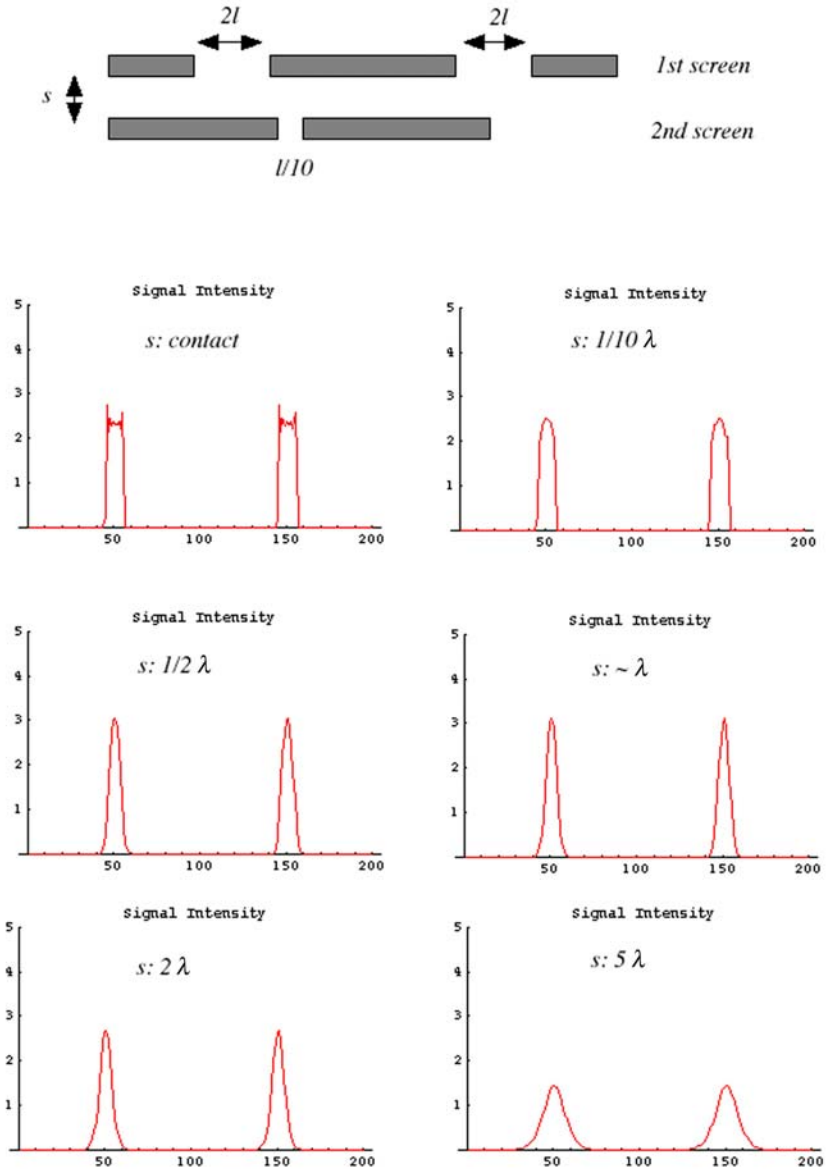

Fig. 3.4. Fourier simulation of two screen problems. Hence, the first screen has two slits and the distance is taken to the ratio of 4:1 (aperture). The slit size of the second screen is 1/5 of that of the first screen's aperture

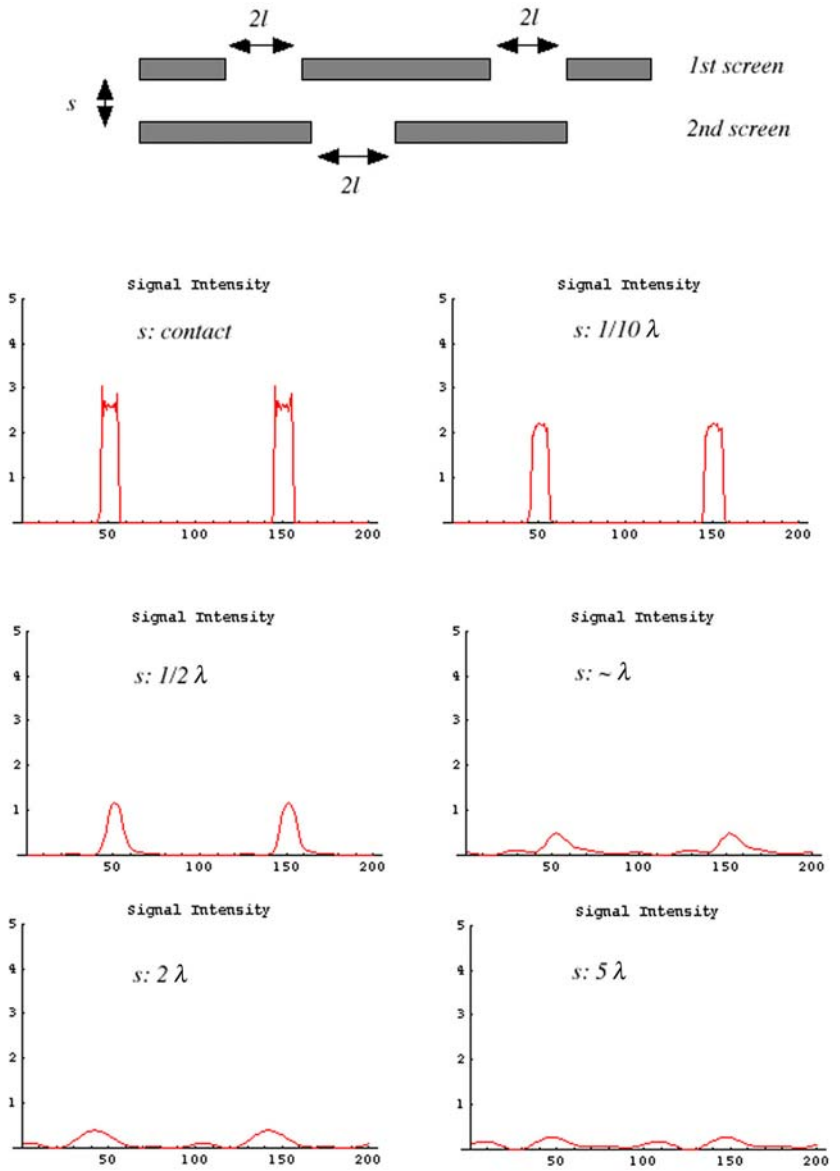

Fig. 3.5. Fourier simulation with a different aperture size. Hence, the slit size of the second screen is expanded to the same size as that of the first screen's slit

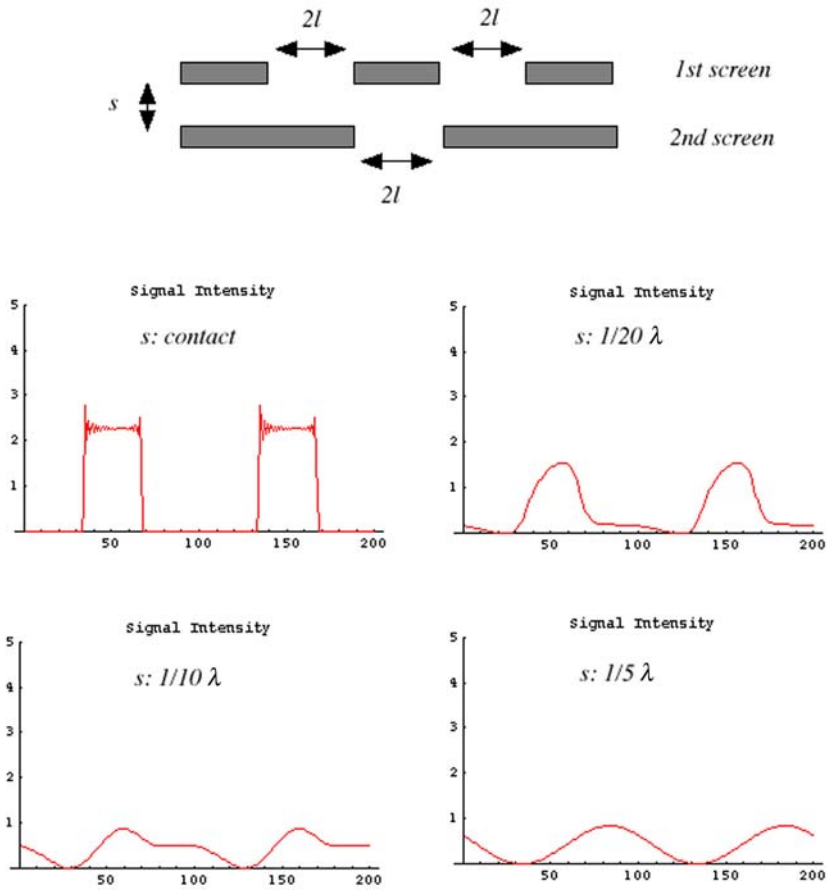

Fig. 3.6. Fourier simulation with the slit duty ratio of 1:1. Hence, the slit size of the second screen is the same as that of the first screen

plasmons [21]. This will be very helpful in the consideration of near-field optical recording later. In fact, there are two main techniques for surface plasmon generation. The simplest method is to use the combination of metal and dielectric thin films fabricated on a prism surface. Hence, we assume that the dielectric constants of the two films are ε_1 (for the dielectric) and ε_2 (for the metal), respectively, and the dielectric film has no absorption, i.e., it is transparent. In a metal or semiconductor, the imaginary part of the refractive index is generally larger than that of the real part, and the dielectric constant becomes negative. Irradiating a light beam onto the multilayer and solving the system with the Maxwell's equations, the electrical field (k_x) along the metal-dielectric film interface is given by

$$k_x = \omega/c\sqrt{(\varepsilon_1\varepsilon_2)/(\varepsilon_1+\varepsilon_2)}\,. \tag{3.4}$$

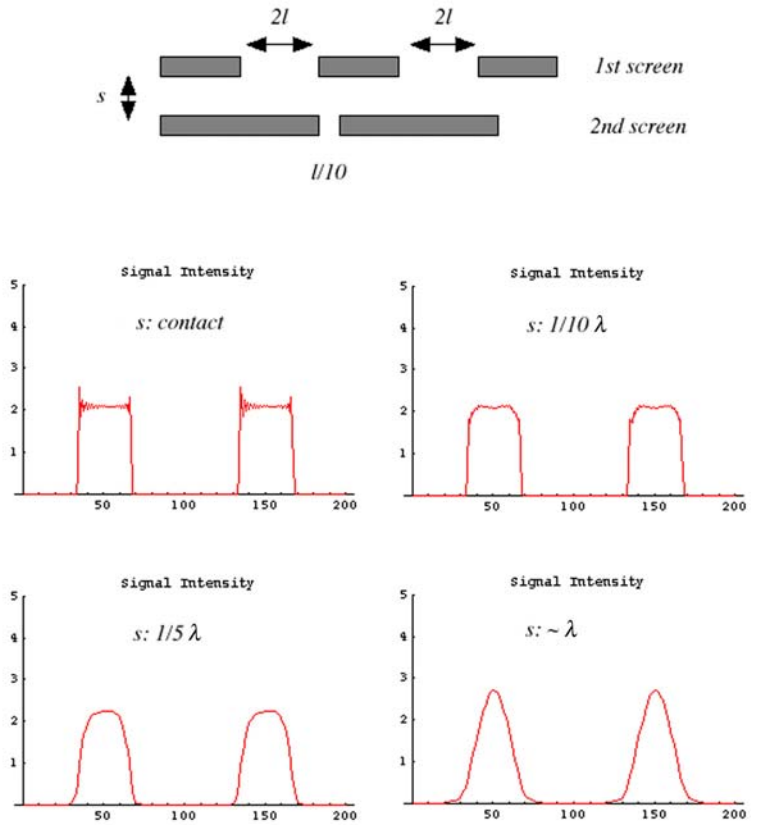

Fig. 3.7. Fourier simulation with an aperture $^1/_5$ the size of that for Fig. 3.6

To trap k_x in the plane, the energy of the reflected or transmitted light (k_z) must be transferred into k_x. In two dimensions, as the total wave vector $\boldsymbol{k}$ must satisfy the equation $k^2 = k_x^2 + k_z^2$: $k_z = [(\omega/c)^2 - k_x^2]^{1/2}$, the imaginary k_z is required because the wave normal to the plane is exponentially reduced by $\exp[-k_z z]$. To satisfy the condition, $k_z = \left[(\omega/c)^2 - k_x^2\right]^{\frac{1}{2}}$ must be imaginary and a large k_x is needed beyond ω/c.

In order to satisfy the condition and generate surface plasmons in the plane, the total attenuated reflection (ATR) method is used in general. Introducing the TM-mode wave into a prism on which the multilayered structure consisting of metal and dielectric thin films is produced, and rotating against the incident wave direction, the best condition to generate the surface plasmons is easily obtained with a strong light absorption. Although the rotating angle of the prism depends on each metal layer and its thickness, approximately, the best condition is found in the range between 40° and 50° (Fig. 3.8).

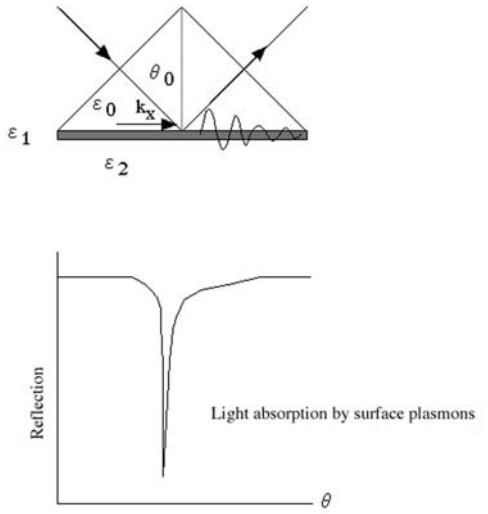

Fig. 3.8. A method to generate surface plasmons by the combination of prism and metal thin film in the Kretschmann–Raether configuration

In optical data storage, however, it is mostly impossible to insert a prism into an optical disc itself to generate surface plasmons. An alternative way is necessary. This can be accomplished by utilizing an optical grating as described above. To generate surface plasmons in the disc, one may notice that recorded marks or pre-recorded pits are used as an optical grating. As already mentioned, when the grating pitch or width is smaller and beyond the limit, the surface plasmons are generated in the grating plane. This is the result in the generation of large k_x due to a small pitch. Hence, ν is a number, a is the grating pitch size, and k_x is

$$k_x = (\omega/c)n\sin\theta \pm 2\pi\nu/a = (\omega/c)n\sin\theta \pm \Delta k_x\,. \tag{3.5}$$

Thus, as the pitch a decreases Δk_x becomes large and finally exceeds (ω/c). If a recording film in which the refractive index changes between the amorphous and crystalline state is used, the surface plasmons are available to increase the signal intensity.

3.2 Computational Analysis Using Finite-Difference Time-Domain (FDTD) Method

The finite-difference time-domain (FDTD) technique has now become one of the powerful numerical simulation methods to solve the Maxwell's equations,

$$\frac{\partial D}{\partial t} = -\sigma E + \nabla \times H \tag{3.6}$$

and

$$\frac{\partial B}{\partial t} = -\nabla \times E\,. \tag{3.7}$$

Up to now several computer simulations to solve the Maxwell's equations numerically have been proposed. Among them, in terms of the model simplicity, effective memory capacities for calculation and speed, and easy treatment of optical constants, FDTD has an advantage over the other methods. In order to apply FDTD to actual optical near-field analysis, including a probe aperture and the interaction with a material, the model has to be divided into 3-dimensional unit cells within electromagnetic vectors (Yee's lattice), and initial conditions: dielectric constant, magnetic permittivity, electric-conductivity, and so on, are attributed to each cell. The FDTD method is applicable to closed systems, and one has to introduce several assumptions not to neglect the wave reflection at the boundaries with absorbers. First, the initial conditions are set, and then $\boldsymbol{H}$ and $\boldsymbol{E}$ are derived numerically after a different time $\Delta t/2$ from the initial time t_0 as well as positions (x, y, z) and $(x + \Delta x/2,\ y + \Delta y/2,\ z + \Delta z/2)$. For example, we assume $\boldsymbol{F}$ as the electromagnetic field, in general, where the differential equations are given as

$$\frac{\partial F}{\partial x} = \frac{F\left(x + \frac{\Delta x}{2}, y, z, t\right) - F\left(x - \frac{\Delta x}{2}, y, z, t\right)}{\Delta x}\,,$$

and

$$\frac{\partial F}{\partial t} = \frac{F\left(x, y, z, t + \frac{\Delta t}{2}\right) - F\left(x, y, z, t - \frac{\Delta t}{2}\right)}{\Delta t}\,. \tag{3.8}$$

In the FDTD method, the position and time are divided into a cell size of (Δx, Δy, Δz) and each node has a label such as ($i\Delta x$, $j\Delta y$, $k\Delta z$, $n\Delta t$). Here, i, j, k, and n are integers. Now, omitting Δ, we define $\boldsymbol{F}(x, y, z, t) = \boldsymbol{F}^n(i, j, k)$ and simply describe the discrete equations

$$\frac{\partial F}{\partial x} = \frac{F\left(\mathrm{i} + \frac{1}{2}, j, k\right) - F^n\left(i - \frac{1}{2}, j, k\right)}{\Delta x}\,,$$

and

$$\frac{\partial F}{\partial t} = \frac{F^{n+\frac{1}{2}}(i, j, k) - F^{n-\frac{1}{2}}(i, j, k)}{\Delta t}\,. \tag{3.9}$$

Hence, the electrical field E is calculated at times of $(n-1)\Delta t$, Δt, and $(n+1)\Delta t$, while the magnetic field at $(n-1)\Delta t/2$, $n\Delta t/2$, and $(n+1)\Delta t/2$. The procedure is repeated by applying one previous time t_{n-1} until the solutions of H and E at every time step are close to a constant. You should be careful that the solutions H and E are sometimes saturated to a different values by giving different time step or domain.

In an actual calculation, as shown in Fig. 3.9a, E^n is derived by using E^{n-1} and $H^{n-1/2}$, and $H^{n+1/2}$ is obtained by using E^n and $H^{n-1/2}$, respectively. Finally, the repeating equations are summarized as

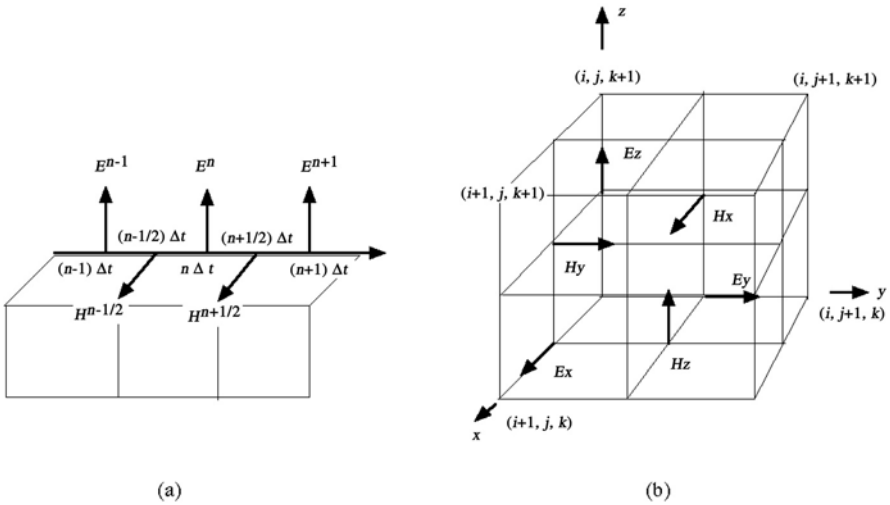

Fig. 3.9. Yee's lattice model and each field setup for FDTD computer simulation

$$E^{n+1} = \frac{2\varepsilon - \sigma\Delta t}{2\varepsilon + \sigma\Delta t}E^{n} + \frac{2\Delta t}{2\varepsilon + \sigma\Delta t}\nabla \times H^{n+\frac{1}{2}} \text{ and}$$
$$H^{n+1} = H^{n-\frac{1}{2}} - \frac{\Delta t}{\mu}\nabla \times E^{n}\,. \tag{3.10}$$

In addition, as shown in Fig. 3.9b, each electrical field and magnetic field is set along each x, y, and z axis (E_x, E_y, E_z), and normal to each plane (H_x, H_y, H_z). Optical constants such as ε, σ, and μ are set at each Yee's cell. The accuracy of the FDTD calculation almost depends on the cell size. The solution is getting close to the real value as the cell's size is smaller and finer. In general, the size should be 1/10, 1/20, or less than a minimum wavelength included in a model.

When the FDTD simulation is applied to models with metals, a careful treatment is required because of divergence. In order to calculate a model dealing with metals such as Au and Ag, one has to transform the dielectric constant described by wavelength or frequency into a form using time domain. That is, (3.12) is transformed to (3.13).

$$\varepsilon(\omega) = \varepsilon_0\left(1 + \frac{\omega_{\mathrm{p}}^2}{\omega(j\nu_c - \omega)}\right) = \varepsilon_0[1 + \chi(\omega)] = \varepsilon_0(n - jk)^2 \tag{3.11}$$

and

$$D(t) = \varepsilon_0\varepsilon_\infty E(t) + \varepsilon_0\int_0^t \chi(t')E(t - t')\mathrm{d}t'\,. \tag{3.12}$$

Hence, ε_0, ω_{p}, n, κ, and ν_{c} are the dielectric constant in vacuum, plasmon frequency, real part of the refractive index, the imaginary part of the refractive

index, and absorption strength, respectively. In addition, $\chi(t')$ is the dielectric susceptibility for the time domain. Using (3.13), (3.11) is then described as the following recurrent expression:

$$E^n = \frac{1}{\varepsilon_\infty + \chi^0}\left(\varepsilon_\infty E^{n-1} + \Phi^{n-1} + \frac{\Delta t}{\varepsilon_0} \bullet \nabla \times H^{n-\frac{1}{2}}\right) \tag{3.13}$$

and

$$\chi^0 = \frac{\omega_\mathrm{p}^2}{\nu_\mathrm{c}}\left[\Delta t - \frac{1}{\nu_\mathrm{c}}(1 - e^{-\nu_\mathrm{c}\Delta t})\right] . \tag{3.14}$$

Here, the relationship between Φ^{n-1} and Φ^{n-1} is connected by

$$\begin{aligned} \Phi^{n-1} &= E^{n-1}\Delta\chi^0 + e^{-\nu_\mathrm{c}\Delta t}\Phi^{n-2} , \\ \Phi^{-1} &= \Phi^0 = 0 , \end{aligned}$$

and

$$\Delta\chi^0 = -\frac{\omega_\mathrm{p}^2}{\nu_\mathrm{c}^2}(1 - e^{-\nu_\mathrm{c}\Delta t})^2$$

According to the mathematical treatment, we can now apply the FDTD method to models including metal surfaces. In the following section, several models and the FDTD simulated results are described [22, 23].

3.3 Several Examples for the FDTD Computer Simulation

It is actually difficult to deal with a quantitative discussion of a 2-dimensional (2-D) FDTD simulation model; however, the model sometimes gives us more intuitive views of the electromagnetic wave behaviors. Additionally, the calculation time and memory requirements are greatly reduced in comparison with 3-D simulation model. Therefore, the 2-D model is still useful to understand the near-field phenomena and to testify several simulation models.

Figure 3.10 shows an example of the electromagnetic field distribution of the optical near-field generated at a small slit (200-nm width) which is covered with an Al thin film (125-nm thickness). Hence, a Gaussian beam (488-nm wavelength) is irradiated. In Fig. 3.10, the electromagnetic field and its Poynting vectors are illustrated. The field distribution and pointing vectors calculated in the TM-mode light polarization is different from those obtained in TE-mode polarization. The beam width passing through the aperture in the TM-mode is nearly the same as that incoming in the aperture. On the other hand, it was found that the width in the TE-mode is much narrower. Repeating the simulation with different aperture size and the metal cover layer thickness, one can obtain the optimized model structure with a high throughput.

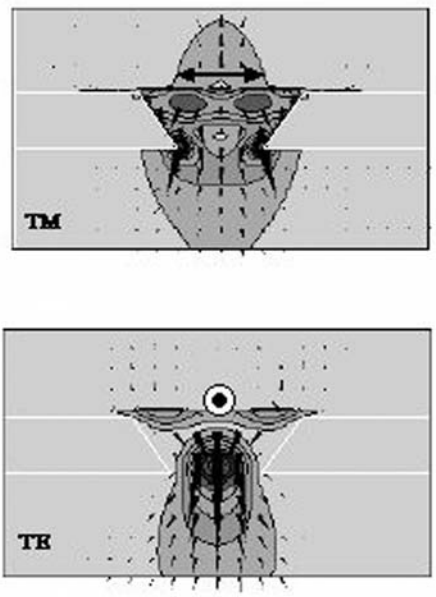

Fig. 3.10. Near-field distributions and Poynting vectors in a small aperture. *Top*: TM waves comes in the aperture, and *bottom*: TE waves. The slit size is 200 nm and Al film thickness is 125 nm. The incident light wavelength is 488 nm and the beam profile is Gaussian

As a second example, the electromagnetic field in a model which consists of optical phase-change recording marks and nanometer-size array fabricated in a Si wafer is shown in Fig. 3.11. Hence, the mark and aperture sizes are equal. A Gaussian profiled beam is radiated from the left-hand side of the figure and the beam transmits the phase-change recording film. The aperture and the recording film are separated by an air space of 25 nm, and then the light is detected by the aperture. Moving the mark position in between t_1 and t_6, it is well understood that the electromagnetic field distribution in the aperture greatly changes. Using 2-D models, we can roughly estimate the behavior and intensity profile of the electromagnetic field, as the model's parameters change. The two models discussed above are the first step of the FDTD simulation, but quite a long time for the calculations is needed. Depending on your model and computer, a Cray C90 machine takes, for example, 3 to 10 minutes to perform the calculations.

As the third model, we should discuss the behavior of surface and local plasmons in the FDTD simulations. As studied in Sect. 3.1, Fourier optics gave us an intuitive image of optical near-field. According to the result, all models can be expressed by the summation of wave functions with low to high spatial frequencies. In order to reconstruct the model exactly, the elements of higher spatial frequencies have to be included. It means that if the model has

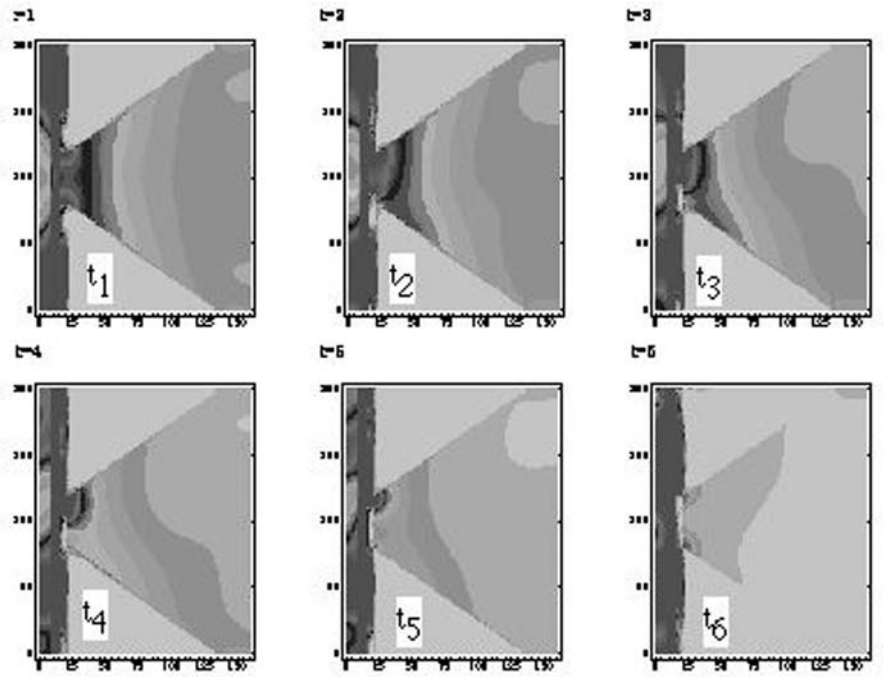

Fig. 3.11. Near-field readout by a small aperture. Hence, the recording film is GeSbTe with a thickness of 20 nm. The air gap between the recording layer and Si aperture slit is 25 nm. The light comes from the left and partly transmits through the recording layer. The transmitted light makes the interaction of the aperture and then comes into the detector. A 200-nm mark moves from the bottom to top between t_1 to t_6

a shaped edge like a probe tip or a boundary of optical constants, the position may have the potential to generate localized plasmons or surface plasmons. Figure 3.12 shows the localized surface plasmons generated in phase-change recording marks in an optical disc. The surface plasmons are clearly identified at two edges of a recorded mark in a focused laser spot. As the mark size gets smaller, plural marks are irradiated in the laser spot. In this case, both marks generate surface plasmons at each edge. As the mark size further decreases, several marks are in the spot and the surface plasmons gradually couple. The plasmon coupling was recently applied as a photonic device.

The final example in 2-D FDTD simulation is a computer model of near-field recording and readout, which is called super-resolution near-field structure (super-RENS). More detail of super-RENS will be discussed. In short, super-RENS normally consists of a multilayered structure with an optical mask layer reducing a laser spot diameter and a recording film. The two active layers are separated by a thin solid film with a near-field coupling space

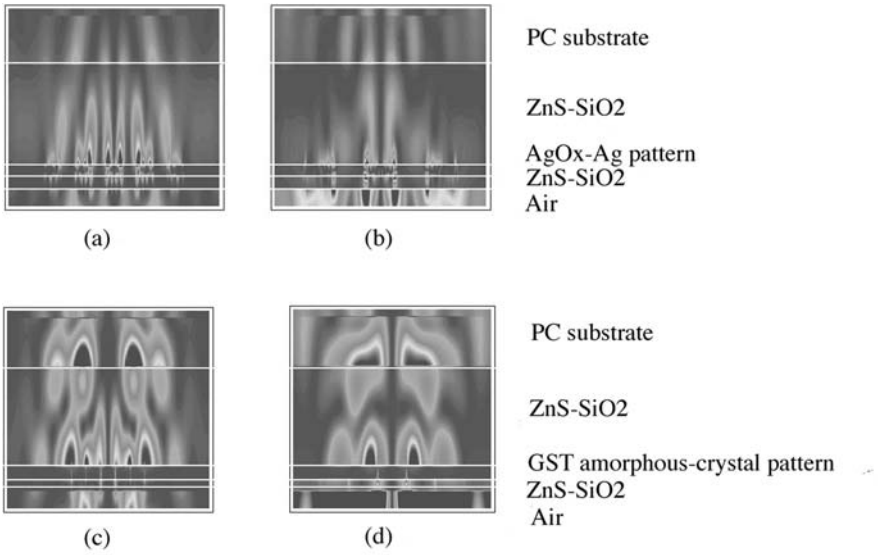

Fig. 3.12. a–d. Evanescent electrical field (surface plasmons) generated at mark patterns. **a** 160 nm mark and space of Ag_2O-Ag and **b** for the 320 nm pattern. **c** 160 nm mark & space of GeSbTe amorphous and crystal phases and **d** for the 320 nm pattern. The model consists of a ZnS-SiO_2 protection layer (170 nm), an active layer (20 nm), and a ZnS-SiO_2 layer (20 nm). The incident light wavelength is 635 nm

(<50 nm). As shown in Figs. 3.13 to 3.15, evanescent wave coupling is identified between small optical aperture and marks recorded in the phase-change film. Recently, several computer simulations and models related to super-RENS have been presented by Japanese, Taiwan, and French groups. Most results are in good agreement with the experimental results, and sometimes it is helpful to understand near-field recording experimental works. However, in order to obtain a better agreement with the experimental results, precise refractive index and thickness of each layer in super-RENS should first be given by the fundamental experiments. In addition, the simulation at the moment is not linked to another simulation analyzing the thermal model. In the near future, both electromagnetic and thermal models will be combined with each other and finally more powerful simulation tools will be available.

Following the 2D FDTD simulations, the 3-D simulation is a much more powerful tool for optical disc analysis. Here, we have a focus on two examples of super-RENS discs with a light scattering center and a gas bubble pit including metallic nanoparticles. Succeeding the super-RENS disc with an Sb film, in which a tiny optical aperture is generated, a second generation super-RENS was developed, in which a nanometer-size light-scattering center is produced as a single light spot. The light-scattering center is thought to be

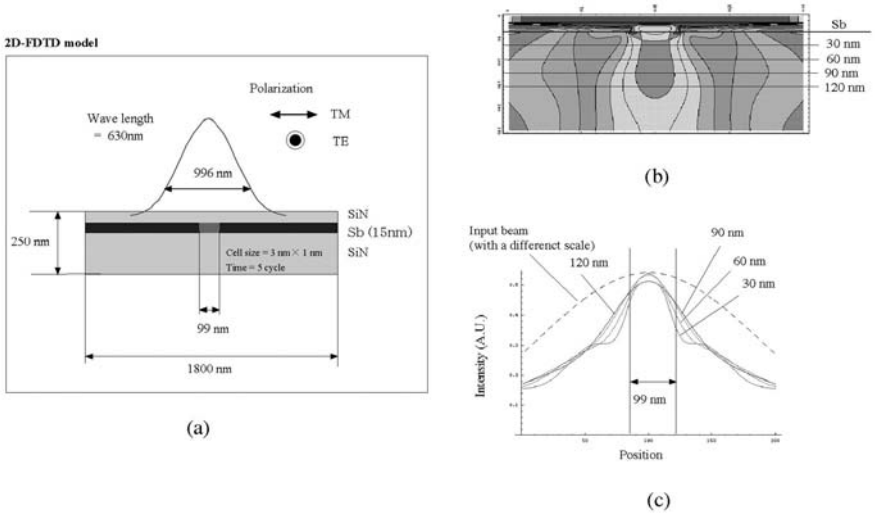

Fig. 3.13. a–c. Two-dimensional FDTD computer simulation of near-field characteristics of Sb thin film and aperture formation. Incident light transmits the 99-nm aperture (amorphous phase). **a** The simulation model. **b** The near-field generated around the aperture (incident light is polarized in TM-mode). **c** Intensity profiles from each aperture position [Courtesy of Mr. A. Sato and Dr. T. Nakano]

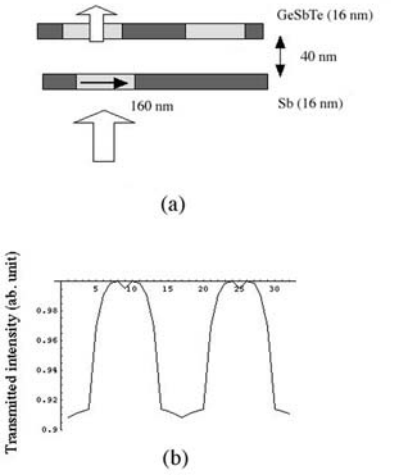

Fig. 3.14. a 2-D FDTD simulation model of super-resolution near-field structure (super-RENS). **b** The transmitted light intensity form the structure

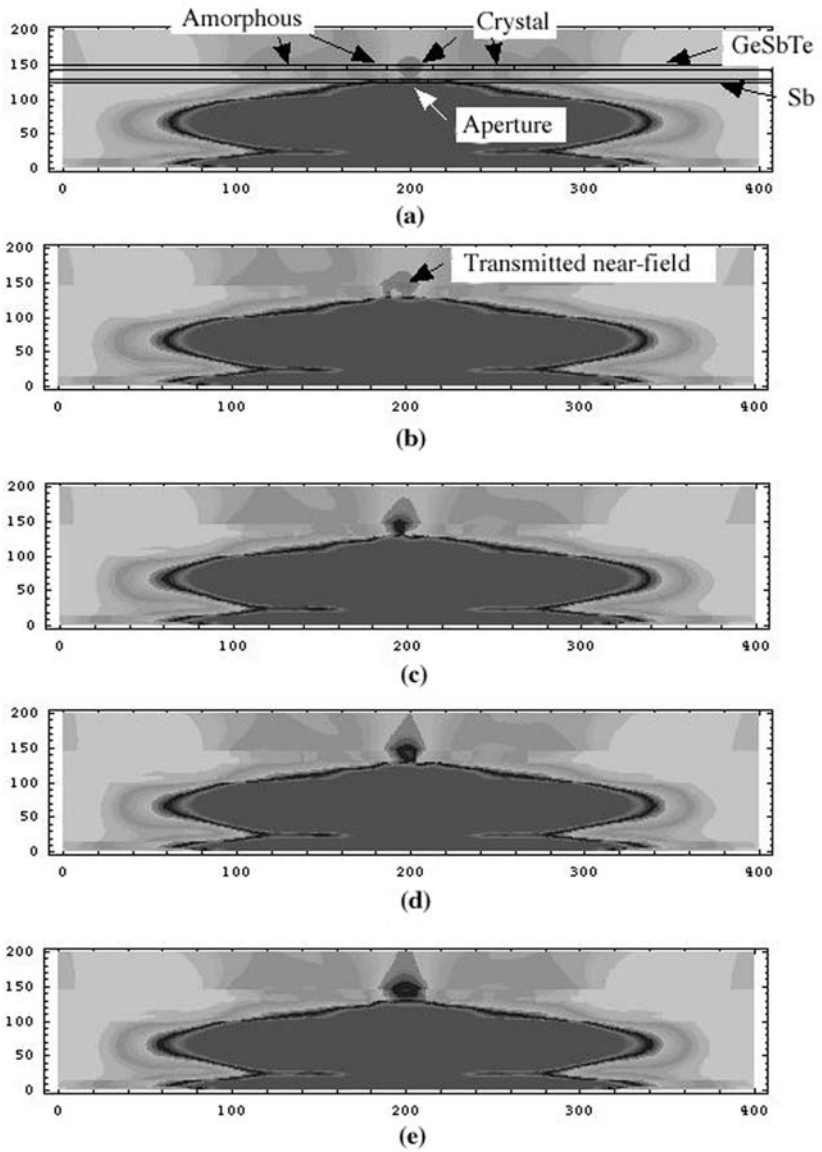

Fig. 3.15. a–e. The time-dependent results of Fig. 3.14. Hence, the recorded mark pattern moves above the aperture. **a** The crystalline area covers the aperture and the transmitted near-field intensity is weak. **b–e** In the meantime, the amorphous area comes in and gradually the near-field scattered to the outside of the disc

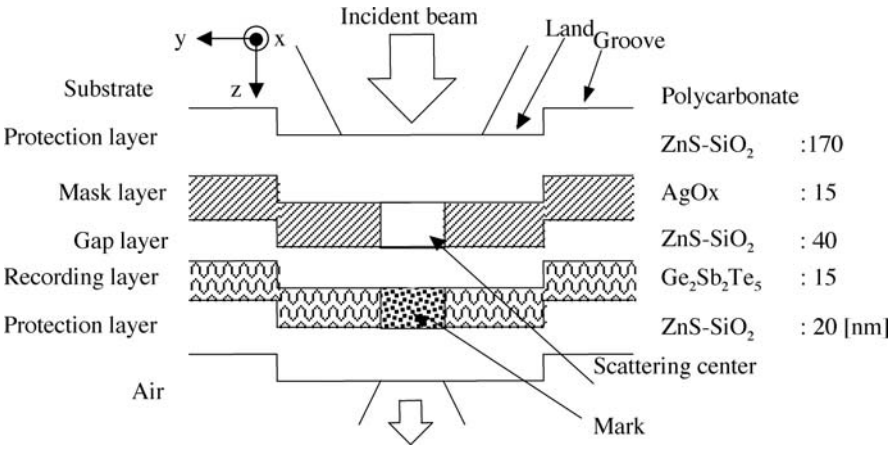

Fig. 3.16. FDTD model for super-RENS disc

a condensed silver particle that is decomposed from a silver oxide thin film. Here, using a super-RENS disc model shown in Fig. 3.16, we can estimate the light intensity profile (Fourier image) on a pupil of a virtual optical pickup lens [24]. The phase-change recording layer and silver oxide (AgOx) layer are separated by a thin dielectric layer (ZnS-SiO_2), and each layer thickness and a groove width (g_w) and depth (g_d) profile are exactly the same as the real layer thickness experimented: ZnS-SiO_2 (170 nm); AgOx (15 nm); ZnS-SiO_2 (40 nm); $Ge_2Sb_2Te_5$ (15 nm); ZnS-SiO_2 (20 nm); g_w (600 nm); and g_d (60 nm), respectively. The optical constants required for the simulation are listed in Table 3.1.

Table 3.1. Refractive indices used in the simulation of Fig. 3.16

Material	Refractive index (n + ik)
ZnS-SiO_2	2.243
AgOx / Ag scattering center	2.661 / 0.7 + 3.65i
$Ge_2Sb_2Te_5$ / recorded mark	4.45 + 1.65i / 4.01 + 3.16i

As it is hard to combine the optical model and thermal model to deal with the chemical decomposition of the AgOx layer, we have to introduce an assumption that a silver light-scattering center is produced in advance and placed in the layer. Then we set 200 nm as the layer thickness of a crystalline-phase mark in an as-deposited $Ge_2Sb_2Te_5$ layer and of the scattering center. The laser beam parameters are set at a wavelength of 650 nm with a polarization across the marks and a lens numerical aperture of 0.60. The results estimated from the model by the 3-D FDTD simulation are shown in Fig. 3.17.

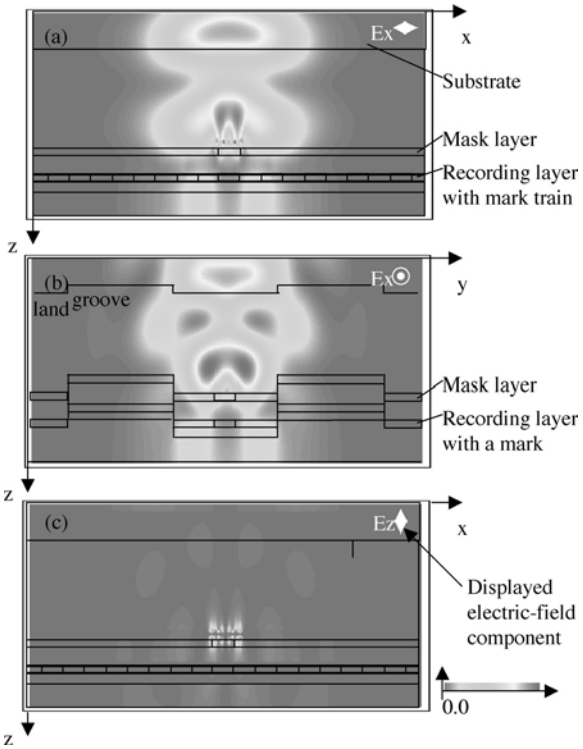

Fig. 3.17. Electrical field distributions of Ex and Ez directions in super-RENS disc shown in Fig 3.18

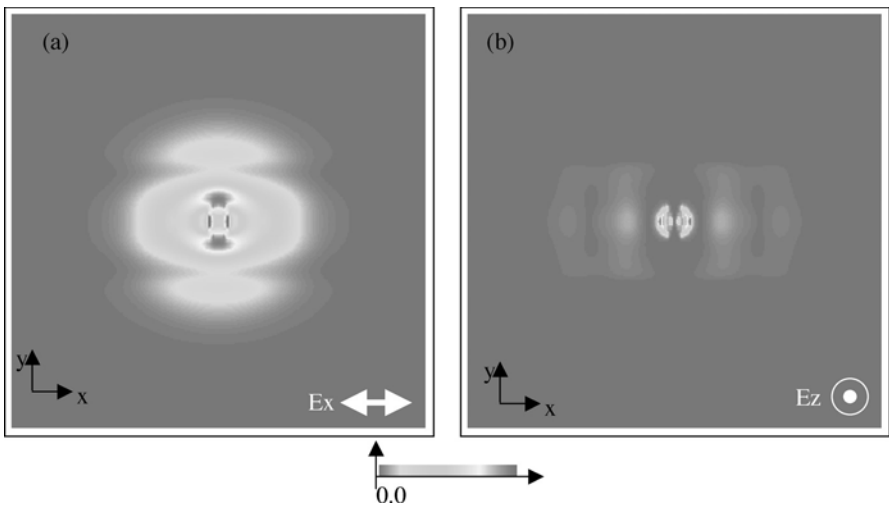

Fig. 3.18. Electrical field distributions in x- and z-directions at around the Ag light-scattering center in the x-y plane

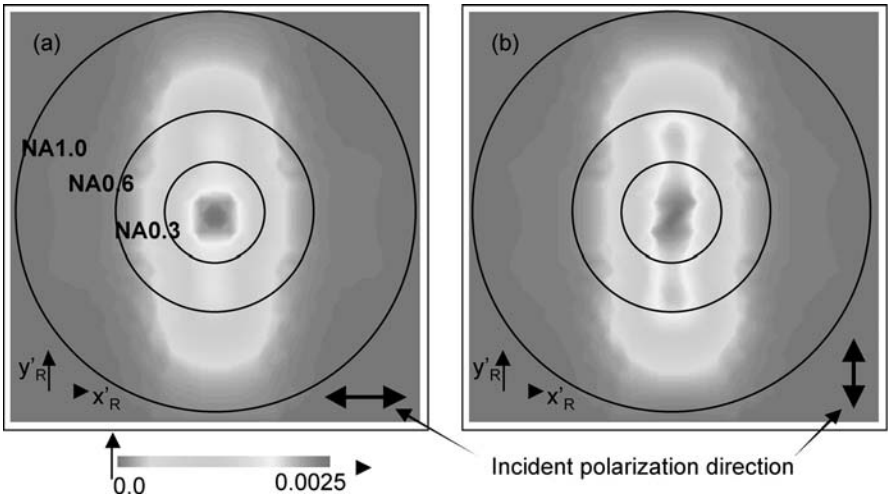

Fig. 3.19. a–b. Reflected light distributions on the pupil plane. The contours show numerical apertures for reproducing signals. **a** Incident beam polarization along the mark trains. **b** Incident beam polarization perpendicular to the trains

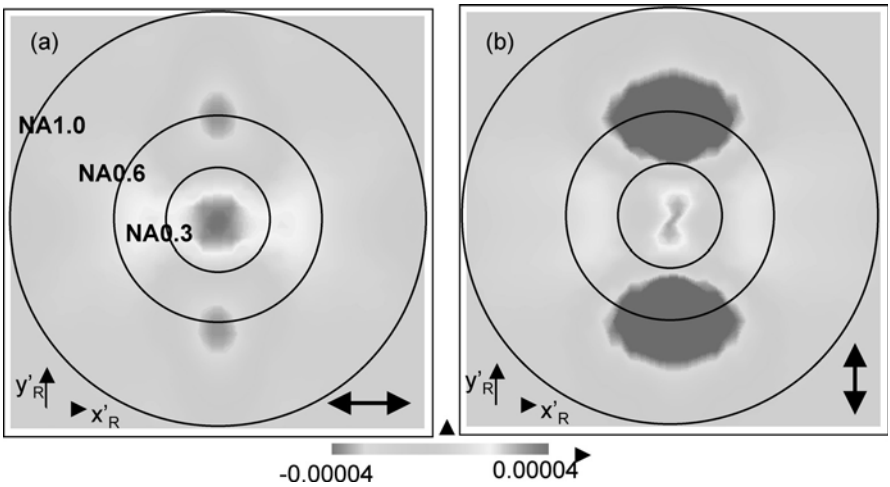

Fig. 3.20. Signal intensity distribution on the pupil plane. **a** Incident beam polarization along the mark trains. **b** Incident beam polarization perpendicular to the trains

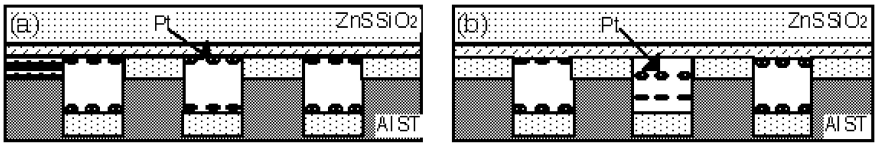

Fig. 3.21. a–b. Simulation model for super-RENS disc with plarinum nanoparticles. **a** Pt nanoparticles have a same configuration in each gas bubble. **b** The central gas bubble has only a condensation

Figure 3.17a shows the electromagnetic wave polarized (Ex) along the track direction, while the intensity along the radial direction is shown in Fig. 3.17b. As shown in the figures, it is found that a strong electric field is generated just above the scattering point. Figure 3.17c, on the other hand, shows the evanescent field (Ez) that exists locally around the silver point. Therefore, it is found that the evanescent field generated by the tiny silver point plays a role like a SNOM probe, which interacts with the phase-change layer to resolute the small marks. Figure 3.18 is the result of the disc plane. Figure 3.18a,b shows the Ex and Ez field generated around the Ag point. Again, the electrical field is strongly trapped around the edge and corners of the point, and depends on the incident beam polarization. From the analysis of the electrical field distribution in the super-RENS disc, we can now evaluate the far-field light intensity returned back to the pupil of the pickup lens. Here, we set the mark size and silver scattering size to 160 nm and 120 nm, respectively. The result obtained shows that the field intensity in the central part of the pupil has a difference on the incident beam polarization (see Fig. 3.19a,b); the polarization has an important role in near-field optical recording. Figure 3.20a,b shows the intensity difference in the case where the mark is just below the Ag point or at an offset point. In the figure, the solid circles indicate lens numerical apertures of 0.3, 0.6 and 1.0, respectively. From the result, for the readout of the super-RENS disc, it is found that a 0.30 NA objective lens is only enough to resolute 160-nm marks.

In the most advanced super-RENS disc, a gas bubble pit including platinum nanoparticles plays a role in the recording carrier and instead the phase-change layer serves as the function of the super-resolution layer [25]. The recorded gas pit by a nano-explosion of platinum oxide (PtOx) is an irreversible pit; thus the super-RENS disc is of a write-once type. Therefore, if a pit trains with the same length and width in less than the diffraction limit is recorded in the disc, the pit cannot be reproduced by itself in the far-field optical system. In order to understand and analyze the behavior of the pits, it is valuable to make several models in such cases. Figure 3.21 is one of the models in which the platinum particles are closely condensed only in a gas bubble pit. This model is based on the theoretical background of thermal distribution in the laser spot and photon pressure. The size of the bubble and each platinum particle are 200 nm and 40 nm, respectively. Each bubble

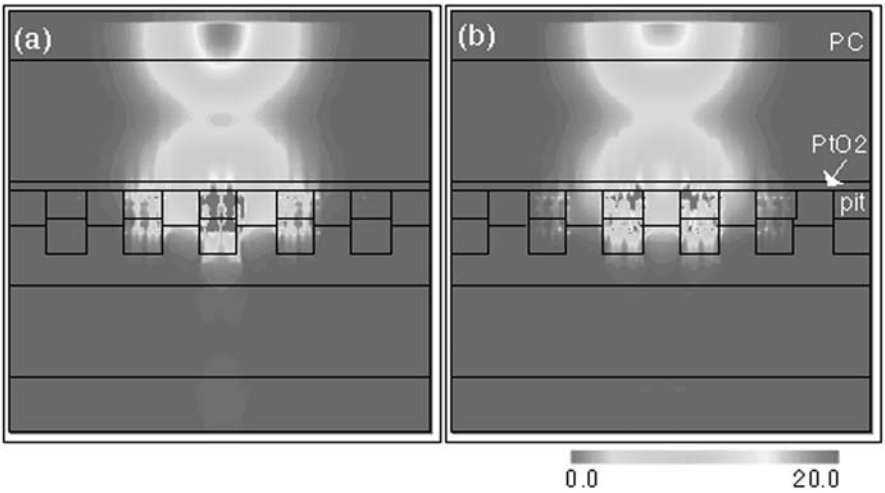

Fig. 3.22. Simulated electrical field intensities of Ex (**a**) and Ez (**b**) directions

includes 6 nanoparticles. Each layer thickness of the model structure is set by the size of the real disc structure. Figure 3.22 shows the estimated electrical field distribution of the model. According to the particle condensation, the central gas pit only exhibits very huge field intensity. From the model, more than 10% modulation of the signal is obtained numerically. In fact, as it is almost impossible to see and understand the electrical field intensity profiles of small marks or gas bubbles beyond the diffraction limit in super-RENS discs by microscopes, the computer simulation methods will become powerful tools in the research and development in the future.

4 Near-Field Recording and Its Actual Methods

Near-field optical recording (NFR) was first proposed and demonstrated by an AT&T group lead by Betzig in 1992 [26–28]. The early stage of NFR was all based on the same technique as that used by the AT&T group, and near-field scanning optical microscope (NSOM). NSOM is a family of scanning probe microscopes (SPM), including scanning tunneling microscope (STM) and atomic-force microscope (AFM), magnetic-force microscope (MFM), and so on. Almost all NFR systems based on SPM hold common fatal disadvantages because the recording speed is on the order of 10 µm/s and the scanning area is limited in a small region of at most $100 \times 100\,\mu m^2$ (see Fig. 4.1). The disadvantages resulted in the scanning units consisted of piezo-scanning elements and the resonance quality factor of an SPM probe.

It is mostly hard to overwhelm the properties unless the system is replaced by alternative breakthroughs. As already discussed in Chap. 2, data transfer rates with more than 20 Mbit/s are required to record and reproduce actual movie pictures in DVD. This means that the SNOM scanning speed is 1/1,000,000 as slow as that of the current optical data storage technology. However, the impact of NFR has attracted a lot of researchers and engineers who have engaged in optical data storage projects because of the diffraction-limit-free recording and readout. Following the pioneering work, several groups have demonstrated the same sorts of NFR by using NSOM based technologies [29–32]. Up to now, the recording and resolution limit of 60-nm size was certainly confirmed on MO and phase-change recording thin film, but unfortunately, little progress has been done in the recording area and speed, using fiber probe heads. Alternative technologies, instead, have been proposed and developed with specially designed lens and thin film technologies. In this chapter, we introduce and discuss three different technological approaches to overcome the optical diffraction limit for NFR.

4.1 Fiber Probe and Flying Head Technologies

The most basic method first introduced was to directly apply the NSOM system itself for NFR. Using a metal-coated fiber probe on top of which a small optical aperture or window is fabricated by pushing on a hard material surface or by cutting off using focused ion beam (FIB), NFR was carried out [33].

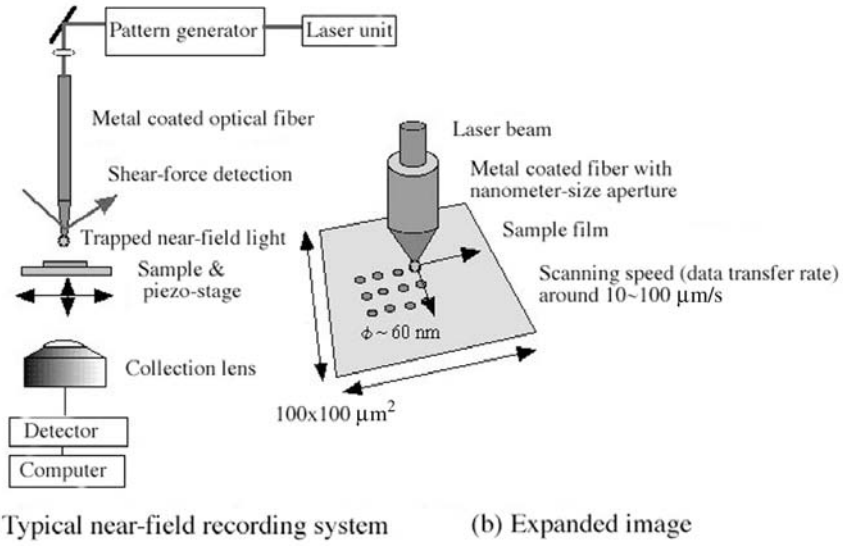

Fig. 4.1. a–b. Schematic pictures of near-field optical recording depending on scanning probe microscope system. **a** The basic optical setup and detection method. **b** The first recorded mark size and typical recording conditions by scanning near-field optical microscope (SNOM)

However, even at the moment, aperture fabrication error is quite large and several wet-etching procedures are required. In addition, a fiber probe made of glass or plastic is very fragile; therefore, the tip is soon damaged by contact or crash with a recording film, when the disc is rotated at a high speed. Furthermore, the light throughput from the aperture is rapidly reduced with the size, and only less than 10^{-3} is available for a 100-nm aperture (10^{-5}–10^{-4} for 20-nm aperture) in readout (see Fig. 4.2) [34]. The low throughput against the input results in the length of the fiber to the laser source; the aperture shape and design greatly affect the efficiency. From the long history of hard disc drive technology, protrusions or tips should be eliminated from the bottom of the slider head because of the head crash [35–37]. Therefore, the method in its present state will probably be not applicable to NFR.

Since the middle of the 1990s, the application of fiber probes to NFR have gradually shifted toward flying-type NFR in order to increase the light throughput from the aperture. To improve light energy loss (throughput) in fiber probes, one simple method is to shorten the fiber length. Several groups have examined and actually designed improved NFR heads (Figs. 4.3 and 4.4). The heads were fabricated by micromachining technology using Si wafers. Here, near-field apertures were produced by anisotropic wet etching process, using the different etching rates between the (111) and (100) faces. Finally, an Al or Ag film was deposited on the surface. The aperture angle

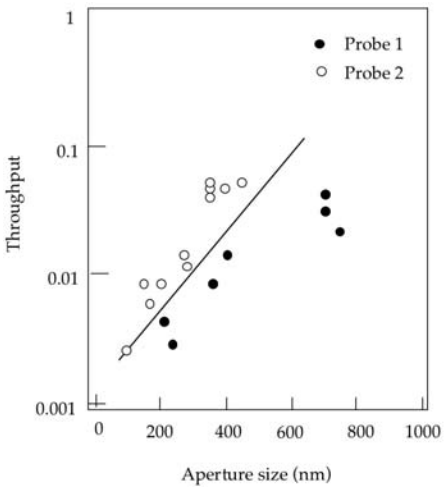

Fig. 4.2. Optical throughput from small apertures fabricated by Si wet etching process. A 670-nm laser beam was focused by a 0.4 *NA* lens and the throughput was detected at the bottom of the apertures. Reprinted by permission of the publisher [34]

was rigidly defined to be 70.5°, and the size was controlled by the wafer thickness and a starting mask size for photo or electron beam lithography (see Fig. 4.5). This slider head is very flat and many apertures are fabricated at the same time by controlling the etching time. The aperture size error has recently been modified by precision-controlled wet processing; but it is still not enough for 1 Tbit/in^2 NFR (approximately 20-nm mark size is required).

An alternative way to make a fixed size aperture is to drill a hole or slice the probe tip directly and physically using a focused ion beam (FIB) [35, 37, 38]. This is not an easy task for the industrial application, although round or square apertures with very sharp edges can be fabricated. Figure 4.6 shows an example of FIB aperture fabrication, and a 200-nm aperture was produced on the facet of a very small aperture laser (VSAL) designed by Partovi et al. [38]. The head can take off a MO or phase-change recording medium surface at a high speed. The laser was metal-coated and a small aperture with a diameter of 200 nm was fabricated by the FIB technique. The laser unit was installed on a hard disc flying head. The recording disc was of the phase-change type. The space between the head aperture and the surface of the disc was fixed at 75 nm and 250-nm marks were recorded and reproduced. The recording density was about 7.5 Gbit/in^2 (Fig. 4.7). However, after reducing the aperture size to less than 50 nm, the throughput rapidly dropped below 10 µW (the input power was 1.25 mW), and no marks were recorded.

Issiki et al. fabricated another type of the flying aperture on a small pyramidal tip surrounded by 4 slider pads (Fig. 4.8) [32]. Two different pyramidal

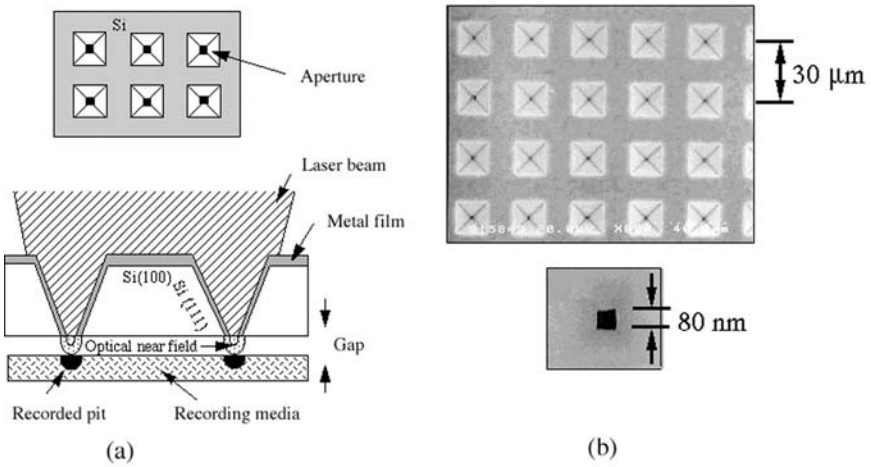

Fig. 4.3. a–b. Small-size apertures for NFR fabricated by Si processing. **a** Aperture design and recording schematic. **b** Scanning electron microscope (SEM) images of the apertures in our group. Reprinted by permission of the publisher [34]

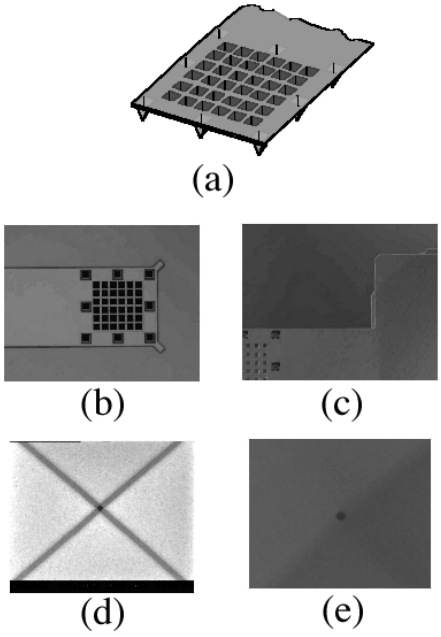

Fig. 4.4. a–e. Flying near-field head with 6 × 6 array apertures designed in LAOTECH. **a** Schematic picture of the array head, **b** and **c** are the SEM images, **d** and **f** are the soom images of each aperture. Each aperture size was 60 nm. Courtesy of Dr. C. Mihalcea

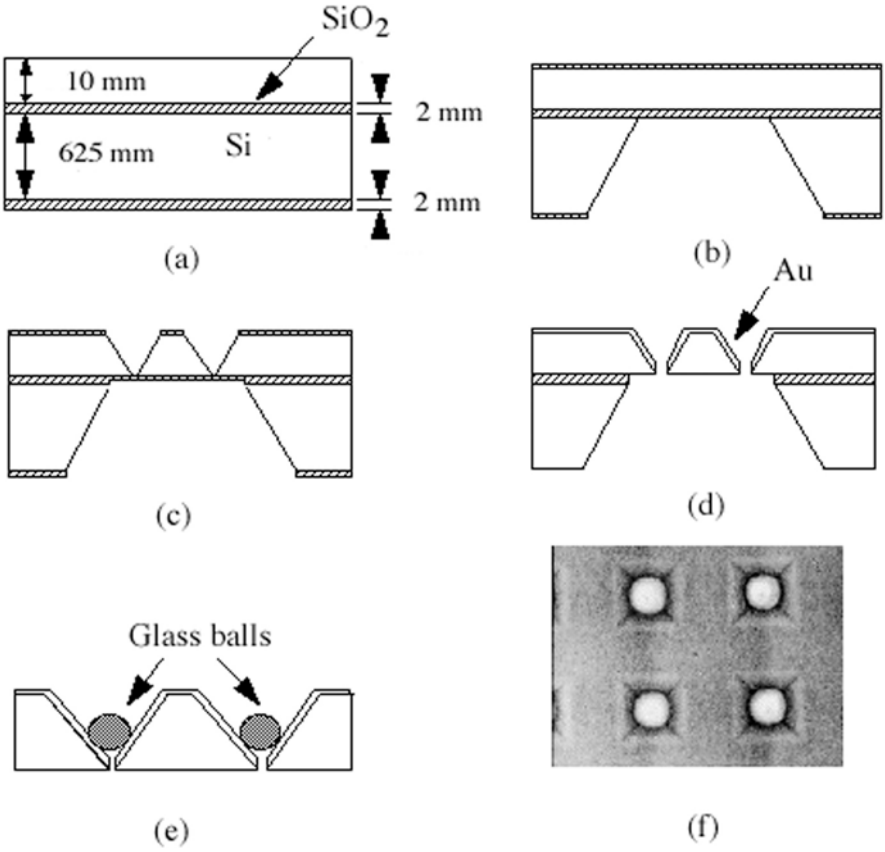

Fig. 4.5. a–e the fabrication process of near-field aperture array in Fig. 4.3 by wet etching method. **f** The SEM image. Here glass balls are placed in the apertures to further enhance the throughput. Reprinted by permission of the publisher [36]

apertures were designed with a single angle of 45° or with double angles of 15° and 75° in order to improve the light throughput. After the deposition of a Pt metal protection layer on the slider, the apertures were fabricated by FIB, and each size was approximately 150 nm (throughput ∼0.5%) for the single type and 50 nm (throughput ∼0.14%) for the double type. Introducing a 650-nm wavelength laser and focusing the beam by a 0.6 *NA* lens, line & space patterns were actually observed. The transmitted signals were monitored at the same time. The resolution of line & space was about 250 nm, and a 125-nm resolution was resolved at the minimum by using their flying head. The scanning speed of the head relative to the pattern was 150 rpm (liner velocity 0.38 m/s). The carrier-to-noise ratio (*CNR*) was 37 dB for the 250-nm line & space pattern. Yatsui et al. on the other hand, fabricated the same sort of the pyramidal flying aperture array, and measured the record-

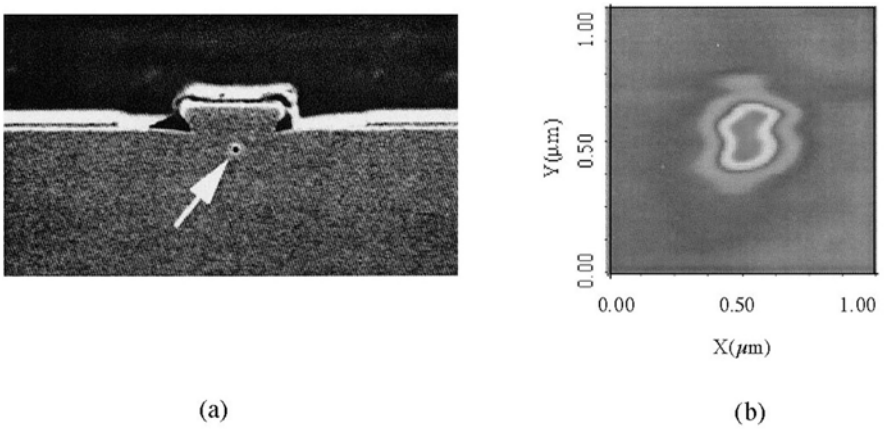

Fig. 4.6. a–b. A near-field aperture (200 nm) fabricated by a FIB process at the facet of very small aperture laser (**a**) and the light throughput (**b**). Reprinted by permission of the publisher [38]

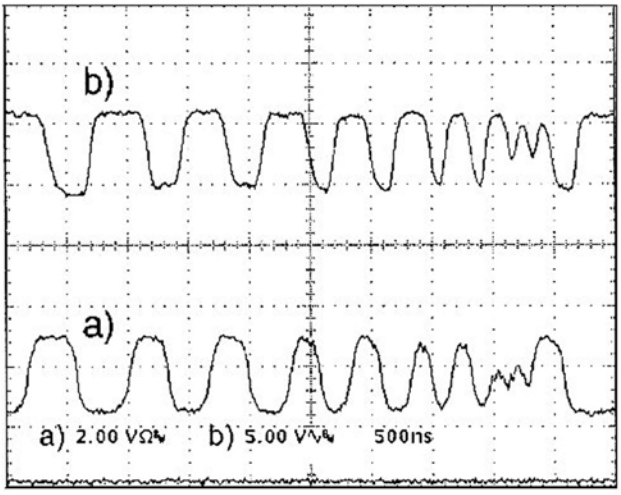

Fig. 4.7. a–b. Flying recording and readout carried by Partovi et al., with VSAL. **a** The refraction signal. **b** The transmission signal. The recorded mark pattern size was 250 nm, and the *CNR* was 45 dB. Hence, a (2,7) run-length limit (RLL) pattern was used. The estimated storage density was 7.5 Gb/in^2. Reprinted by permission of the publisher [38]

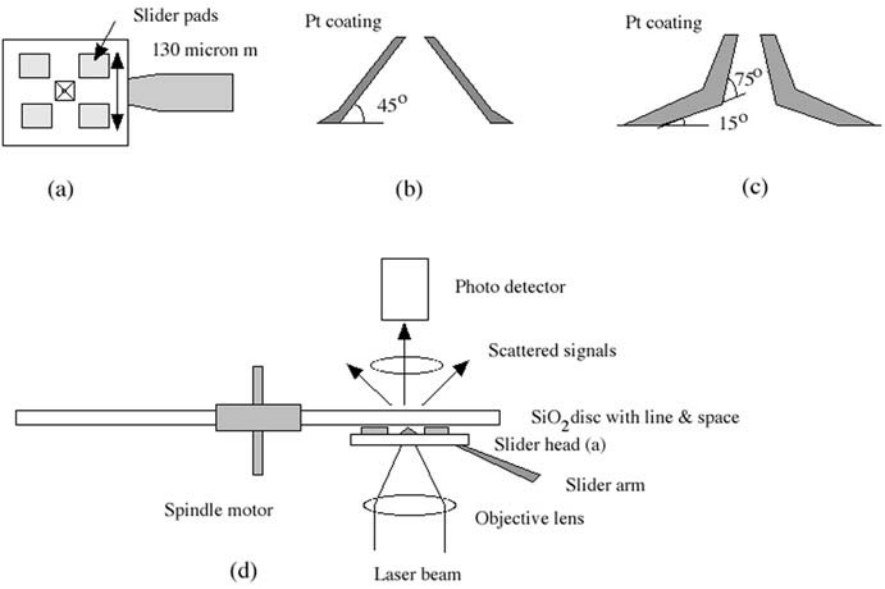

Fig. 4.8. a–d. Flying aperture (**a**) designed by Issiki et al. They compared two different aperture properties with **b** and **c**. The inside apertures were filled with SiO_2. The experimental setup is shown in (**d**). (Drawn on the base of [32])

ing and readout characteristics on a phase-change film (AgInSbTe) [39]. The experiment was carried out in contact-mode, and the space between the pad and pyramidal tip was fixed at 10 nm. Even using a 830-nm wavelength laser, 110-nm marks were read out with a *CNR* of 10 dB.

Goto et al. have proposed further advanced near-field flying heads in combination with vertical cavity surface emitting laser (VCSEL), and their technological challenge towards TB memory is very active but still underway (see Fig. 4.10) [37].

As shown in the pioneering works, it is soon understood that the improvement of light throughput is one of the technological obstacles in aperture-type NFRs. In order to produce optical near-field light effectively, Martin et al. proposed an alternative NFR not using or fabricating a small aperture, but using a metallic cantilever that was illuminated by a focused laser beam [40]. On the basis of the dipole-dipole coupling between localized surface plasmons at the metallic tip and recording medium, further strong optical near-field enabled a better resolution up to 256 Gb/in^2. Several groups have recently simulated the characteristics of the light-scattering type NFR. Matsumoto et al. proposed the dipole-dipole antenna consisting of two triangle metal plates in which the gap was approximately less than 10 nm [41]. According to the computer simulation, it was found that the electrical field intensity was localized and enhanced 3,000 times as large as the case without the an-

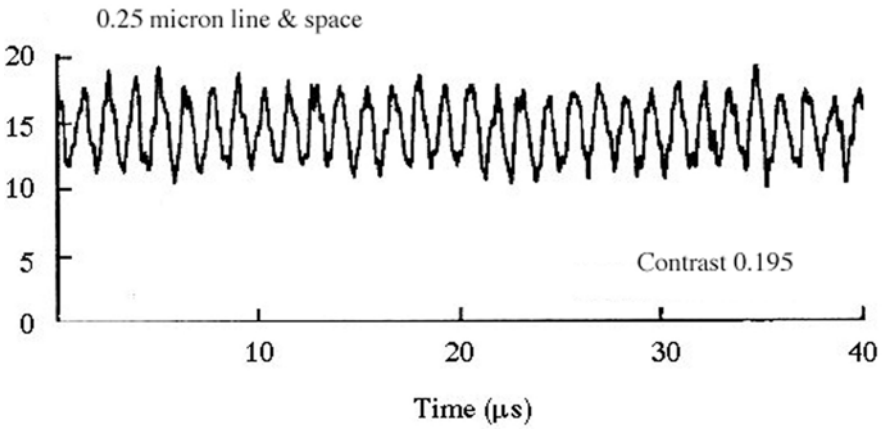

Fig. 4.9. The resolution of the 0.25-μm L& S pattern read out by Issiki et al. The disc rotation was 150 rpm (linear velocity 0.38 μm/s). The wavelength and objective lens *NA* were 650 nm and 0.8, respectively. Reprinted by permission of the publisher [32]

tenna. (Fig. 4.10). However, the gap between the antenna and the recording medium has to be much narrower than that using an aperture; the effective gap is nearly the same as the antenna gap [42]. This approach is very interesting at a glance, but technically it is more complicated than any other NFR systems because the sharp edges melt and diffuse into the substrate due to the heat generated by the enhanced and absorbed light energy. If the antenna size is very small, the quantum effect decreases the melting point and the surface tension soon makes the edges round. Although many problems are involved the systems using the dipole-dipole enhancement or antenna will be installed in the flying-type NFR technology in the future. In addition, we should consider the toughness of the small apertures. It is a more important factor, especially the aperture fabrication by micromachining technologies. Most studies in fabricating the flying head give little consideration to air pressure enforcing on the flying pad and the bottom of the aircraft. As is well-known in hard disc technology, the relative speed between the head and disc is similar to the relationship between the runway and a jumbo-jet at a speed of about 900 km/h. In almost all flying heads designed for the NFR so far, unfortunately, the apertures are probably broken, before taking off against the air high pressure and unstable turbulence. More serious problems in such NFRs will not provide the exchangeability of optical discs between two drives for users.

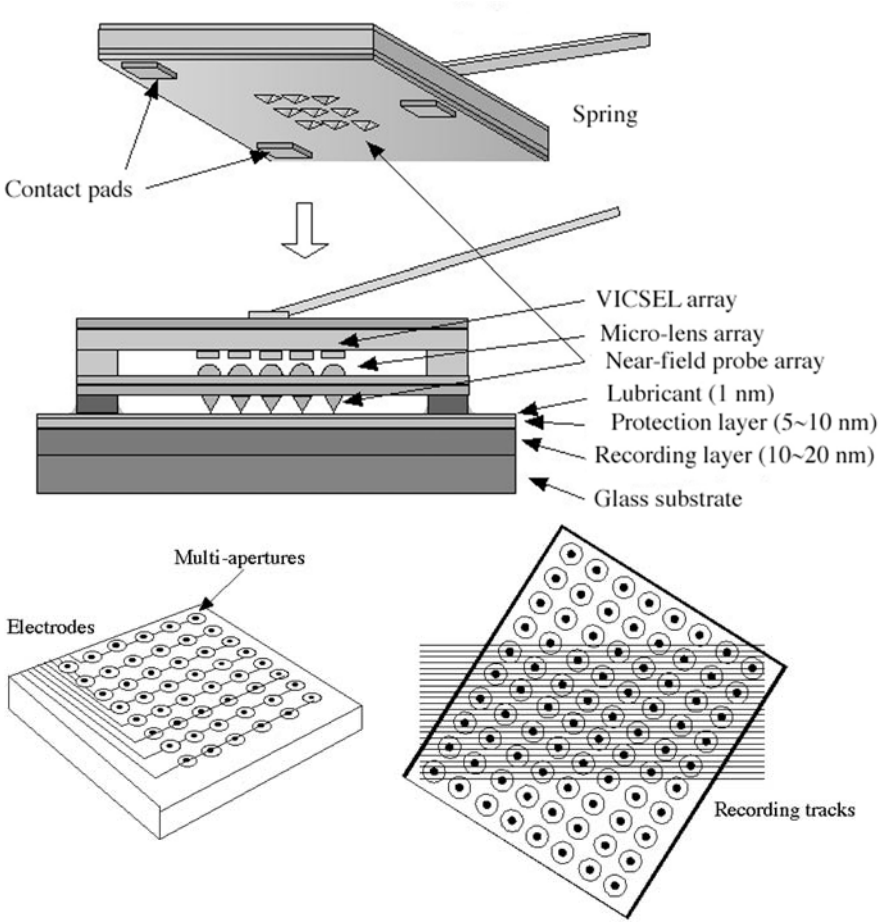

Fig. 4.10. a–c. Future NFR flying head within vertical cavity surface emitting laser units. **a** Whole unit. **b** Bottom structure multi-array apertures. **c** The tracking method. Reprinted by permission of the publisher; courtesy of Professor K. Goto [37]

4.2 Solid Immersion Lens (SIL) and Its Related Technologies

As is well known, a laser spot size, d, on a medium by a focusing lens is given by using the refractive index, n, of the medium, the wavelength, λ (here, the effective wavelength in the medium with n is expressed as λ/n), and the focusing angle, θ:

$$d = 1.22\lambda/(n \sin\theta)\,. \tag{4.1}$$

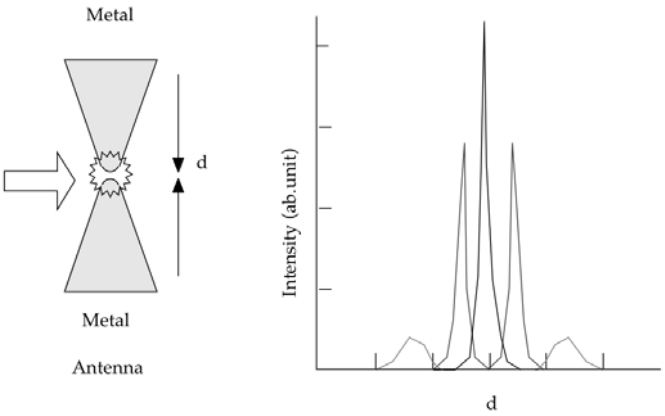

Fig. 4.11. Dipole-dipole antenna using metal triangles. The electromagnetic field enhancement is increased by reducing the space d. If d is large, the field around the two edges are enhanced, but it is merged at $d < 20\,\mathrm{nm}$

In general, $n \sin\theta$ is the numerical aperture NA. In order to decrease the size d, therefore, you have to use a laser source with a shorter wavelength and a lens with a higher NA. If the experiment is done in air ($n = 1.0$), the minimum d is $1.22\,\lambda$. In the medium with $n \neq 1$, however, d can be further small depending on $1/n$. Realizing such a condition with n higher than that of air has long been done in optical microscopes; for example, oil or water is often used to fill a gas between an object and a lens that is specially designed in such observations. In the systems, NA can be improved up to approximately 1.2. This technique has recently been applied to optical microlithography. The technique with a high NA is probably applicable to realize ultra-high density optical data storage as well. However, the difficulty to rotate an optical disc in liquid has been a big technological issue to the real application.

Kino et al. provided the first approach in the early 1990s by using a solid immersion lens (SIL) [43]. The optical setup is given in Fig. 4.12. Two lenses are combined to focus a laser beam on the bottom surface of a hemispherical lens by adjusting the position of another objective lens. Under the condition, the beam passing through the objective lens hits the normal to hemispherical lens surface and is focused on the bottom, preserving the light passing from the objective lens. The optical device works like the immersion lens system in liquid and d is reduced with a ratio of $1/n$ if the hemispherical lens has a refractive index of n.

The light output from the optical device is subjected to the Snell's law. As a result, the light within the internal total reflection ($n \sin\theta < 1$) can propagate in far-field if the lens bottom surface makes contact with air. Even in this case, the NA outside the SIL satisfies $n \sin\theta$. The spot size that is generated by the far-field propagating light may have the same focusing depth

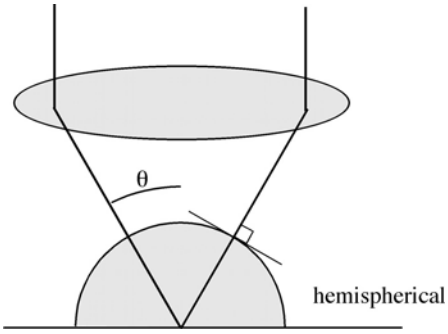

Fig. 4.12. Typical solid immersion lens (SIL) using a hemispherical lens

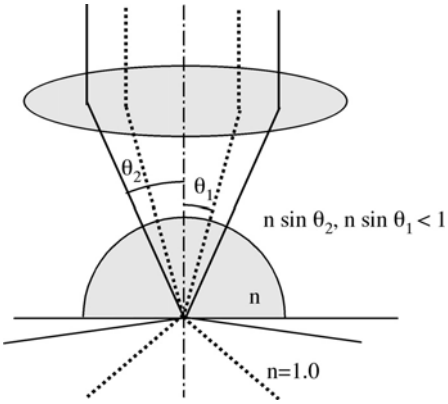

Fig. 4.13. The light pass in the SIL device

across the propagation direction as well as normal lenses. The maximum output NA then becomes 1. In contrast, the light beyond the internal total reflection ($n \sin\theta > 1$) generates evanescent waves at the interface between the SIL bottom surface and air. The wave vectors on the bottom surface and in air are coincident; it means that the spot appearing on the SIL bottom is reduced by the focus size inside the SIL. However, the evanescent field is not a propagating field because of the imaginary wave vector, and the intensity exponentially decreases with distance (Fig. 4.13). Therefore, a small spot with the same size as that generated inside the SIL only exists at a region extremely close to the bottom surface, and the spot size becomes bigger as it moves apart from it. If a medium with a refractive index of n' is inserted, the incident light is coupled with a surrounding medium (refractive index, n) by the Snell's law; the light in a region between $n \sin\theta < n'$ can propagate in the medium as far-field.

Mansuripur et al. and Kino et al. studied the spot size variation against a distance between an MO medium and SIL by use of the vector analysis

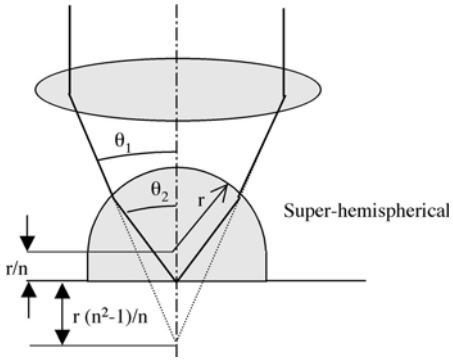

Fig. 4.14. Super-hemispherical SIL

method applied to high density MO recording [44–46]. Using a wavelength of 780 nm, *NA* of 0.7 and assuming an SIL refractive index of 2.0, it was found that the spot size in the SIL is still preserved by around 200 nm apart from the bottom, while the intensity decreases by 1/3.

In the special case that the incident light is only limited in the waves producing the total internal reflection, the evanescent waves are only generated outside the SIL bottom. Therefore, no coupling occurs with far-field lights, and the small spot size is still preserved by the same distance as the wavelength [45], while the intensity drops exponentially. In addition, the incident light given by an annular illumination generates the spot subjected to the 0-th order Bessel function, J_0, which increases a side lobe.

In order to induce the maximum ability of the SIL, the gap control between the bottom surface and the medium is thus very important in addition to the precise adjustment in the SIL device.

4.2.1 SIL with Super-Hemispherical Lens

The SIL devices using a hemispherical lens must have the configuration in which the focus of the objective lens is coincident with the center of the hemispherical lens bottom. Therefore, the device using a higher *NA* objective lens makes the working distance shorter; the hemispherical lens must be smaller. Thus, the manufacturing process and positioning is harder. In order to eliminate such problems and further improve the *NA*, super-hemispherical lenses have been designed and proposed. Figure 4.14 shows the configuration.

The super-SIL devices are designed with an aplanatic point, which is applied to usual lens designing. As shown in Fig. 4.15, let's consider a sphere with refractive index, n is placed in a uniform medium ($n = 1$) and the sphere has a focal point. If a real image A exists inside and its imaginary one exists outside, A', and a point M is given on the sphere, the following relationship must be satisfied:

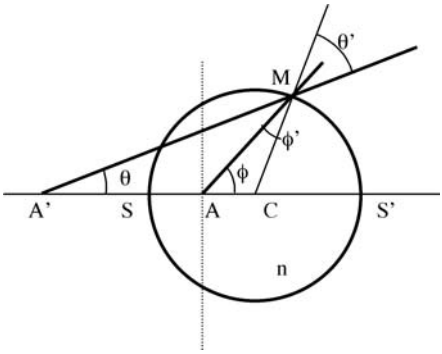

Fig. 4.15. Focal image points inside and outside medium with refractive index, n

$$nMA - MA' = 0 \tag{4.2}$$

or

$$MA'/MA = n\,. \tag{4.3}$$

It means that both light paths have to be equal in length. Therefore, if we consider a line AA', the point M is restricted in the circle region between S and S'. Here, S and S' are the points to divide AA' into the ratio of $1/n$ and n, respectively: the surface is called *Apolonius circle*. Then assuming the circle center, C, and radius r, CA and CA' are given by

$$CA = r/n \text{ and } CA' = rn \tag{4.4}$$

because

$$SA'/SA = (CA' - r)/(r - CA) = n\,, \text{ and}$$
$$S'A'/S'A = (r + CA')/(r + CA) = n\,.$$

Also, introducing the incident light beam angles in the vicinity of the circle, θ and ϕ, respectively, we obtain

$$\sin\phi/\sin\theta = MA'/MA = n\,, \tag{4.5}$$

and the effective NA of the SIL is finally obtained by

$$NA_{\text{eff}} = n\sin\phi = n^2\sin\theta\,. \tag{4.6}$$

From (4.6), the super-SIL can give n times as large NA_{eff} as that of a hemispherical SIL. However, as the super-SIL accompanies the diffraction on the super-hemispherical lens surface, the focused spot size in the lens is restricted by the incident angle θ. As discussed in the above section, assuming the incident angle to the super-hemisphere is θ' and its diffracted angle is ϕ', the Snell's law at the interface gives,

$$n \sin \phi' = \sin \theta \,. \tag{4.7}$$

The condition that the light transmission in the lens is

$$\sin \theta' < 1 \,, \tag{4.8}$$

and at triangles CMA and CMA',

$$CM/CA = r/(r/n) = n \,, \quad \text{and} \quad CA'/CM = nr/r = n \tag{4.9}$$

must be satisfied. That is,

$$\theta' = \phi, \ \phi' = \theta \,. \tag{4.10}$$

As a result, using (4.9) and (4.10), (4.11) is given by

$$\sin \theta' = \sin \phi = n \sin \theta < 1 \,. \tag{4.11}$$

Therefore, for the incident light beam into the super-SIL, the NA is scarified and limited to $1/n$. The incident light NA outside this condition thus gives only the same effective NA as that of the hemispherical-SIL. In addition, as the incident angle θ' increases, the transmittance largely decreases; the part close to $\sin \theta' \sim 1$ has little contribution.

4.2.2 Designing of Optical Data Storage System with SIL

In the application of the SIL devices to the high-density optical data storage, the bottom surface of the devices have to be set at a position close to the storage media surface because of the nature of the evanescent light. Therefore, the protection or cover layers on the recording layer have to be extremely thin and at most on the order of 10 nm. If the refractive indices of the SIL and the disc protection layer are coincident, it is possible to computer-simulate in a combined system, as shown in Fig. 4.16. In this case, a thicker protection layer is available, although better resolution is not obtained because $n \sim 1.5$.

Guerra et al. recently proposed and designed an optical storage disc in which micro-SILs were fabricated on the recording layer (see Fig. 4.17) [47]. In the disc, the high-resolution is obtained across the direction of the grooves. The other advantages are that the lens adjustment and nm-sized space control mechanics are eliminated.

Combination probes with SIL and near-field probe have also been proposed to improve the resolution and throughput. Milster et al. designed an SIL with a small protrusion aperture to increase light throughput [48]. On the other hand, Kurihara et al. designed a combination probe with a micro-lens array of GaP and surface plasmons generated from a grated reflector [49].

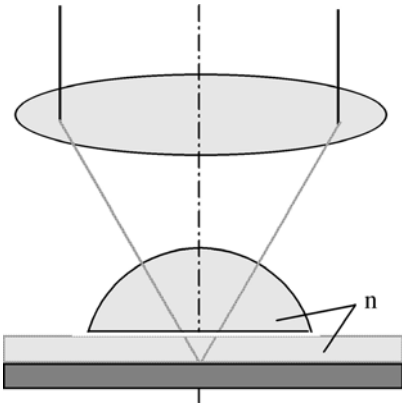

Fig. 4.16. Optical near-field recording system using an SIL slider combined with an optical disc. Hence, the refractive index n of the disc protection layer is coincident with that of the hemispherical lens

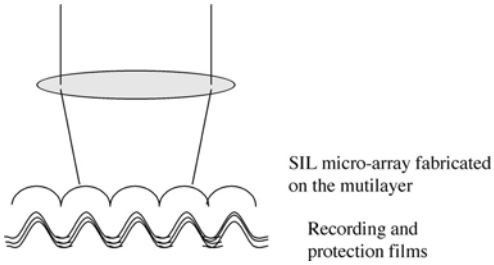

Fig. 4.17. Pre-fabricated SIL micro-array on the optical disc surface by vacuum deposition method by Guerra et al.

4.2.3 Solid Immersion Mirror (SIM)

Realizing the same effect as that of SIL, Lee et al. used a specially designed mirror system (see Fig. 4.18a) [50]. It is named *solid immersion mirror* (SIM). The SIM consists of a specially cut-and-designed high refractive index medium that is covered with a metal coating, except for a center of the bottom surface. In the SIM, an objective lens required in SIL can be eliminated because the lens part is fabricated in the SIM itself. This is the greatest advantage over any other SIL systems. Ueyanagi et al. on the other hand, proposed a SIM with a parabolic mirror (see Fig. 4.18b) [51]. The advantage of this design is to introduce the light beam horizontally, enabling the design of a thinner drive system. In contrast to the difficulties for designing in the SIMs, realizing the same function with the combination of a *plano convex* lens and annular illumination was proposed by Hatano et al. (see Fig. 4.19) [52, 53]. As shown in Fig. 4.19, the metal thin film covers the convex surface and a central area of the flat surface. Then, a small aperture

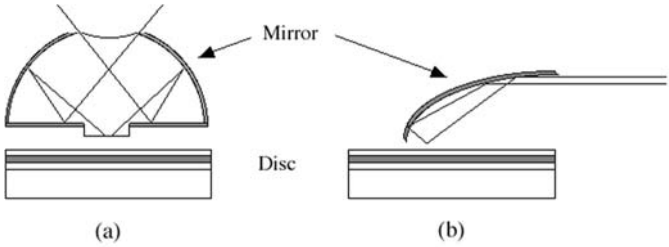

Fig. 4.18. a–b. SIL-related technologies using catadioptric mirror (SIM) (**a**) and hemi-parabolodal SIM (**b**)

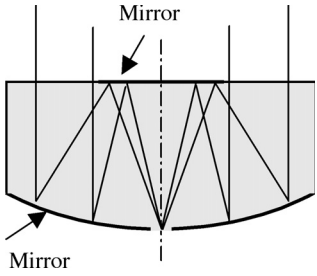

Fig. 4.19. SIM designed by Hatano et al.

is fabricated at the center of the convex mirror. The SIM has more advantage in the manufacturing process, although increasing the side lobe intensity is an issue.

4.2.4 Flying SIL on Optical Disc

Optical recording and readout with the SIL devices have experimentally been carried out by several groups. Terris et al. first succeeded in the flying experiment with a super-SIL device ($n = 1.9$) with $NA{=}_{\text{eff}}$ 2.16 on a stage-scanning microscope, and resolved 350-nm MO marks (Fig. 4.20). Here, they used an optical system with 780-nm wavelength laser beam and $0.6NA$ objective lens [50]. Following this successful work, they also performed the MO mark read-and-write on a rotating MO disc surface at a linear velocity of 1.25 m/s. Mizuno et al. used a lens with NA of 0.7 and a hemispherical lens with $n = 1.26$, and realized NA_{eff} 1.26. They demonstrated read-and-write on an optical phase-change disc, and 200-nm phase-change marks were actually written and read out with a CNR of 49 dB, using a 650-nm wavelength beam at a speed of 8.0 m/s [54]. The flying height was controlled at 50 nm. Here, the tilt margin of the SIL was within $\pm 1^\circ$ and errors from the readout center were within $\pm 100\,\mu$m.

The gap-control systems of the SIL flying devices have also been developed mostly by SONY groups [55, 56]. Ichimura et al. controlled the flying height

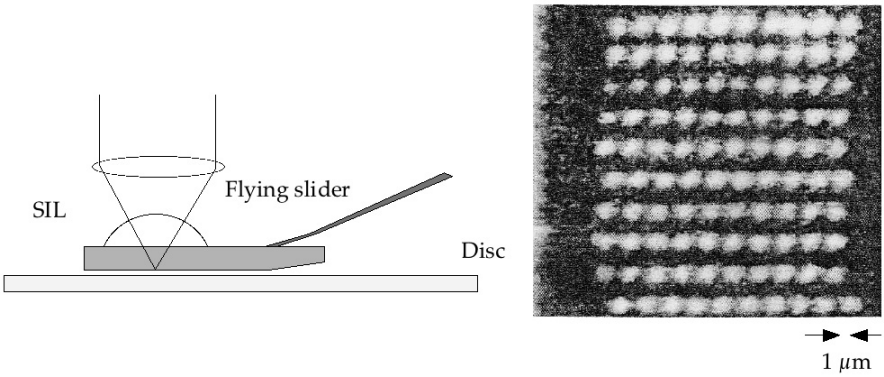

Fig. 4.20. First designed flying SIL head and recorded marks in MO layer. Reprinted by permission of the publisher [48]

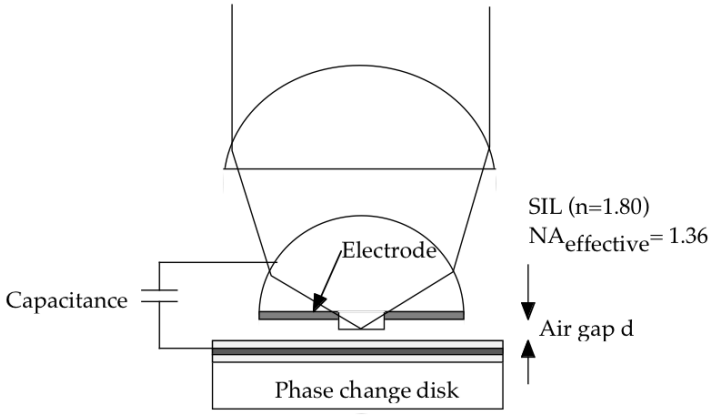

Fig. 4.21. Metal coated SIL system to control the space by the change of capacitance between the SIL and phase-change disc

by using electric capacitance charged between the phase-change film and hemispherical lens bottom that is covered with a metal coating, except for the focused spot [55,56] (see Fig. 4.21). Measuring the capacitance and holding it constant enabled the precise gap control and the feedback of piezo-elements.

Hence, the metal coating was used as an electrode to measure the gap capacitance. If the metal electrode surface is S and the gap distance is D, the relationship with the capacitance C_{gap} is simply

$$C_{\mathrm{gap}} = \varepsilon S/D\,, \tag{4.12}$$

where ε is the permittivity. Using an LC resonance circuit and assuming an external inductance L, the relationship between the frequency and C_{gap} is derived.

$$F = 1/2\pi \left[L(C_{\text{gap}} + C_{\text{f}})\right]^{1/2} \tag{4.13}$$

Thus, by holding C_{gap} at a constant value and the feedback to the lens actuator, the air gap is always fixed at a constant height. They maintained a 40-nm gap height even at a constant linear velocity of 2.5 m/s, which was twice as large as that of a CD-ROM. The applied frequency for the control was 4.44 MHz and a height error less than 2 nm was attained. They succeeded in recording and reading out the phase-change marks with the minimum mark length of 167 nm at the data transfer rate of 15 Mbps, and the corresponding recording density achieved 20 Gbit/in^2 with a *CNR* of 48 dB using a 657-nm laser beam. Following the research, they recently improved the *NA* up to 1.5 by using a super-hemisphere SIL, resulting in a 107-nm mark length readout in combination with a blue laser.

4.3 Super-Resolution Near-Field Structure and Thin Film Technologies

As described in Sects. 5.1 and 5.2, all the NFR systems discussed so far have relatively poor optical throughput and conversion efficiency because of the intrinsic near-field characteristics. The most important issue in NFR results in the non-propagating and exponential intensity reduction characteristics of the near-field; therefore, flying apertures and SILs have been combined and the research transferred from hard disc technology have been carried out since the mid of 1990s. In 1998, a unique idea was proposed for NFR by Tominaga et al., and the technology is called "super-resolution near-field structure (super-RENS)" [57–62]. Super-RENS is not a "lens," but plays a role of something like a lens which generates, confines, and propagates an optical near-field effectively, resulting in recording and readout small marks far beyond the diffraction limit size. Super-RENS technology has provided many attractive and intriguing properties in optical near-field, surface and local plasmons, and its interaction with recording medium since the invention. In this section, the backgrounds of super-RENS and optical dynamic nonlinearities generated in mutilayers are described.

4.3.1 Super-RENS Using an Optical Near-Field Aperture

The principle of super-RENS is attributed to the optical super-resolution (OSR) discussed in Chap. 2. Proposed in the early 1990s, OSR was a technology to improve the optical resolution by generating an optical window in an opaque mask layer [63]. Inserting such an opaque mask between prefabricated pits surface and incoming laser beam, the beam is almost blocked because of its high light absorption. The mask layer first used in OSR was a GeSbTe phase-change film that was a relatively high absorption constant in crystal. However, increasing the beam power, the central region in the beam

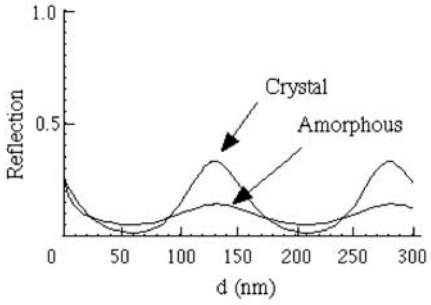

Fig. 4.22. Reflection change through the small aperture generated in the laser spot. Hence, the disc structure is polycarbonate substrate/ZnS-SiO_2 (90 nm)/mask (GeSbTe) (15 nm)/ZnS-SiO_2 (d nm)/recording film (GeSbTe) (15 nm)/ZnS-SiO_2 (20 nm)/Al (100 nm). The simulation was carried out without near-field effect. According to the far-field simulation, the maximum modulations are obtained at around $d = 140$ nm and 280 nm

spot is melted to produce a small part with a low *absorption*, as studied in Chap. 2. If the crystallization speed of the molten part is relatively slower that that of the beam spot, the part is solidified in amorphous with a low absorption. In such case, a narrow line would be drawn and left in the read-out track. If the crystallization speed is fast enough against the beam spot speed, in contrast, the molten part returns to the crystal again, after passing the beam. The size in the active spot thus depends on the disc rotation speed (beam spot speed) and the incident laser power. It means that the active and dynamic aperture size determines the resolution limit. The aperture probably includes much higher spatial frequencies beyond the diffraction limit. However, the OSR was first applied to a ROM disc and the distance between the reflection layer and mask layer was set to about 80 to 160 nm so as to obtain the maximum change in reflectivity. In Fig. 4.22, the reflection change of a rewritable-OSR structure using two GeSbTe layers with a space, d showed that one for the mask and another for the recording layer can be simulated without near-field effect for example. It is clear that there is no solution to obtain a large modulation at around $d \sim 0$.

In the two-slit problem discussed in Chap. 3, the longer distance between the slits rapidly reduces the spatial frequency integration: $\exp[-\mathrm{i}z(k_z^2 - k_x^2)^{1/2}]$. If including higher spatial frequencies in the integration, z has to be smaller than the wavelength. When OSR was first proposed, nobody examined in such a small z region and confirmed the optical near-field effect. The reason is the very small and faint near-field signal compared to the level of the current optical data storage as learned in Chaps. 2 and 3.

In the first OSR, the GeSbTe thin film was adapted as the mask; however, a procedure to crystallize the whole disc from the as-deposited amorphous to crystal was required by using a huge and high power laser beam (this process

Table 4.1. Refractive indices of Sb thin films

Film thickness	Real n	Imaginary k
Sb (7.5 nm) as-deposited	4.51	3.66
Sb (7.5 nm) annealed (200°C)	3.36	5.55
Sb (15.0 nm) as-deposited	3.11	5.66

is called "bulk initialization"). The procedure is very sensitive to the formation of GeSbTe poly-crystalline grains that affect the medium noise (5 to 10 dBm). This noise often damages the overwriting cyclicity of CD-RW and DVD-RW discs. It means that the crystallization condition and grain size mostly depend on the beam power and disc rotation speed. Unfortunately, the as-deposited GeSbTe film produced by dc or rf sputtering method at room temperature is in amorphous state. In addition, as polycarbonate is adapted as a disc substrate of CD and DVD, the substrate should not be irradiated at 120°C, the plastic deformation temperature. On the other hand, there exists the crystallization temperature T_c of $Ge_2Sb_2Te_5$ at around 160 to 180°C. Therefore, without a crystallization-assistant layer such as Sb or Sb_2Te_3 underneath, the GeSbTe film is amorphous. Rather than using GeSbTe, Sb or Sb_2Te_3 is much preferred to the mask layer for the near-field detection because the as-deposited film changes to crystalline state and the grain size is also very small and uniform [64]. In Table 4.1, the refractive indices of a Sb film are listed in amorphous and crystal states, and the light-transmittance change is shown against temperature in Fig. 4.23. In particular, the imaginary index k changes by approximately 2. Thus, the Sb film is one of the preferable candidates for the mask of the OSR-NFR. The second point for NFR is the stability of the readout. In order to protect the Sb mask from oxidation or heat damage due to the laser beam radiation, the mask should be covered with thermally stable dielectric layers, which must be tough enough for the thermal shock. In super-RENS, SiN thin film was selected for the objectives.

The principle of the super-RENS readout is roughly depicted in Fig. 4.24 [55]. Hence, the recording and readout optical head is placed much farther away from the disc surface compared to any other NFRs and the distance is the same as that used in a DVD. The laser beam is focused on the Sb film for example, and the spot size is of course determined by the diffraction limit due to the relationship between λ and the lens NA. By controlling the thermal profile generated due to the Gaussian beam intensity, a very small central part in the spot is activated and optically transits more transparently than in the other region. As the Sb layer and the phase-change recording layer are separated by a thin solid SiN layer (thickness < 50 nm), the optical near-field generated at the active apart can interact with the electromagnetic field weakly-generated on the recording layer. The advantage over any other NFR system is that the readout head-crash with the disc no longer occurs

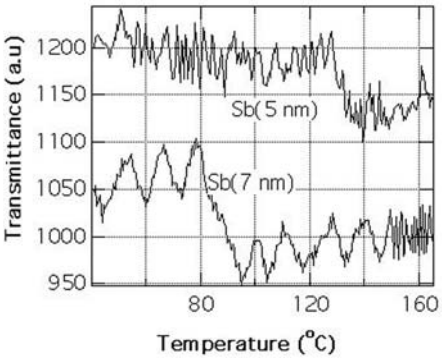

Fig. 4.23. Phase transition of Sb films. The transition temperature from as-deposited amorphous to the crystal state is affected by the film thickness, and no transition temperature is observed at a thickness of more than 10 nm. The films were deposited on a SiN (70 nm) film. The optical interference occurred due to the thermal expansion of the substrate (glass). The phase transition temperature of the 5-nm film is at around 130°C and 85°C for the 7-nm film

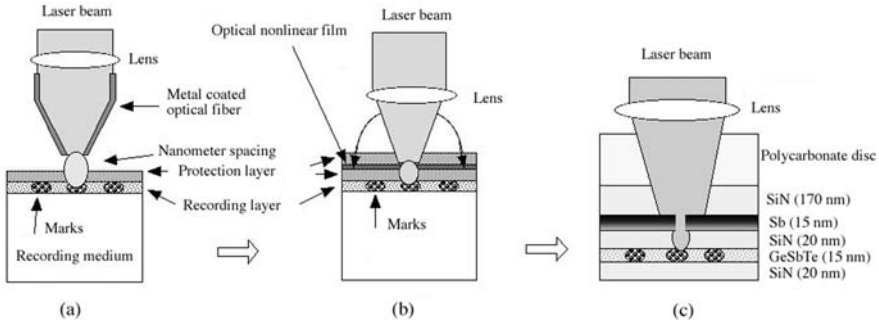

Fig. 4.24. a–c. The principle of super-RENS and its structure. **a** Conventional NFR image using metal-coated fiber probe and recording medium. **b** By expanding the metal coating on the medium, a wide space (mm scale) is preserved. **c** Cross-section of super-RENS disc. Reprinted by permission of the publisher [57]

in the super-RENS system, because the air space is now filled with a solid film, of which the thickness is controlled by a sputtering deposition time. Moreover, due to the structure holding the near-field generation source, the disc can be rotated at a very high-speed nearly equal to that of a DVD (CLV = 6.0 m/s). From this point, the data transfer rate of the super-RENS system was amazingly improved from few tens of bps to more than 20 Mbps! Additionally, the recording area restricted by the scanning area of a piezo-electric unit (100 µm × 100 µm at maximum) was eliminated to all over the 12-cm disc-surface by the invention of the super-RENS.

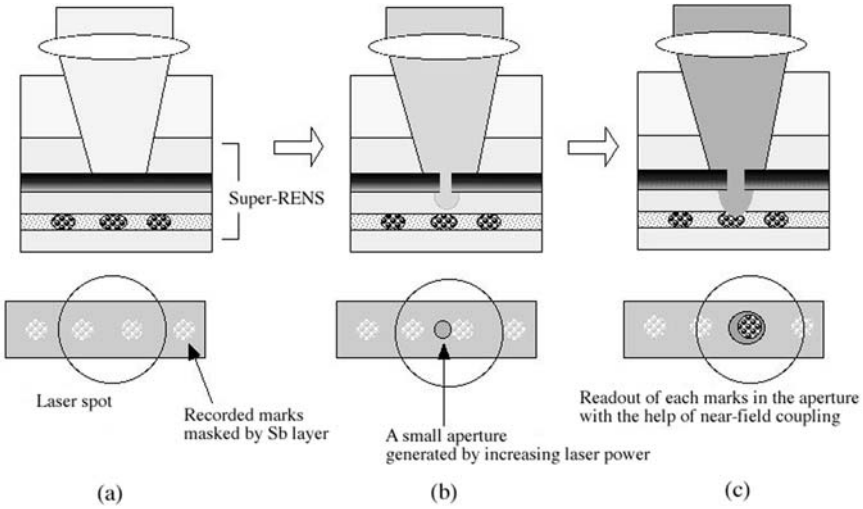

Fig. 4.25. a–c. Super-RENS readout. **a** No mark is readout at a low laser power because there is no aperture formation. **b** As increasing the laser power, a small portion changes the refractive index and an optical aperture is produced. **c** If the power overcomes the threshold power, the optical near-field interacts with the electromagnetic field generated around the marks and the field is scattered to the far-field. As the disc rotates, the Sb crystalline area is continuously provided in the laser spot, and the previously active area becomes inactive to the aperture. It means that the aperture looks like it is running over the disc. The aperture size is controlled by the laser power large and small. It strongly depends on the readout signal intensity. The Super-RENS disc is the only head-crash free FNR system

Recording on the super-RENS disc, on the other hand, is carried out in the same way as that on recordable disc such as a DVD-RAM or DVD-RW. By modulating the laser beam with recording patterns across the track direction, the laser pulse is absorbed into the Sb layer to increase the temperature of the small part (aperture) up to the melting point. The laser beam profile squeezed in the aperture size produces a hot spot, resulting in the phase transition in the recording layer. Due to the high-speed disc rotation, the accumulated heat is soon released and dispersed the beam position backwards and then the aperture closes. As the disc rotates or moves relative to the beam, a fresh aperture is continuously provided and old one is eliminated by the recrystallization of the Sb layer. The motion of the small aperture in the laser spot is depicted in Fig. 4.25, and its FDTD computer-simulation results are shown in Fig. 3.15.

As the laser power increases or decreases, the molten aperture is expanded or squeezed accordingly. Therefore, the readout power should be carefully controlled to hold the signal intensity constant during the disc rotation. As shown in Fig. 3.13, the optical near-field is more accumulated at the aperture

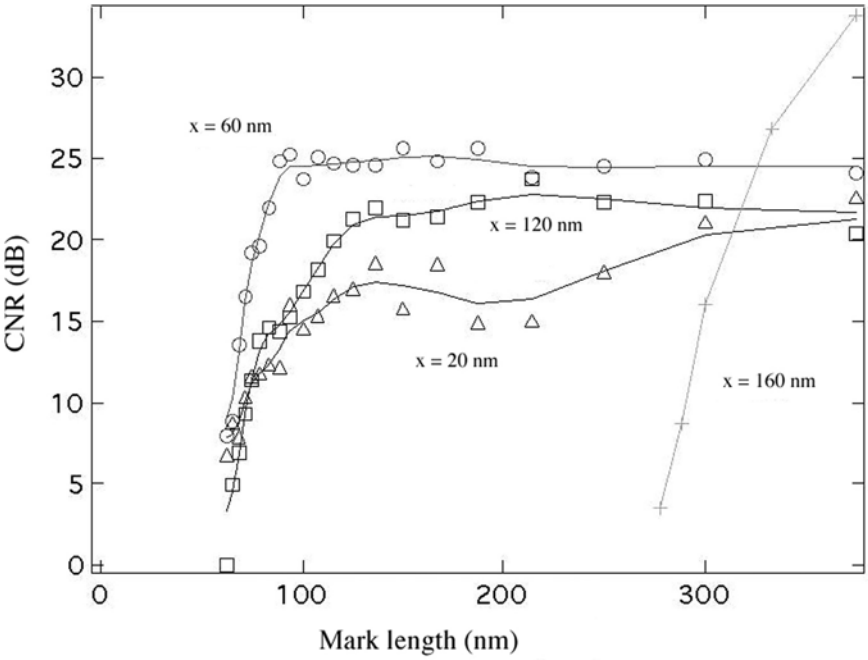

Fig. 4.26. The readout resolution of a super-RENS disc with different intermediate layer thickness x. Hence, the structure is polycarbonate disc/SiN (170 nm)/Sb (15 nm)/SiN (x nm)/GeSbTe (15 nm)/SiN (20 nm). Recording was mostly carried out at a constant linear velocity (CLV) of 3.0 m/s and readout at 6.0 m/s. The *CNR* at around 200-nm mark length decreases with near-field edge effect at x smaller than 40 nm. Hence, the optical system used a wavelength of 635 nm and a lens *NA* of 0.6. Courtesy of Mr. A. Sato

edges, at which the near-field coupling occurs; the signal intensity is weakened as the distance drops to below 40 nm, unexpected in NFR in general. In the actual experiment, as the thickness is reduced to less than 40 nm, the near-field signal intensity decreases. The maximum intensity was obtained at 60 nm (Figs. 4.26 and 4.27).

The experimental result agreed well with the FDTD simulation results (Fig. 4.26). Recording marks and the readout were carried out by a DVD optical disc drive tester (DDU-1000, Pusltec Industry, Corp.). The disc drive was connected to a frequency generator, spectrum analyzer, and oscilloscope. The super-RENS disc was spinning on the tester at a constant linear velocity (CLM) of 6.0 m/s, which was mostly the same speed as that of a DVD-RAM, and a red laser beam (635-nm wavelength) was focused on the super-RENS disc. As we have already studied in Chap. 2, the focus depth of the beam by a lens *NA* of 0.60 is much longer than the total multilayer thickness. Thus, the focus spot size is assumed to be uniform in the layers. Due to the

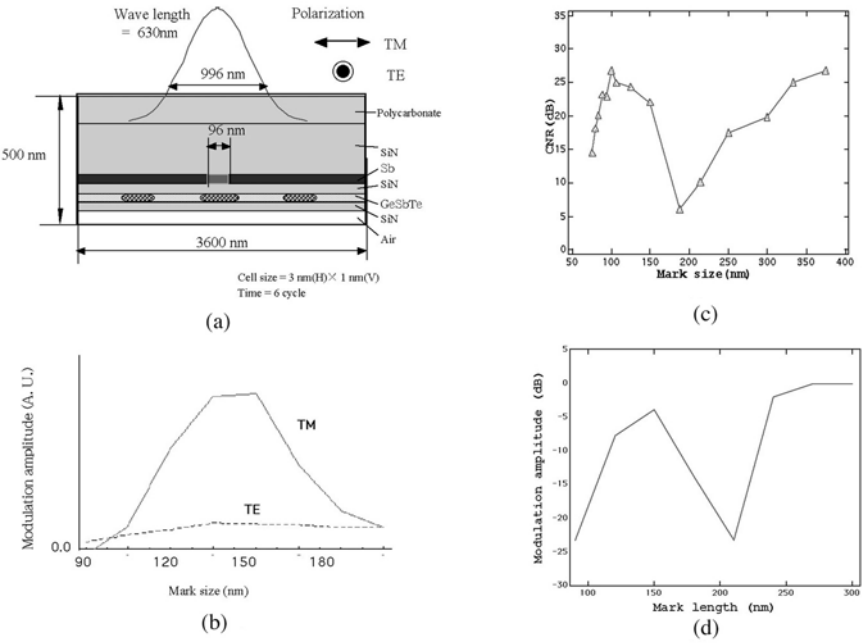

Fig. 4.27. a–d. FDTD computer simulation model of super-RENS and evaluated results. **a** The simulation model. **b** Modulation amplitude of the TM-mode and TE-mode. **c** The experimentally observed mark resolution. **d** The simulated signal amplitude against the mark size. Hence, the intermediate layer thickness is 40 nm. Courtesy of Mr. A. Sato

equation of $(\lambda/2/NA)$, the diffraction limit is estimated to be approximately 540 nm and thus the minimum resolution is the half: 270 nm in the system. As shown in Fig. 4.27, the resolution of the recorded marks in the super-RENS disc is actually in good agreement with the theoretical result, if the readout power is lower than the threshold that generates an optical aperture. As the power is increased up to more than 3.5 mW, however, the resolution is greatly improved by 60 nm, which is a quarter of the resolution. In 2001, a group at Data Storage Institute of Singapore University succeeded in further improving the resolution by 30 nm [65]. The 100-nm mark signals observed by increasing and decreasing the readout power are shown in Fig. 4.28. Nearly about 25 dB was obtained in the system with a wavelength of 635 nm and an NA of 0.6.

So far, we have learned that the Sb thin film holds the very interesting characteristics in NFR. However, the protecting layer also plays a very important role in squeezing the aperture size, thus controlling the resolution [61]. Figure 4.29 shows the resolution limits when replacing the different protection layer. For example, ZnS-SiO_2 is a typical protection layer used

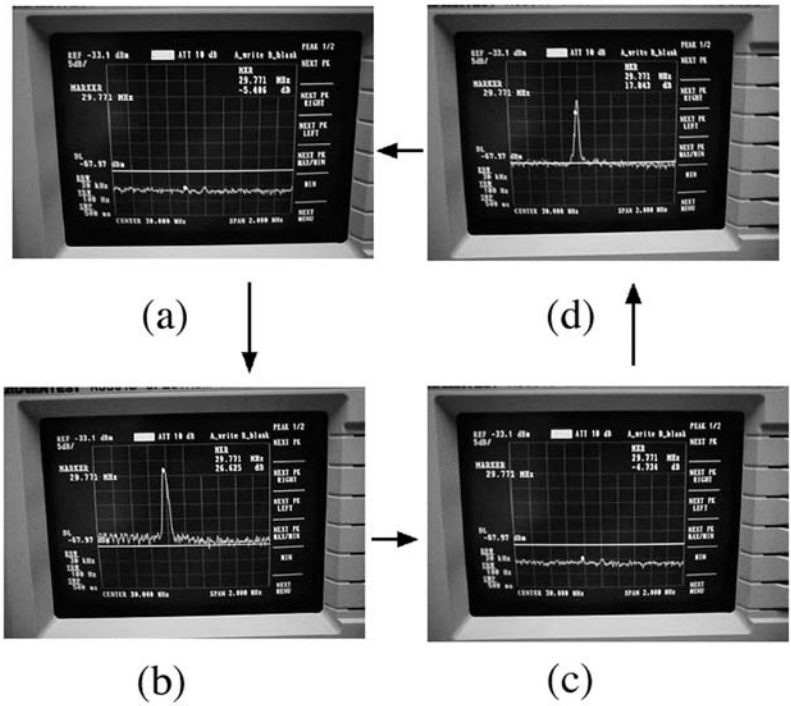

Fig. 4.28. a–c. A 100-nm mark readout by a super-RENS disc. **a** The recorded signal is mostly zero and in the noise at a laser power of 1.0 mW. **b** When the power is increased to 3.5 mW, the recorded signal jumped up to the level around 25 dB on the same track. **c** When the power is returned to 1.0 mW, the signal is eliminated. **d** Once again by increasing the power to 3.5 mW, the signal is recovered on the same readout track. The wavelength and *NA* are 635 nm and 0.6 in the readout system. The disc is rotated at CLV of 6.0 m/s. Reprinted by permission of the publisher [59]

in phase-change recording. This result shows that the combination with the protection layers is also a very important factor for the super-RENS resolution. In thermal static study by 600°C, multilayers of SiN/Sb/SiN and ZnS-SiO_2/Sb/ZnS-SiO_2 on Si wafers showed different melting points (T_m), respectively. In the SiN structure, T_m was not observed by 600°C, while T_m clearly appears in the ZnS-SiO_2structure at about 500°C, despite mostly the same optical properties. One of the resolution effects was believed to be the internal stress forced on the Sb layer affecting the aperture size.

It is actually difficult to estimate internal stresses induced in each layer within the multi-layers. Figure 4.30 shows the stress change of the sandwich structures after each film deposition on Si wafers and annealing at 250°C. The stress was evaluated using the Stony's equation [57]. The stress induced

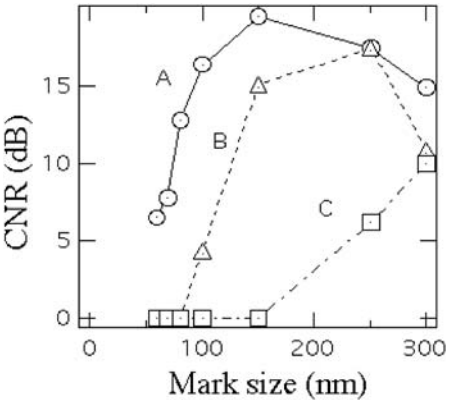

Fig. 4.29. Signal intensities obtained by using different protection layers. (A) denotes SiN, (B) SiO_2, and (C) ZnS-SiO_2. The intermediate layer thickness is the same and fixed at 20 nm. The refractive index of each layer is 2.1, 1.45 and 2.2, respectively. Reprinted by permission of the publisher [59]

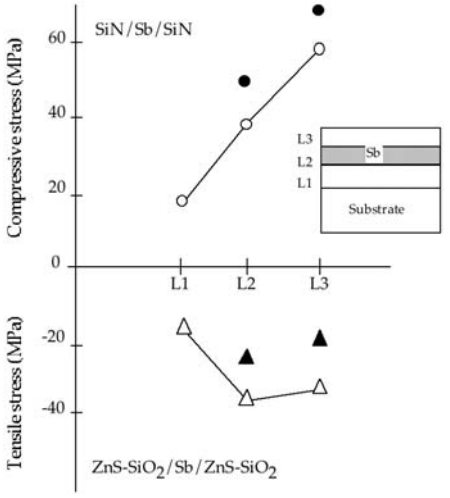

Fig. 4.30. Stress induced by multilayered structures using SiN and ZnS-SiO_2 protection layers. L1, L2, and L3 indicate each surface after film deposition. Open marks represent the as-deposited state and filled marks represent values after annealing at 250°C. Si wafers have a 300-µm thickness, and each layer thickness for L1, L2, and L3 are 170, 15, and 20 nm, respectively. Reprinted by permission of the publisher [59]

after the first Si film deposition was 19.1 MPa (compressive), while it was −16.6 MPa (tensile) for ZnS-SiO_2. As the second and third layers are stacked with SiN, the compressive stress further increased to 38.1 and 58.7 MPa. After the annealing at 250°C, the compressive stresses were more increased by 49.8 and 68.9 MPa. In contrast, the stress was in tensile for ZnS-SiO_2 even after the third film deposition and after the annealing. In readout of the super-RENS discs, the laser power needs to increase the temperature to a threshold value to generating the aperture in the Sb layer. As is well known, the thermal expansion coefficient's in solid and liquid are greatly different and the volume change in liquid is much larger than that in solid. Therefore, as the internal stress of SiN is in compressive, it plays a role in squeezing the aperture formation of the Sb layer, while the tensile stress induced in ZnS-SiO_2 helps to expand the aperture, i.e., it cannot make the size smaller. The effect can probably be explained using the following model and the internal energy balance of the aperture formation in the stack.

$$\Delta G_{\mathrm{tot}} = -\pi r^2 d\Delta G_{\mathrm{v}} + 2\pi r d\gamma + 2\pi r^2 d\gamma_\sigma \tag{4.14}$$

$$\gamma_\sigma = -k\sigma\,. \tag{4.15}$$

Hence, ΔG_{tot} is the total energy, r the radius of the molten portion, d the Sb film thickness, ΔG_{v} the energy change of the phase transition, γ the homogeneous surface energy between molten-solid interface, and finally γ_σ the heterogeneous interface between the molten portion and protection layers. The term γ_σ is only related to the internal stress through a coefficient k. Here, we take compressive stress as positive. The model is depicted in Fig. 4.31.

In the critical condition of the aperture formation, $\Delta G_{\mathrm{tot}}/\Delta r = 0$, and we assume the critical aperture radius r

$$r_{\mathrm{c}} = \gamma/(\Delta G_{\mathrm{v}} + 2\pi\sigma/d)\,. \tag{4.16}$$

As shown in Fig. 4.31, the aperture size reduces by increasing the internal stresses. The model would be helpful to improve the resolution limit. However, as the size decreases, the available photon number becomes smaller – the carrier as the signal becomes lower. As a result, even if the resolution with a smaller aperture reaches less than 30 nm, the *CNR* will not be improved to the level of the conventional CD or DVD (∼50 dB). From the point of view of the FDTD computer simulation (Fig. 4.27), the aperture edges disturb and reduce the signal intensity at a specific mark size (170 nm). The issue will appear in NRF using a bow-tie antenna, as shown in Fig. 4.11. In conclusion, an NFR head with a couple of strong near-field points will not be applicable in future NFR data storage systems if the system or code selects the same recording data sequences or modulation code used in a CD or DVD. This is because there includes a specific mark signal drop due to the near-field interference produced from the front and tail edges of the small aperture. The issue is limited to not only the super-RENS and bow-tie antenna system, but also anyother NFR heads with a flying aperture. Thus, the other tools are required for improving super-RENS properties.

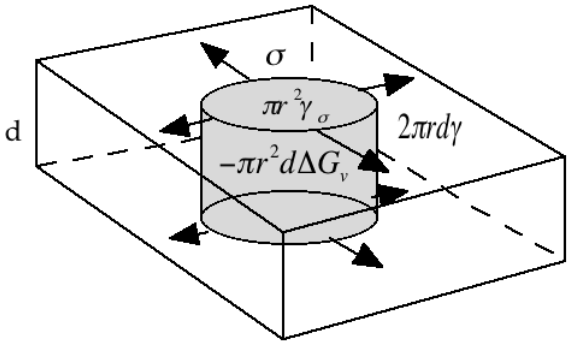

$$\Delta G_{tot} = -\pi r^2 d\Delta G_v + 2\pi r d\gamma + 2\pi r^2 \gamma_\sigma$$
$$\gamma_\sigma = -k\sigma$$

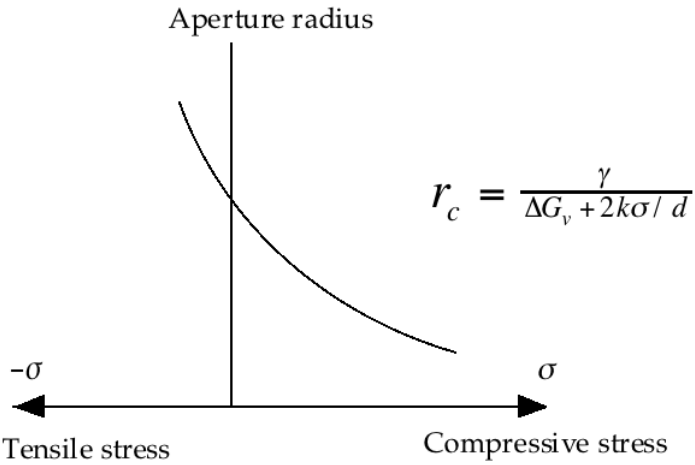

Fig. 4.31. Energy balance in the Sb aperture formation, and the aperture size enforced by the induced stresses by the protection layers. Reprinted by permission of the publisher [59]

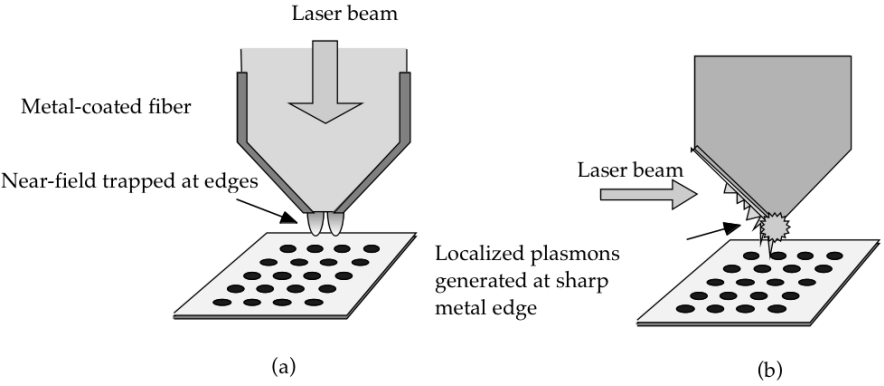

Fig. 4.32. a NSOM with an aperture. **b** NSOM with metallic probe for generating localized surface plasmon polaritons on the wall

4.3.2 Super-RENS Using a Light Scattering Center

In the previous section, we learned that a single light scattering point with strong electromagnetic field is more important and preferable to further enhancing the readout signal in NFR. In near-field microscopy, fortunately, AFM cantilevers covered with a metallic thin film (Ag or Au) have already been utilized and atomically scaled images have been observed with the help of localized surface plasmon polariton, as depicted in Fig. 4.32 [40, 68, 69].

Is it possible to introduce such a single light-scattering center in super-RENS? Once it is possible, the signal carrier level from super-RENS will be further enhanced beyond the practical level ($> 50\,\mathrm{dB}$). To generate a light-scattering center, metallic nanoparticles have to be generated in an active area of super-RENS disc readout. A group at the National Institute of Advanced Industrial Science and Technology (AIST) introduced a silver oxide (AgOx) as the source, instead of the Sb layer. The material AgOx is chemically known to decompose into Ag and oxygen at 160°C in an open system. The material AgOx was first applied to recordable optical disc as CD-R in 1992 to produce a gas bubble pit [70, 71]. The fundamental characteristics of AgOx films are shown in Fig. 4.33. AgOx deposited by rf magnetron sputtering has usually two or three mixture phases of which the formation ratio depends on the gas mixture ratio of oxygen to argon. As the oxygen ratio increases during the film deposition, the refractive index gradually changes from that of an Ag-rich metallic phase to the oxides'. At the oxygen ratio of $0.45 \sim 0.5$ to the total, the imaginary index k has a minimum (0.08). As the ratio further increases, the index is saturated at about 1.0. On the other hand, the real index is saturated at 2.8 with a ratio of more than 0.3. The composition ratio of Ag to oxygen in the film can be confirmed by several techniques, such as Rutherford back-scattering spectroscopy. When the film is thermally heated without a

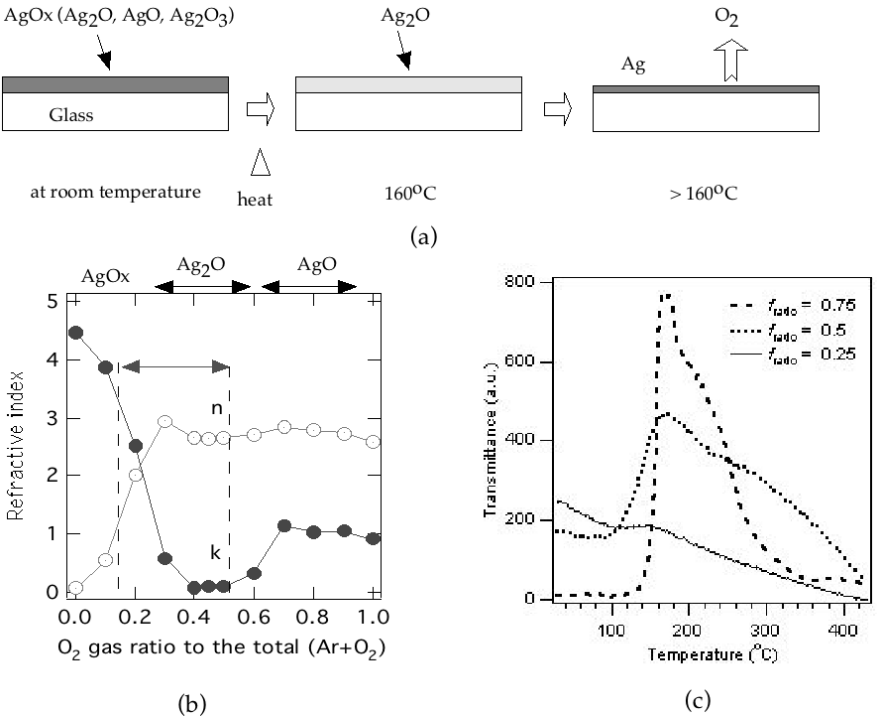

Fig. 4.33. **a** AgOx thin film deposited by rf reactive magnetron sputtering and the thermal decomposition. AgOx films are usually decomposed at 160°C and Ag metallic film is left. **b** The refractive index of AgOx films by changing the gas mixture ratio of oxygen to the total with Ar. The deposition power is 200 W with a 3-inch pure target. **c** The light transmittance of the AgOx films and f means the oxygen gas mixture ratio. At 160°C, the AgOx films change the phases to an Ag-rich state. Even at $f = 0.25$, a small amount of oxygen released will gradually turn the film into a pure silver metal

protection layer, the light-transmittance changes at 160°C (see Fig. 4.33c) and especially the change become larger as increasing the oxygen ratio.

It is not so difficult to imagine that in the AgOx thin film confined in a closed system (protected by dielectric layers from both sides), oxygen released by the decomposition has no space to expand. Figure 4.34 shows the dynamic optical nonlinearity of an AgOx film sandwiched by ZnS-SiO_2 protection layers. As the laser power increases, the beam reflection intensity gradually increases and the transmission intensity in contrast decreases. This means that the reflection in the film is actually changed by the reaction that is mostly reversible in a power range. The effect is strongly related to the oxygen composition in the sputtered film.

The super-resolution effect by the light-scattering center from the AgOx decomposition occurs between the oxygen gas ratio of 0.25 and 1.0 to the

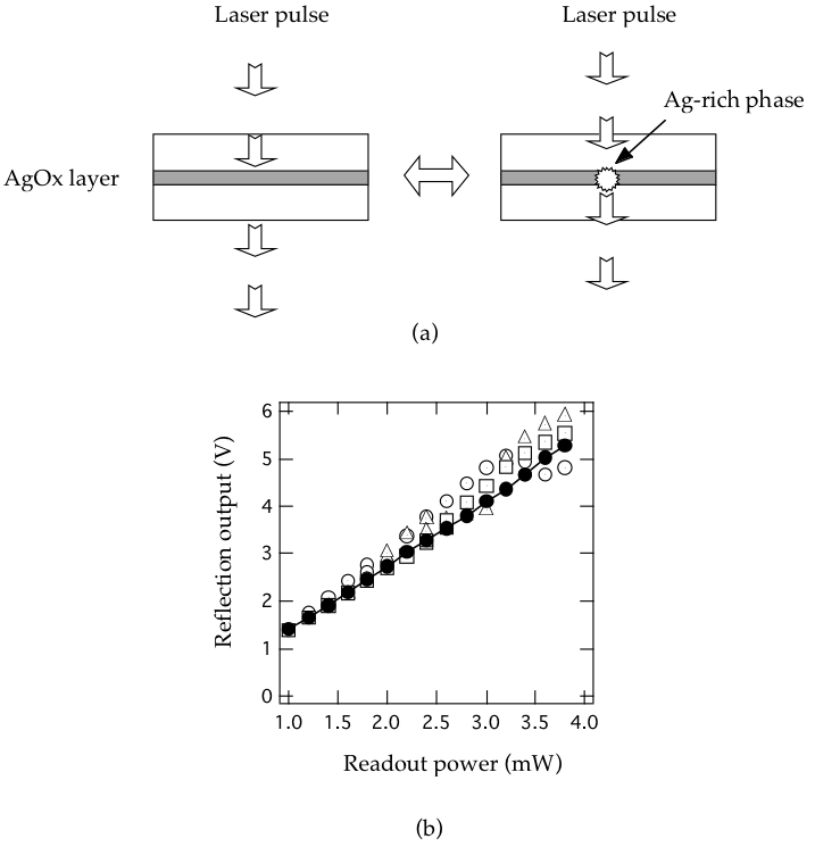

Fig. 4.34. a AgOx reversible reaction images by pulse laser beams. **b** The reflection change from the laser beam focused on the disc in which the structure consists of polycarbonate/ ZnS-SiO_2 (170 nm)/AgOx (15 nm)/ZnS-SiO_2 (20 nm). The disc was rotated and tested at a DVD disc drive tester with a wavelength of 635 nm and an *NA* of 0.60. The rotation speed was varied from 2.0, 4.0, 8.0, and 14.0 m/s (○: 0.6 m/s, △ : 2.0 m/s, □ : 4.0 m/s and ●: 8.0 m/s)

total. In particular, the 0.50 ratio shows the best resolution (Fig. 4.30). Here, it should be noted that the ratio usually depends on a sputtering chamber size and its space between a Ag target and electrode. Also, it depends on the vacuum pumps used. The typical film thickness is 15 nm or less because thicker film may produce a big oxygen bubble by the pressure and heat accompanied with the decomposition by the focused laser beam. The resolution property of the super-RENS disc shows a monotonically decreasing curve, with an approximate resolution of 100 nm on the disc drive tester with 635-nm wavelength and *NA* 0.6 [73].

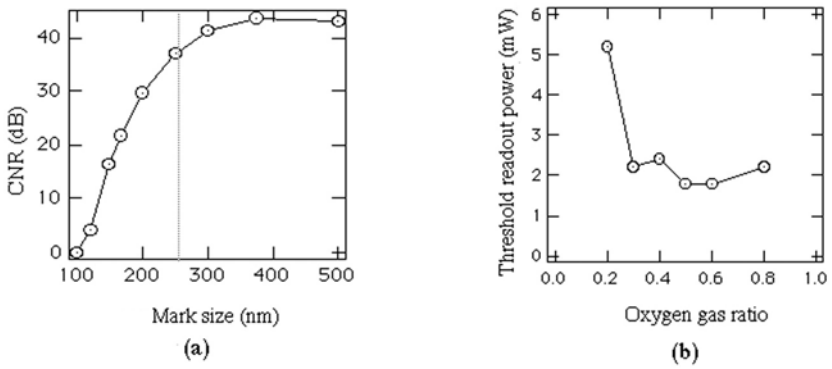

Fig. 4.35. a–b. The super-RENS disc resolution using a AgOx layer (**a**) and the minimum readout power for the super-resolution vs. the oxygen gas mixture ratio (**b**). The disc structure: polycarbonate/ZnS-SiO_2 (170 nm)/AgOx (15 nm)/ ZnS-SiO_2 (40 nm)/GeSbTe (15 nm)/ZnS-SiO_2 (20 nm). The resolution characteristics were estimated by a DDU-1000 optical disc drive tester (635 nm/*NA* 0.6). The disc rotation speed was fixed at 6.0 m/s. The system resolution limit is 270 nm. Reprinted by permission of the publisher [72]

The resolution is inferior to that of the super-RENS disc using an Sb mask layer (60 nm) in the same optical system, but the resolution curve has no special drop at around the 200-nm mark range. This means that the single light-scattering center actually works and is generated.

The switching response of the AgOx layer was estimated by the pump-probe method by Fukaya et al (Fig. 4.31) [74]. As the test specimen, a ZnS-SiO_2 (20 nm)/Ag_2O (15 nm)/ZnS-SiO_2 (20 nm) multilayer was deposited on a glass substrate. The intensity dependence of transmittance and reflectance was monitored by a pump-probe. The pulse cycle of the pump and probe lights was ten pulses a second and a couple of pump and probe pulses are selected by using a mechanical shutter. The pulsed beams are focused by a microscope.

The result observed by the method is shown in Fig. 4.37. Without pump radiation, only a plain rectangular curve was obtained. Hence, the result is the average of the 64 data points. With a pump light, the reflection decreases rapidly in the rising time of the pump and then slowly recovers. The first rapid response time in the reflectance data is approximately 165 ns and the slow response time is 1025 ns. On the other hand, the transmittance response seems much faster than the reflected one.

In comparison with the case in actual disc rotation, the response time estimated in the reflectance measurement seems longer because the rising time corresponds to approximately 6 MHz and 1.0 µm at a constant linear velocity of 6.0 m/s. Because the focused laser spot in the optical system is approximately 530 nm, the light-scattering center always exists outside of the

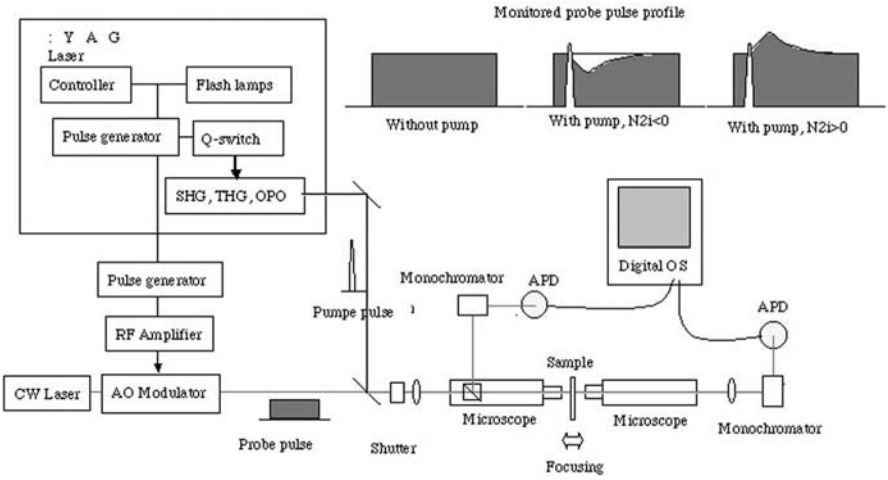

Fig. 4.36. Pump-probe method and the experimental setup. Nd:YAG 10 ns pulse laser is used as the pump light, and a 442 nm He-Cd laser was modulated in microsecond pulses by an acoustic modulator. Courtesy of Dr. T. Fukaya

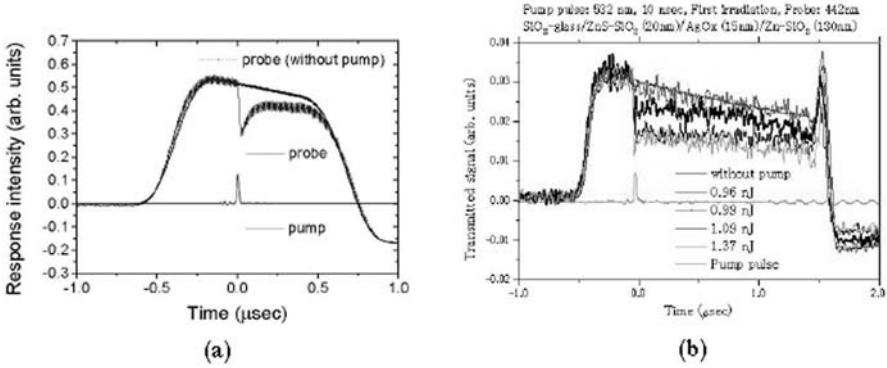

Fig. 4.37. a–b. Reflectance response (**a**) and transmittance response of the AgOx film switching by pump-probe method. Reprinted by permission of the publisher [74]

laser spot. Figure 4.38 shows the super-resolution effect of Sb-super-RENS and AgOx-super-RENS discs against the disc rotation speed. Even at more than 14 m/s, the super-resolution effect is still observed in the AgOx disc. Assuming a scattering size 100 nm, the switching time is evaluated to be approximately less than 10 ns at 14 m/s [72].

However, the recording mechanism and readout mechanism have not been clarified yet. More intensive studies will be required to increase the signal intensity according to the practical application level of the optical data storage.

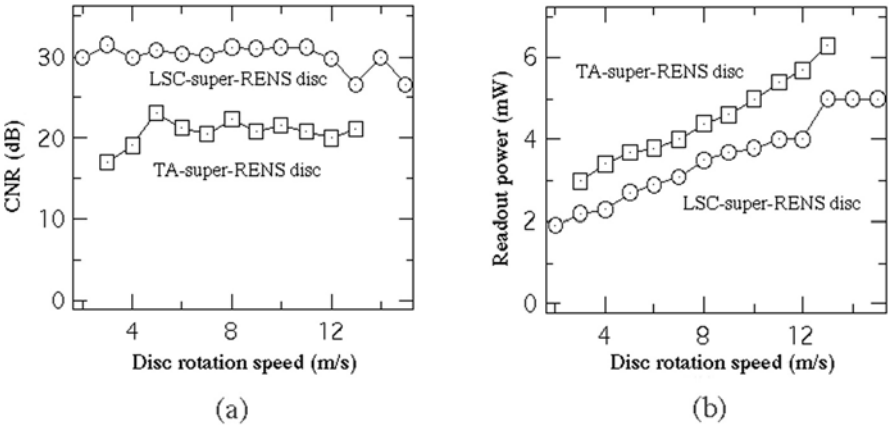

Fig. 4.38. a–b. Super-resolution effect vs. disc rotation speed. **a** The *CNR* change. **b** Minimum readout power. Hence, TA: transmittance aperture (Sb) and LSC: light-scattering center (AgOx) super-RENS. Reprinted by permission of the publisher [72]

4.3.3 Super-RENS with Bubble Formation

In 2002, the third generation super-RENS disc was developed [75]. The characteristics of the new super-RENS disc were found to be very different from the others. The super-resolution mechanism of the light-scattering type has gradually been elucidated through research, however. Before discussing the mechanism, briefly, the present issues of the super-RENS discs of the aperture and light-scattering types should be summarized. First, just like the other NFR heads, thermal damage to the recording film cannot be removed even using the super-RENS disc. It is easy to guess that in the aperture type super-RENS disc, for example, a very hot spot must be required in the laser spot whenever holding the super-resolution effect. It occurs due to the light absorption of the Sb film. As the optical mask layer and the recording layer, which are separated with a thin dielectric layer (SiN or ZnS-SiO_2), are placed nearby (< 50 nm), the heat flows rapidly to the recording film through the thin dielectric layer. Therefore, the recording film is always irradiated to a high temperature ($\sim$500°C). In typical phase-change optical discs, the phase transition temperature of the recording film (GeSbTe or AgInSbTe) exists in the rage from 160°C to 190°C. Even in the short time irradiated at a high temperature, the recorded amorphous marks or crystal ones surrounded by amorphous become unstable, returning to the lowest energy state. It means that the mark shape is getting unclear and finally the mark eliminates as increasing the readout numbers. In the super-RENS disc with the Sb film, the signal intensity rapidly drops at more than 3,000 readouts. In the light-scattering super-RENS disc with the AgOx layer, on the other hand, the readout cyclability is only a little bit better than the disc with Sb. The light-scattering center generates a fireball accompanied with a localized strong

light field. Therefore, although super-RENS is a very attractive method for the super-resolution in less than 100-nm mark size, thermal issue occurred in NFR is not solved. In order to improve or reduce the thermal damage to the recording film in super-RENS, the phase-change materials (GeSbTe or AgInSbTe) would be replaced into other new functional materials holding a higher transition temperature. For the scientists and engineers engaged in the phase-change material research, it will be a very hard work. Secondly, the signal intensity of the recorded marks with a size less than 100 nm is not yet enough high to reproduce the actual eye-pattern of RLL codes. Until recently, it was really thought that both issues are huge obstacles for future super-RENS research.

However, introducing a novel super-RENS disc with platinum oxide (PtOx) layer instead of AgOx eliminated both issues in 2002. This new super-RENS disc is now called "the third generation super-RENS disc." The recording and readout mechanism in the super-RENS disc is absolutely different from that of the former two types. In the third type, the role of the recording in the phase-change layer (for example, AgInSbTe) and the super-resolution readout of the active layer (PtOx) is exchanged. In other words, now, the phase-change layer plays a role as readout, and the PtOx layer does as recording. In recording, a focused laser beam is first absorbed in the phase-change layer because the PtOx layer is very thin and less than 5 nm. Subsequently, the heat is soon transferred to the PtOx layer, inducing the explosion at more than 550°C, resulting in a bubble pit with scattered Pt nanoparticles. Thus, the recording process is completely irreversible. However, the super-RENS disc indicates giant super-resolution and very thermal stability after more than 50,000 readout cycles in comparison with any other super-RENS discs proposed so far, although the phase transition temperature is lower than the PtOx decomposition temperature. Recently, Kim et al. and Kikukawa et al. established and demonstrated the world records of 80-nm *CNR* with 42 dB for the optical system by a wavelength of 635 nm and lens *NA* of 0.60; 50-nm *CNR* with 40 dB for the system by a wavelength of 405 nm and lens *NA* of 0.85 at nearly the same disc rotation speed as that of DVD [76].

So, why does the third generation super-RENS with PtOx show such dramatically improved resolution and stability in high temperature? The important discovery for developing the third generation type had long been hidden in the phase-change material itself. Since the discovery of phase-change materials and the unique switching function as ohvonic memory or optical memory in early 1960s, the research and development had concentrated on the first phase transitions and switching speeds of the materials (mostly chalcogenides). Here, the first phase transition means the phase transition of solid-liquid or liquid-vapor. However, very recently, it has gradually been cleared that GeSbTe and AgInSbTe are ferroelectric [77]. As known well like $BaTiO_3$, ferroelectric materials generally have a Curie temperature as the second phase transition. Here, the second phase transition means the transition

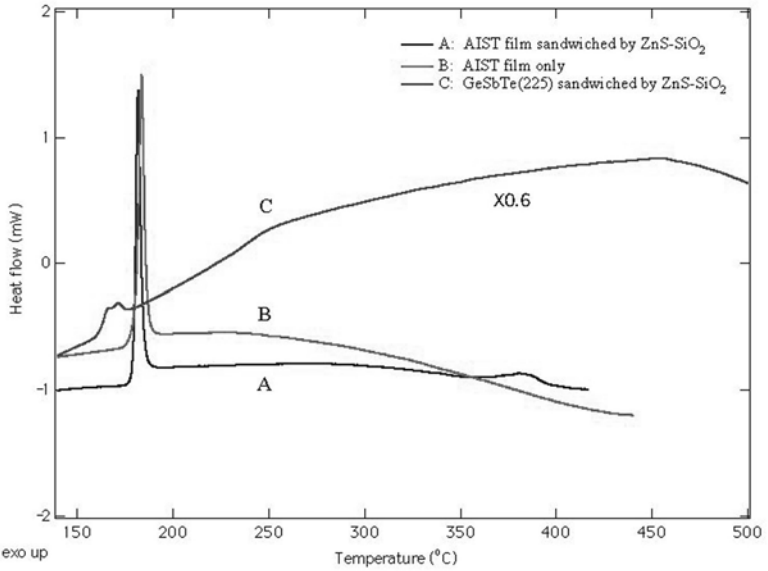

Fig. 4.39. Heat flows of AgInSbTe (A) and GeSbTe (B) films sandwiched by dielectric layers (ZnS-SiO_2), and a bare AgInSbTe film (C)

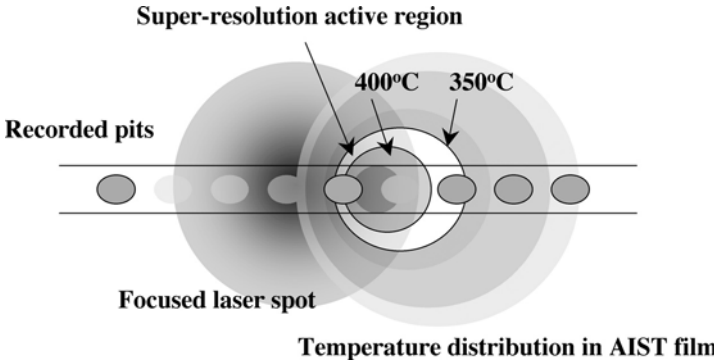

Fig. 4.40. Super-resolution model of PtOx super-RENS readout by a ring aperture formation due to ferroelectric catastrophe

of solid-solid with different structures. In many works published as literatures so far, the second transitions of the phase-change materials had been shown in figures, but the transitions are generally very tiny in comparison with the first transition points. Therefore, nobody had noticed or commented such tiny points appeared in their data curves obtained experimentally. The reason is that while the fist transition accompanies heat flow as latent heat and easy to identify, the second transitions do not, but with a small enthalpy change due to the structural modification to take a lower Gibbs energy: usu-

ally it is very much tiny. Therefore, the heat capacity only bends slightly at the transition. At a glance, although it is thought that the transition may generate a small change in optical constant, it actually induces a huge dielectric variation if the material is ferroelectric because the charge balance in the unit cell is polarized, inducing a huge electronic polarizability. The refractive index is strongly related to the electronic polarizability rather than the accompanied density change. It means that GeSbTe and AgInSbTe may have the great potential for inducing a huge refractive index at the second transition points: Curie temperatures. Figure 4.39 shows heat flow curves of GeSbTe and AgInSbTe thin films sandwiched by ZnS-SiO_2 films to induce tensile stress because the internal stress often stimulates the ferroelectric natures. In GeSbTe, the second transitions appear at 251°C and 457°C accompanied with the first transition peak at 166°C. On the other hand, the second transitions of the AgInSbTe appear at around 350°C and 400°C with the first transition at 182°C. As mentioned, the transition of 182°C is very large in comparison with the second ones. In addition, the film without the ZnS-SiO_2 films does not show the second transition.

According to computer simulations and other experimental results, it was recently reported that there exists a strong correlation between the super-resolution readout power and the second phase transition at 350°C. Based on the ferroelectric transition, one model to explain the PtOx super-RENS readout can be proposed and the mechanism is depicted in Fig. 4.40. As the laser power in the readout, the phase-change film absorbs the light energy and transfer to heat. Then, a temperature profile is generated in the film using the Gaussian beam intensity. Once the temperature overcomes 350°C in AgInSbTe, for example, the ferroelectric catastrophe is induced to diverse the polarizability. This leads to a huge refractive index change and a huge near-field light is generated in the aperture. As the temperature further rises, the active region changes to a ring shape. The ring width may depend on how quickly the atoms can adjust the structure or transit to the higher energy structure. From the experimental results from Kim et al. and Kikukawa et al., the ring width is roughly estimated to be the half of the minimum mark ($30 \sim 40$ nm)!

Since the first invention of super-RENS in 1998, the research and development has gradually spread worldwide to Japan, Korea, Taiwan, Singapore, US, Finland, Netherlands, China, and Switzerland. So far, several interesting super-RENS proposals and experimental studies have been reported. Among them, the third generation super-RENS disc with the PtOx decomposition and ferroelectric super-resolution will become the most promising ultrahigh-density optical storage technology in the future.

5 Role of Surface Plasmons in Optical Disc

As described in Sect. 4.3, the surface and local plasmon interaction between the AgOx and optical phase-change layers provides the interesting characteristics of near-field scattering. So far, almost all studies of NFR have oriented to the fabrications of high-throughput near-field apertures, but paid little attention to the interaction of electromagnetic field generated on small marks and pits. Due to its experimental difficulty, such estimation was not carried out with great accuracy until the super-RENS was invented. In this chapter, we deal with the local and surface plasmon interaction generated on recorded marks smaller than the diffraction limit size in super-high-density optical storage. The properties may provide helpful information for designing pit coordination and recording codes in future NFR.

5.1 Surface Plasmons in Optical Disc and Scattering

Surface plasmon generation on recorded marks in a focused laser-beam spot was first indicated in the super-RENS discs using an AgOx layer, when the signal intensity was further enhanced by closing a second AgOx layer to the phase-change recording layer [78–80]. The latter is based on the assumption that the local plasmons generated in an AgOx layer is the main source of the strong signal intensity from the super-RENS disc. This is something like a bow-tie antenna depicted in Fig. 4.11. In spite of closing the antenna to the recording layer, you can imagine that the recorded mark trains are running through the two tiny metallic light-scattering balls in which electromagnetic field is intensively accumulated, as shown in Fig. 5.1.

Here, generation of optical dipole-dipole coupling with strong light scattering is expected. If the distance between the recording layer and the second AgOx layer is very far, there may be little coupling because such intensive scattering is produced by the combination with the first AgOx layer. As the distance closes, the contribution from the second layer gradually appears and couples with that of the first one. The disc structure and the signal intensities are shown together in Fig. 5.2. The results are very attractive and interesting.

The intensities observed from relatively long marks, which can be read out by the far-field optics, changed little and was mostly constant. In contrast, the intensities of the marks less than the diffraction limit gradually

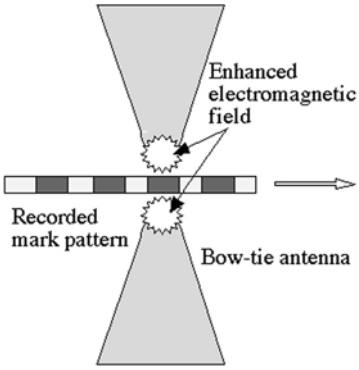

Fig. 5.1. Image of mark running through two light-scattering centers

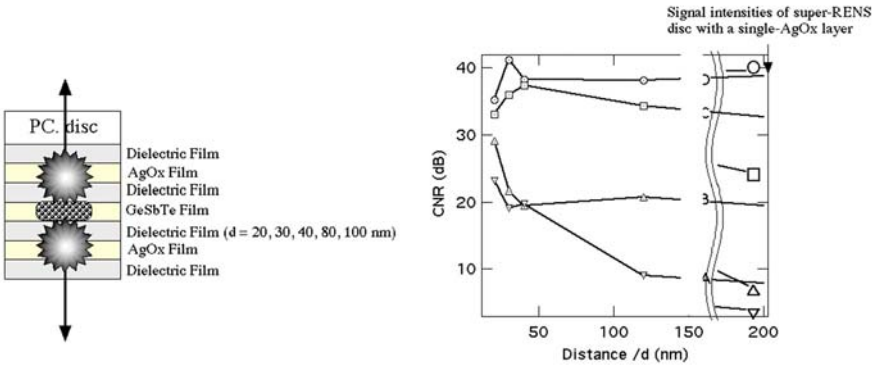

Fig. 5.2. Super-RENS disc with double AgOx layers (**a**) and the experimental result when the intermediate layer thickness d was varied (**b**). A, B, C, and D in **b** indicate the recorded mark sizes and 100, 150, 200 and 400 nm, respectively. The marks showed at the right end of **b** indicates the *CNR* obtained without the second AgOx layer: standard single AgOx super-RENS. Reprinted by permission of the publisher [78]

enhanced with decreasing distance. In addition, the smaller the mark size, the further enhanced the signal intensity. The result ensures it sure that smaller marks beyond the diffraction limit can accumulate a part of the incident electromagnetic energy in the super-RENS disc. The electromagnetic field distribution over small mark trains in the laser spot is estimated in both cases of Ag-AgOx and amorphous-crystal patterns using FDTD computer simulation, and the obtained results are shown in Fig. 3.12. The metal Ag is one of the best materials to generate surface plasmons besides Au. As shown in Fig. 3.12a, the simulation in Ag-AgOx patterns supports the experimental results of the generation of surface plasmons, which mainly concentrate on

the Ag-rectangle edges. The field enhancement was also discussed in the case of metallic aperture flying head and super-RENS disc using an Sb aperture. In the simulation, the model is divided into the Yee's lattice; the edges are always shinning by the plasmons because sharp edges include higher spatial frequencies k in comparison with round parts (see Chap. 3). In the actual experiment, however, the edge is not as sharp, but round and the plasmons may cover with two or three Ag-rectangles in the laser spot. So, how is the cross-section simulated in the case of the amorphous-crystal patterns of the GeSbTe phase-change layer? The amorphous and crystal pattern of the GeSbTe film shows the property similar to that of Ag-AgOx pattern (Fig. 3.12c,d). This is also intuitively understood by the diffraction theory. As discussed in Chap. 3, the surface plasmon is not only generated by attenuated total reflection method (ATR) configuration with a prism and thin metal film, but also induced on a grating pattern (see Fig. 3.1). The diffraction angle θ depends on the grating pitch $2\pi/a$, and as reducing the pitch a, the wave vector along the surface k_x rapidly increases. Finally, $k_z = (k^2 - k_x^2)^{1/2}$ becomes imaginary, if k_x overcomes a threshold; a part of the incident light energy is absorbed in the grating as surface plasmons. This is confirmed by measurement of the reflection and transmission energies to the incident one. The simulation results indicate that the GeSbTe phase-change pattern works as an optical grating. Here, we have also to consider that the laser beam is not normal to the pattern surface because the laser beam is focused by a high lens NA of 0.6 or 0.65 in DVD, etc. Therefore, the generating surface plasmons on the pattern may be more effective and easier. In comparison with the simulation results, the above experimental results of the super-RENS discs using the double-AgOx layers strongly support that the recorded small marks beyond the diffraction limit generate surface plasmons over several marks and accumulate the incident-light energy. The light diffraction by the recorded small marks in the super-RENS disc was experimentally confirmed by the following system shown in Fig. 5.3 [79]. This experimental setup was designed to confirm the diffraction by focusing and crossing two laser beams coincidentally on a mark-recorded small area (less than 1 μm), while rotating the super-RENS disc at a high speed. A light-scattering super-RENS disc of an AgOx layer was inserted between two laser pickup heads. One of the pickup heads consists of a 405-nm wavelength laser (blue) beam and of a 635-nm wavelength (red) laser beam. Both laser beams are focused on the multilayer fabricated on a surface of the disc by the lens with NAs of 0.65 for 405 nm and 0.6 for 635 nm, respectively. The foci and positions on the disc was controlled by the same feedback system as that of a CD or DVD drive, which was already explained in Chap. 2. A light-scattering center was generated by the power control of the red beam and the blue laser was slightly power-modulated at a high frequency (around 15 MHz). Hence, the blue power was small enough not to affect the light-scattering center generation by the red laser.

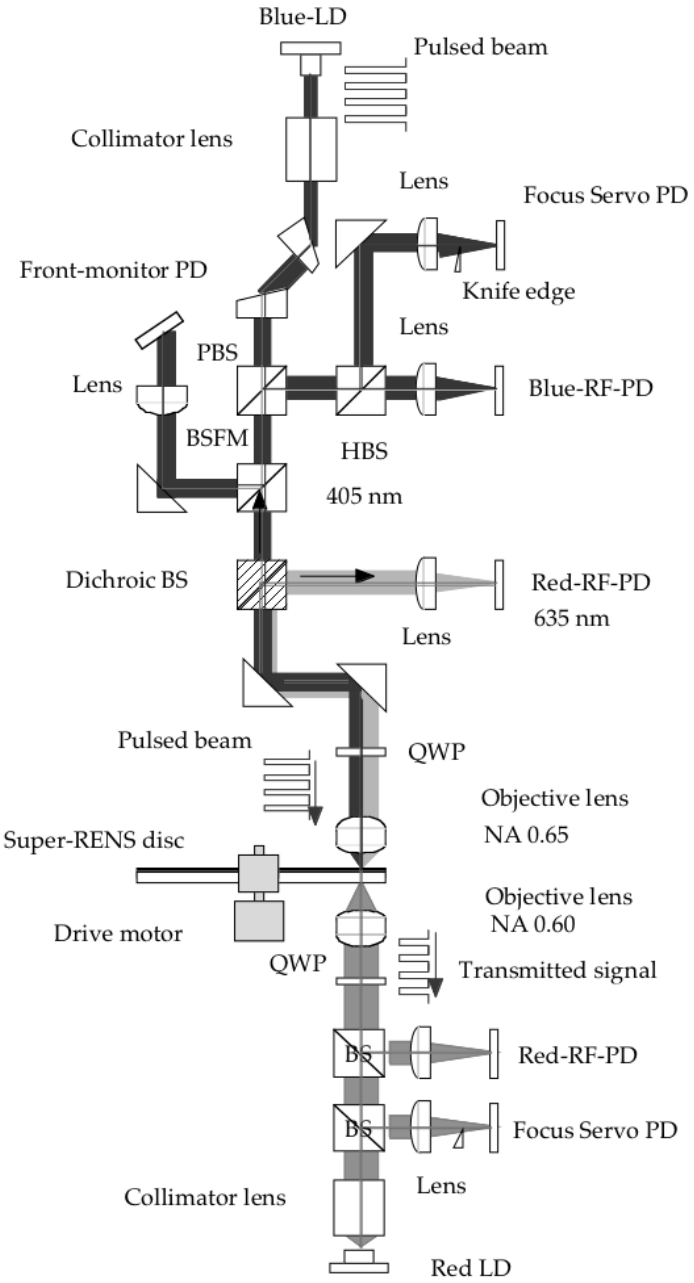

Fig. 5.3. Experimental setup to confirm the surface plasmon generation. Red and blue laser pickup units with a photodetector sandwich the rotating super-RENS disc. The blue laser is slightly power-moduated, while the red laser is continuously varied by 4.0 mW. The transmitted blue beam through the disc was monitored by the photodetector in the red pickup unit

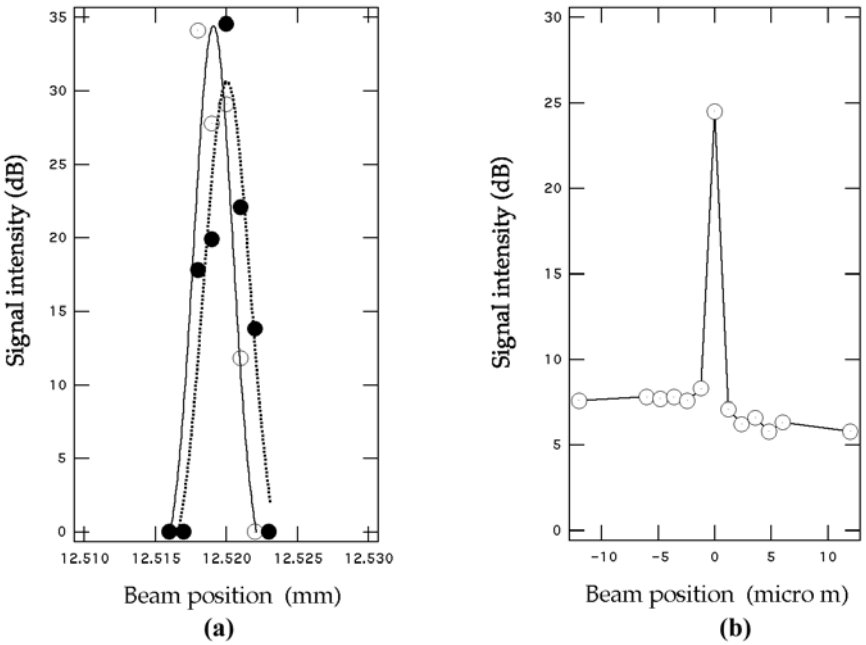

Fig. 5.4. a–b. The blue laser signal intensity change against the red laser position shift. Hence, no mark pattern was recorded. **a** The red laser was shifted along the groove. **b** The red laser was shifted across the groove. Hence, the blue laser was power-moduated at 14.8 MHz with the power between 0.5 and 0.7 mW. Open marks show the intensity at the red laser power of 1.0 mW and black marks at 2.0 mW, thus generating the scattering center

The diffraction characteristics of the transmitted blue laser beam as a result of changing the recorded mark pattern and pitches were monitored. As already studied in Chap. 3, the diffraction angle of the incident light becomes steeper as the pitches reduce in size. Hence, it should be noted once again that the red laser is not used to record marks or pattern, but to generate a light-scattering center in the AgOx layer. In the experiment, the signals detected by the red laser pickup includes two different wavelength lights: the reflected red laser beam from the recorded mark pattern and the transmitted and modulated blue beam which is power-modulated by a tuned frequency. That is, after recording small mark patterns, the red laser pickup reproduces both signals. However, if the mark size is smaller than the resolution limit size, the signal from the red reflection will be eliminated with less than the threshold power of the super-RENS. Then, you will be able to observe the different diffraction patterns by changing the size and pitch of the recorded mark pattern. As you move the red laser position to the blue laser spot, the high and low diffracted intensity pattern will be observed at around the blue laser spot. The experimental results are shown in Figs. 5.4 and 5.5 [80].

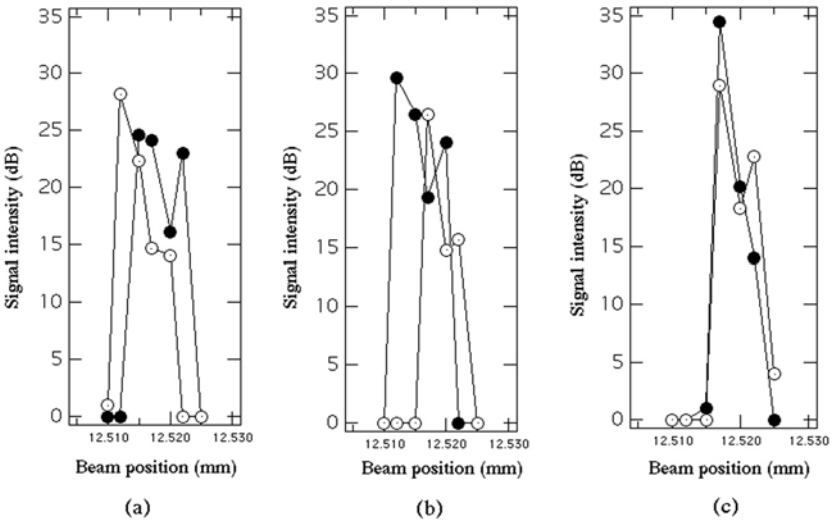

Fig. 5.5. a–c. The blue laser intensity changes after recording marks. **a** Mark pattern recorded with 300 nm, 200 nm **b** and 150 nm **c**. The marks were recorded by the red laser at 7.0 mW, and the readout conditions were the same as those in Fig. 5.4

Without recorded marks (Fig. 5.4), the diffracted pattern has a single peak along the tangential direction. It is absolutely true because there was no diffraction source on the track. On the other hand, the diffraction pattern after recording the longer marks (Fig. 5.5) appeared to split into two beams in the range of approximately 10 µm, and high orders of the diffracted beams are clearly detected. The intensity peak positions are all observed at the edge of the detectable area. The lens is approximately separated by 3 mm from the disc surface. As a result, $\pm\theta < \sin^{-1} NA$ is only admitted for the detection. Therefore, the higher orders of the diffracted beams beyond θ are cut off by the lens. As the mark pattern pitch a decreases by which the red detector is not able to detect, the two peaks seem to merge into one peak and the intensity of the center of the detectable region becomes larger. However, the blue laser pickup can still detect the recorded marks because the mark size is in the resolution limit of the blue system while beyond the resolution limit for the red detector. From the results, the diffracted peaks of the blue laser passing through the small mark pattern are not merged, but widely diffracted and not detected by the red detector. The result strongly indicates that the recorded small marks in the super-RENS disc play a role of accumulating the incident light energy as surface plasmons. Of course, the incident light of the red laser beam may be accumulated as the surface plasmons as well as the blue beam. This is the strong evidence that the surface plasmons are generated in the disc.

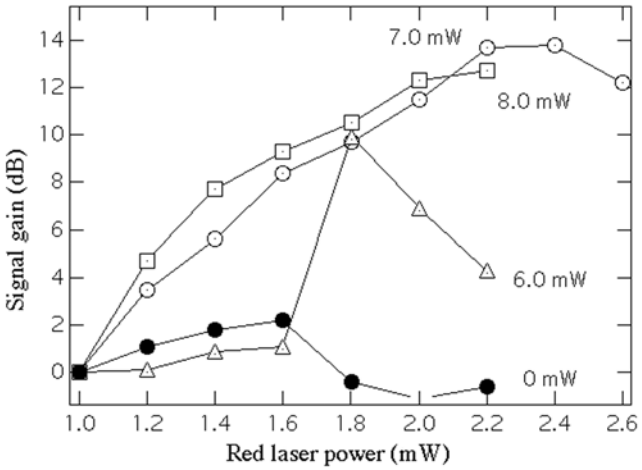

Fig. 5.6. Signal gains against the red laser power. The 200-nm mark pattern was first recorded in each track by several recording powers: 6.0, 7.0 and 8.0 mW. The blue laser power was modulated between 0.5 mW and 0.7 mW at a frequency of 15.3 MHz

What happens next when the red laser beam power is increased and a light-scattering center is generated in the proximity of the surface plasmon field on the recorded mark pattern? Figure 5.6 gives the results and answer. After recording 200-nm sized mark patterns on several tracks with different powers, the red laser power was gradually increased. On the track recorded by 0 mW there were no marks, the intensity change of the transmitted blue beam was small against the red laser power because there was no surface plasmon generation. At the recording power of 6.0 mW, the intensity increases suddenly at the power of 1.7 mW. Hence, the power is the minimum for mark recording. At the recording power of more than 7.0 mW, the transmitted blue intensity increased and decreased reversibly against the red laser power [81, 82].

Figure 5.7, on the other hand, shows the results when the mark size was changed and the recording power was fixed at 7.0 mW. As the mark size increased, the amplification was clearly increased. From the experiments, the local plasmon generation in the proximity of the surface plasmons in the super-RENS disc has the potential of releasing and scattering the accumulated surface plasmons in the disc. Through the analytical works, the mechanism of the light-scattering super-RENS disc is believed to be the coupling of the surface plasmons generated on the recording marks and the local plasmons in the AgOx layer. As a result, the electromagnetic field is released and scattered as far-field signals, as shown in Fig. 5.8. In the light-scattering super-RENS disc, the local plasmons in the red laser spot play an important role in enhancing the blue laser signal as well. This is confirmed by using the

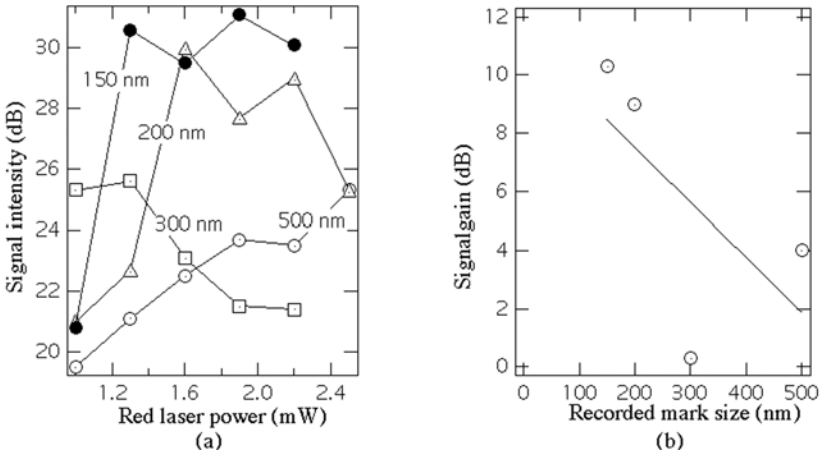

Fig. 5.7. a–b. The signal gains change by recording mark sizes. **a** The relationship between the signal gain and red laser power. **b** The gain against recorded mark size. The signal gains depend on the mark size and is controlled by the red laser power reversibly

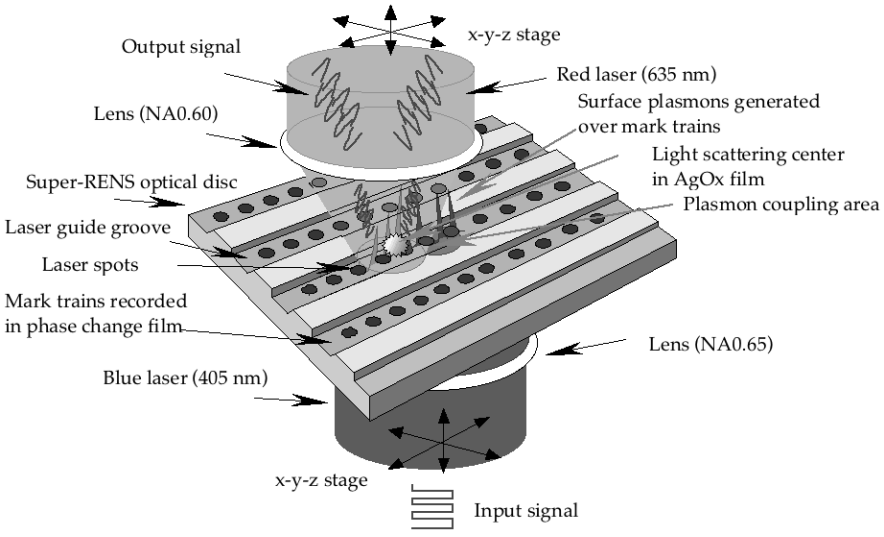

Fig. 5.8. Images of surface and local plasmon coupling in the super-RENS disc. This would work like a photonic amplifier or transistor (local plasmon photonic transistor)

combination of two AgOx layers, instead of one GeSbTe recording layer [82]. The same experimental setup used in Fig. 5.3 is applicable to the local-local plasmon scattering. The disc structure is depicted in Fig. 5.9.

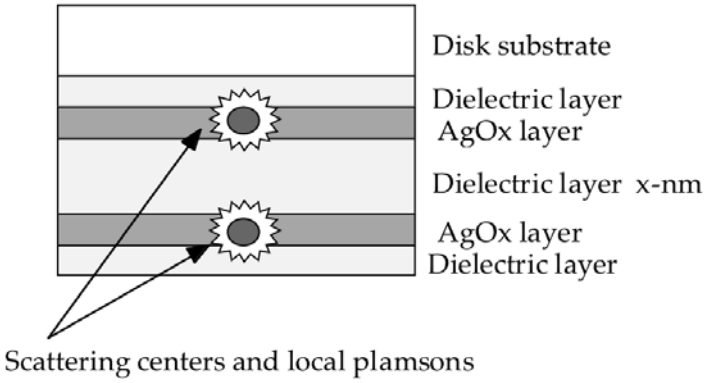

Fig. 5.9. The disc structure to estimate the local-local plasmons coupling by using double AgOx layers. Hence, the recording layer is removed

5.2 Localized Plasmon Scattering with a Coupled Scattering Center

In our studies, the distance between the intermediate layer thickness between the AgOx layers was varied and the transmitted blue laser intensity was monitored by the red laser pickup unit. Here, in order to elucidate the local-local plasmon coupling effect, recording marks are no longer needed (see Fig. 5.9).

The blue laser was slightly power-modulated to avoid affecting the generation of the light-scattering centers in the AgOx layers. The results obtained are also very attractive. Two different curves were observed at 2.3 mW and 3.8 mW against the red laser readout power, as shown in Fig 5.10a. At 2.5 mW, the intensity rapidly decreases against the intermediate layer thickness by $1/5\,\lambda$ and then it is saturated. At 3.8 mW, in contrast, the tendency is similar to the curve at 2.5 mW, but it has a hill at around $1/4\ \lambda$, where an optical cavity is probably generated between the two AgOx layers. The FDTD computer simulation of this model supports the experimental results, as shown in Fig. 5.10b. Hence, E_x is the electromagnetic field in plane polarization and E_z is the evanescent field. The result obtained at 2.5 mW is consistent with the E_z characteristics in the simulation. Thus, the signal enhancement by the scattering at 2.5 mW results in the evanescent light coupling. On the other hand, the result at 3.8 mW is similar to the curve of E_x, which is the propagating far-field. It therefore suggests that the hill at $1/4\ \lambda$ generates the optical cavity between two light-scattering centers. The actual signal photos observed in an oscilloscope and a spectrum analyzer are shown in Fig. 5.11 at different red laser powers. The coupling gain is estimated to be approximately 5 to 10 dB. On the other hand, as described in the section on advanced super-RENS discs, the signal level is more than 40 dB even at 200-nm mark patterns. From the above experiments, the contribution of the

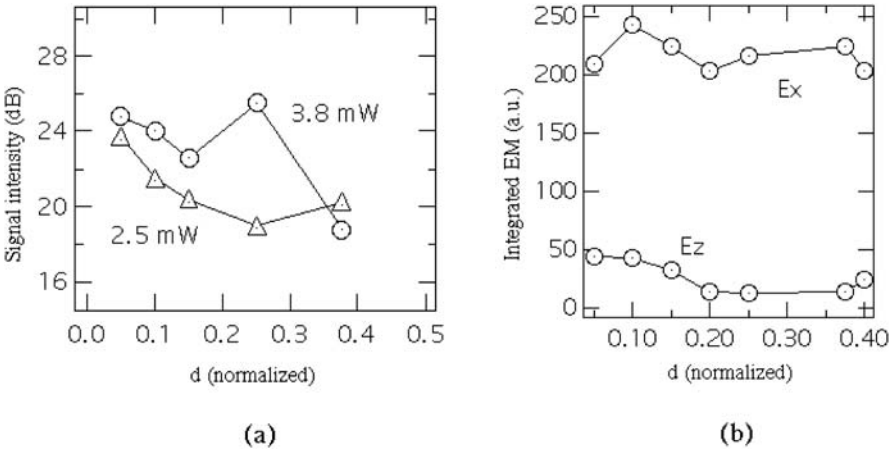

Fig. 5.10. **a** Experimentally observed singal intensity change by different incident powers 2.5 mW and 3.8 mW. **b** Integrated electromagnetic field intensities of evanescent (E_z) and propagated field (E_x) in computer simulation

localized plasmon coupling using two Ag light-scattering centers is not big enough to push up the signal intensity more than 40 dB, and just only about 10 dB at most. In contrast, as shown in Fig. 5.6, the contribution of the surface plasmons seems a little bit larger, but does not exceed 20 dB. Therefore, a huge refractive index change is really required to increase the signal intensity by inducing special functions of materials, such as ferroelectric catastrophe used in PtOx super-RENS discs.

5.3 Localized Plasmons and Super-Resolution with Metallic Nanoparticles

As discussed so far, it has gradually been understood experimentally that the electromagnetic field enhancement of surface plasmons and localized surface plasmons generated in optical discs are not so enough to increase the signal intensity towards the same level as that of the commercialized ones. Fortunately, the results were only the values from the experiments using a couple of light-scattering centers or the scattering involving a single scattering center and several small marks. As increasing the numbers of the scattering centers and activating the coupling points in nano-scale region, further strong electromagnetic field will be released and enhance signals from small marks. In order to realize this objective, a thin film structure composed of a large amount of metallic nanoparticles is required. Tominaga et al. recently demonstrated optical nonlinear response and super-resolution effect with nano-structured thin film composed of Ag metallic nanoparticles [82]

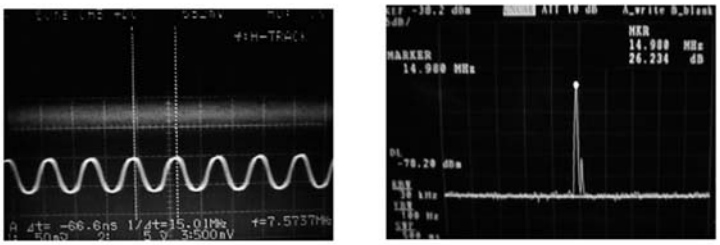

(a) $P^{red}_{readout} = 1.5\,mW$

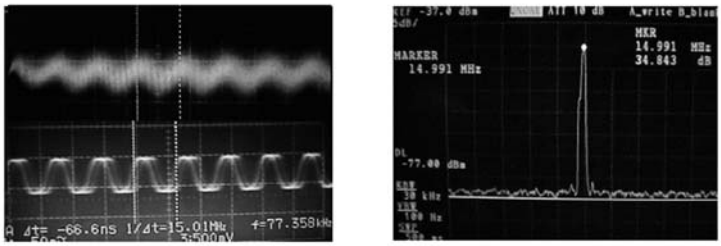

(b) $P^{red}_{readout} = 3.5\,mW$

Fig. 5.11. Optical switching effect of the super-RENS disc with two light-scattering centers. Hence, the intermediate layer thickness is 20 nm, and incident blue (405 nm) laser power is modulated between 4.5 mW and 1.0 mW at 15 MHz. The transmitted signal from the disc at the red laser power of 3.5 mW is 34.8 dB, and 26.2 dB at 1.5 mW. Left pictures of **a** and **b** show the transmitted signals (15 MHz) (*top*) and incident signals (*bottom*). Right pictures shows the transmitted signals detected by spectrum analyzer

The fabrication method of Ag nanoparticles was a spin-off technology from super-RENS disc research. As studied in Chap. 4, it depends on the experimental fact the AgOx film decomposes at more than 160°C. This means that the bonding energy between Ag and oxygen is not so strong in comparison with the bonding between hydrogen and oxygen. Therefore, oxygen may be easily removed by hydrogen from AgOx, resulting in Ag metal. After depositing a AgOx film on a glass or polycarbonate disc substrate, the film is deoxidized in a reactive ion etching chamber by introducing gas mixture of H_2 and O_2, with a small amount of CF_4 for the seeding. Advantage over any other fabrications reported so far is that this method can be applicable to almost all materials, on which a AgOx film is deposited. The Ag nanoparticles fabricated by the method is shown in Fig. 5.12.

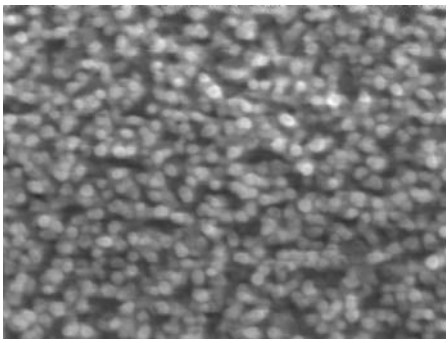

Fig. 5.12. SEM image Ag nanoparticles (size of each nanoparticel is 20nm) fabricated by oxygen reduction from AgOx film

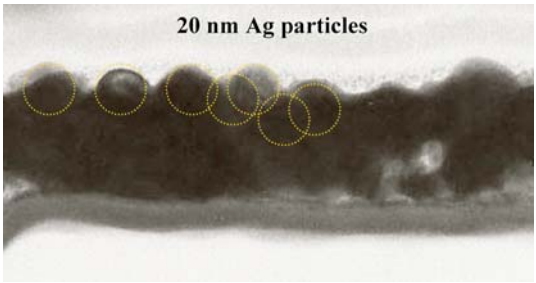

Fig. 5.13. Cross section of Ag nanoparticles formed on a polycarbonate disc substrate. A ZnS-SiO_2 dielectric thin layer (10 nm) was covered with the plastic substrate (TEM image)

Each size of the Ag nanoparticles is approximately 20 nm and very uniform. The nanoparticles formed on a polycarbonate disc substrate with grooves and lands is shown in Fig. 5.13, which was taken by transmission electron microscope (TEM).

The size and shape can be changed from particle-like to wire-like structures in the redox condition. As the amount of Ag in the film increase, the structure shows wire-like formation, while it transits to particle-like with decreasing Ag.

Controlling Ag composition only by sputtering condition may be hard sometimes. In such a case, a thin film of Ag ($\sim$50 nm) should be deposited before hand. During the AgOx deposition, then, the two layers inter-diffuse to form an Ag-rich AgOx film. From these treatments, a variety of Ag nanostructures can be fabricated on a whole surface of a 12-cm optical disc substrate, as shown in Fig. 5.14. The optical nonlinear characteristics, especially the super-resolution effect after laser recording are very interesting. The structural deformation with pit patterns by laser radiation is shown in Fig. 5.15. Hence, no phase-change recording layer was deposited on the structure. In turn, the

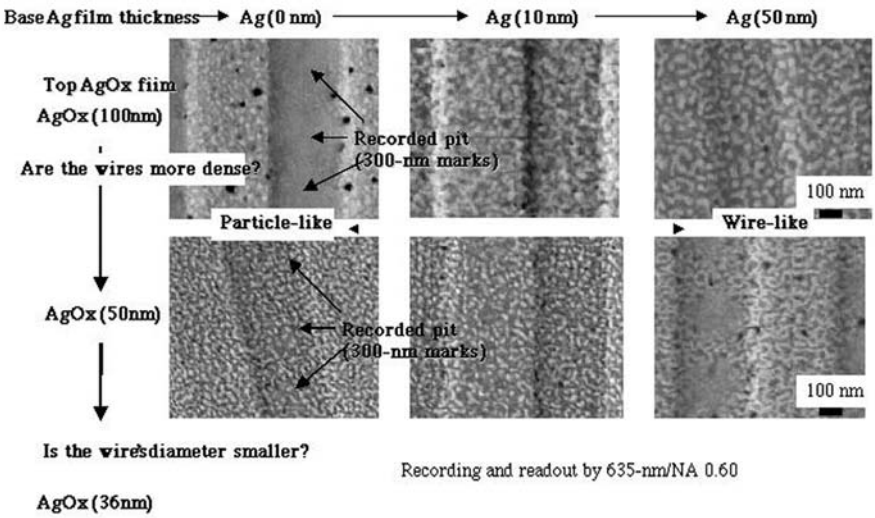

Fig. 5.14. Ag nanostructures fabricated under several different conditions. As the base Ag film thickness increases, the structure transforms to nanowires

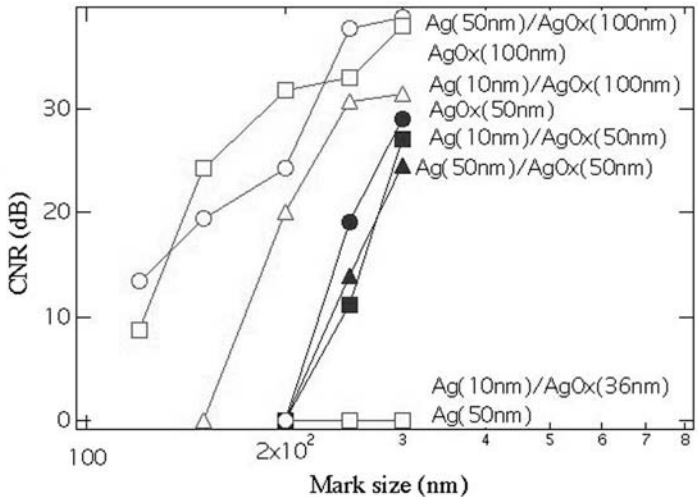

Fig. 5.15. Super-resolution effect depending on Ag nanostructures with the same optical discs in Fig. 5.14. The recording and readout was done by a DVD disc drive tester with a wavelength of 635 nm and lens NA of 0.6. The theoretical resolution limit is 270 nm.

discs were composed of only two layers: ZnS-SiO_2 protection layer and Ag nanostructure layer. It is interesting, but plausible, that a single Ag layer did not show any super-resolution effect because there was no solution to generate surface plasmons between the protection layer and the Ag layer. With a thin Ag nanostructure (curve of Ag(10 nm)/AgOx(36 nm) in Fig. 5.15), the super-resolution effect was not allowed. As the nanostructural thickness increased above 50 nm, the super-resolution effect was induced. From the figure, the super-resolution effect probably depends on the nanostructural thickness.

It should be noted in general that a penetrating thickness of the surface plasmons in the Ag layer is at most 50 nm. However, in Fig. 5.15, the effect has the clear thickness dependency of the nanostructure. Therefore, the effect is probably attributed by the surface plasmons locally generated between the nanoparticles or nanowires : localized surface plasmons. Applying and combining the localized surface plasmons in this method to the third generation super-RENS disc will be able to further enhance and amplify small pit signals of less than 10 or 20 nm in size by the help of the plasmons.

6 Epilogue

In this book, we have introduced optical recording from the development of CD to the advanced future high-density systems, where localized photons will be applicable to overcome the diffraction limit. It has already been 20 years since the first invention of optical recording systems. Although magnetic recording seems easy to reach the recording density area of around few 100 Gbit/in^2 at a glance, the progress speed has rapidly showed down since 2001. In order to further increase recording density, fabricating isolated magnetic dots in nanometer-size has been intensively examined. The situation is almost the same as that of near-field optical recording. Since electromagnetic fields leaked from a nano-magnetic dot are very weak, the future system does require nanotechnology to control nanoprecision errors in commercial production. As already mentioned in Chap. 4, a space control between the head and magnetic media in a few 10 s nanometers is an indispensable technology as well as near-field optical recording. Two big national projects to make breakthroughs in this technological issue have been organized in the United States, and in Japan. Also, in Europe, China, and Taiwan, the same sorts of high-density recording projects including Ohvonic memory have been carried out, combined with nanotechnology research. The US project is based on magnetic recording, in which the development of a 1=Tbit/in^2 hard disk system has been carried out with a help of a focused laser beam to easily reverse magnetic poles. This is called heat assisted magnetic recording. On the other hand, the Japanese project is rather focused and based on optical recording, where the fabrication of near-field apertures and the designing of the flying heads are the main objectives. Unfortunately, the project has gradually been oriented to the same recording system as that of the US project. This means that future optical discs will be non-removable and closed in a package with flying heads. Such optical disc system is no longer distinguishable with a hard disk drive. The originality of optical discs will be eliminated in future.

In contrast, it is thought that super-RENS technology will still take over the advantages of optical recording systems. As shown in Chap. 4, super-RENS technology has introduced several intriguing topics to near-field optical recording. In super-RENS, the advanced technologies are closed only in the media itself. An optical recording head is slightly modified from the current DVD or a Blu-ray one. Using a lens with NA < 0.85 and alternating the media structure from a rewritable-DVD disc, a 50-nm size mark or pit can be

reproduced with more than 40-dB CNR. The fact gives us an important suggestion that a function of the thin films consisting of super-RENS has a great role in super-resolution and near-field recording. However, as mentioned in Sect. 4.3.3, nobody has noticed the most important function hidden in optical phase-change films: chalcogenides! The first generation optical phase-change recording has only used the first phase-transition in between amorphous and crystal to store information bits. But, the future phase-change recording may adapt the second phase transition in between one crystal phase and another. At the moment, it is thought that ferroelectric catastrophe is the source to generate a huge refractive index change for super-resolution. But, don't forget that the catastrophe only occurs in tension. We think that Peierls transition causes the super-resolution. If such interesting physical phenomenon really happens in the disc, optical recording may lead to a new research era in physics and chemistry. The huge optical nonlinearities due to the ferroelectric catastrophe have not been applied to data storage so far. Almost all studies to estimate optical nonlinearities of materials have been done by pulsed laser beams under static conditions because of heat releasing. In optical recording, on the other hand, a thin film material in a multilayered stack is rotated at high speeds and the film is irradiated in high stress condition (compressive or tensile). For example, a typical phase-change film used in a rewritable-DVD reduces its volume more than 5%, which induces a very huge strain in the film: the protection films deposited up and down are oppositely irradiated in compressive stress, after crystallization from as-deposited condition. The study of materials under such ultimate conditions has barely been carried out, except in optical recording and earth sciences so far. We expect future research in super-RENS to open a new basic research field of dynamic optical nonlinear and chemical physics for detailed phase-transition.

In nanotechnology, on the other hand, a number of studies have been reported in fabricating nanoparticles and nanostructures up to now. The application to optical recording system still requires a long time, however. In Chap. 5, we would like readers to pay an attention to the importance of metallic nanoparticles and their interactions. Our research introduced in Chap. 5 is still basic. Controlling the size and space will become important factors to improve the light-scattering intensity and plasmon enhancement.

We believe that many young scientists and engineers should take part in this challenging research field to open a new physics and industrial world.

References

1. S.C. Esener, M.H. Kryder, W.D. Doyle, M. Keshner, M. Mansuripur and D.A. Thompson: WTEC Panel Report on "The Future of Data Storage Technologies," Jan. 1999
2. Optical Disc Storage Roadmap, National Storage Industry Consortium, Feb. 29, 2000
3. H. Nakajima and H. Ogawa: *Compact Disc* (Ohmsha, Tokyo 1996, in Japanese)
4. Y. Tsunoda (ed.): "The Principle and Application of Optical Data Storage," (Denshi-Joho-Tsuushinn-Gakkai, Tokyo 1995, in Japanese)
5. H.M. Liddle: *Computer-aided Techniques for the Design of Multilayer Filters* (AdHiger Ltd, Bristol 1981)
6. E. Hamada, Y. Takagishi, T. Yoshizawa, T. Fujii, R. Negishi, T. Nakajima: "Ten years overview and future prospects of write-once organic recordable media," *Jpn. J. Appl. Phys.* **39** 785 (2000)
7. Philips Consumer Electronics B. V.: Orange Book, Part II, Ver. 2.0, 1994
8. M. Mansuripur: "The physical principle of Magneto-optical Recording" (Cambridge Univ. Press, Cambridge 1995)
9. M. Okuda: *Materials for Rewritable Optical discs* (Kougyo-chyousa-kai, Tokyo 1989, in Japanese)
10. I. Duc: "Crystallization of amorphous chalcogenide thin films," Master's Degree Thesis (School of Industrial and manufacturing Science of Cranfield Univ., UK 1995)
11. N. Yamada, M. Otoba, K. Kawahara, N. Miyagawa, H. Ohta, N. Akahira, T. Matsunaga: "Phase-change optical disc having nitride interface layer," *Jpn. J. Appl. Phys* **37**, 2104 (1998)
12. T. Kikukawa: "Recent research and development of Ag-In-Sb-Te alloy for phase-change disc material," *Proceeding of the 13th symposium on Phase-change optical information storage* (PCOS2001, Yugawara, Japan 2001) p. 26
13. V. Gehanno, A. Fargeix, L. Poupinet, B. Hyot, A. Lagrange, O. Lartigue, B. Rolland, B. Bechevet: "High-density blue laser phase-change process analysis," *Proceeding of the 13th symposium on Phase-change optical information storage* (PCOS2001, Yugawara, Japan 2001) p. 1
14. M. Kaneko, K. Aratani, M. Ohta: "Multilayer magneto-optical disc for magnetically induced superresolution," *Jpn. J. Appl. Phys.* **31**, 568 (1992)
15. H. Awano, M. Sekine, M. Tani, N. Kasajima, N. Ohta, K. Mitani, N. Takagi, S. Sumi: "0.04 µm domain expansion readout for the magnetic amplifying magneto optical system," *Jpn. J. Appl. Phys.* **39**, 725 (2000)
16. T. Tokunaga, Y. Fujii, K. Yamada: "Domain expansion phenomena in exchange-coupled multilayer magneto-optical films," *Jpn. J. Appl. Phys.* **38**, 1621 (1999)

17. Y. Kasami, K. Yasuda, M. Ono, A. Fukumoto, M. Kaneko: "Premastered optical disc by superresolution using rear aperture detection," *Jpn. J. Appl. Phys* **35**, 423 (1996)
18. J. M. Vigoureux and D. Courjon: "Detection of nonradiative fields in light of the Heisenberg uncertainty principal and the Rayleigh criterion," *Appl. Opt* **31** 3170 (1992)
19. J. M. Vigoureux, F. Depasse and D. Courjon: "Sperresolution of near-field optical microscopy defined from properties of confined electromagnetic waves," *Appl. Opt* **31**, 3036 (1992)
20. J.W. Goodman: *Introduction to Fourier Optics*, MacGraw-Hill, New York 1968
21. H. Raether: *Surface Plasmons on Smooth and Rough Surface and on Grating*, Springer-Verlag, Heidelberg New York 1988
22. A. Taflove and S. Hagness: *Computational electrodynamics: The Finite-difference Time-domein Method*, Artech House, Boston 2000.
23. J. Judkins and R. Ziolkowski: "Finite-difference time-domain modeling nonperfectly conducting metallic thin film grating," *J. Opt. Soc. Am.* **A**, **12**, 1974 (1995)
24. T. Nakano, T. Gibo, L. Men, H. Fuji, J. Tominaga and N. Atoda: "Angular dependence of near-field scattering light from super-resolution near-field structure disk," *Proc. SPIE* **4085** 201 (2001)
25. T. Nakano, A. Sato, H. Fuji, J. Tominaga and N. Atoda: "Near-field optical simulation of super-resolution near-field structure disk," *Jpn. J. Appl. Phys.* **40**, 1531 (2001)
26. E. Betzig, J.K. Trautman, T.D. Harris, J.S. Weiner, R.L. Kostelak: "Breaking the diffraction barrier: optical microscopy on a nanometric scale," *Science* **251**, 1468 (1991)
27. E. Betzig, J.K. Trautman: "Near-field optics: Microscopy, spectroscopy, and surface modification beyond the diffraction limit," *Science* **257**, 189 (1992)
28. E. Betzig, J.K. Trautman, J.S. Weiner, T.D. Harris, R. Wolfe: "Polarization contrast in near-field scanning optical microscopy," *Appl. Opt.* **31**, 4563 (1992)
29. S. Hosaka, T. Shintani, M. Miyamoto, A. Hirotsune, M. Terao, M. Yasuda, K. Fujita, S. Kammer: "Scanning near-field optical microscope with a laser diode and nanometer-sized bit recording," *Thin Solid films* **273**, 122 (1996)
30. S. Hosaka, T. Shintani, M. Miyamoto, A. Hirotsune, M. Terao, M. Yasuda, K. Fujita, S. Kammer: "Nanometer-sized phase change recording using a scanning near-field optical microscopy with a laser diode," *Jpn. J. Appl. Phys.* **35**, 443 (1996)
31. K. Ito, T. Shintani, S. Hosaka, M. Muranishi: "A Cavity-SNOM(Scanning Near-field Optical Microscopy) Head Using a Laser Diode," *Jpn. J. Appl. Phys.* **37**, 3759 (1998)
32. F. Issiki, K. Ito, K. Etoh, S. Hosaka: "1.5-Mbit/s direct readout of line-and-space patterns using a scanning near-field optical microscopy probe slider with air-bearing control," *Appl. Phys. Lett.* **76**, 804 (2000)
33. M. Muranishi, K. Sato, S. Hosaka, A. Kikukawa, T. Shintani, K. Ito: "Control of Aperture Size of Optical Probe for Scanning Near-Field Optical Microscopy Using Forced Ion Beam Technology," *Jpn. J. Appl. Phys.* **7B**, L492 (1997)
34. M.B. Lee, N. Atoda, K. Tsutsui, M. Ohtsu: "Nanometric aperture arrays fabricated by wet and dry etching of silicon for near-field optical storage application," J. Vac. Sci. Technol. **B17**, 2462 (1999)

35. H. Yoshikawa, T. Ohkubo, K. Fukuzawa, L. Bouet, M. Yamamoto: "Readout characteristics of a near-field optical probe as a data-storage readout device: submicrometer scan height and resolution," *Appl. Opt.* **38**, 863 (1999)
36. M.B. Lee, M. Kourogi, T. Yatsui, K. Tsutsui, N. Atoda, M. Ohtsu: "Silicon planar-apertured probe array for high-density near-field optical strage," *Appl. Opt.,* **38**, 3566 (1999)
37. Y.J. Kim, K. Suzuki, K. Goto: "Parallel recording array head of nano-aperture flat-tip probes for high-density near-field optical data storage," *Jpn. J. Appl. Phys.* **37**, 2274 (1998)
38. A. Partovi, D. Peale, M. Wutting, C.A. Murray, Zydzik, L. Hopkins, K. Baldwin, W. S. Hbson, J. Wynn, J. Lapata, L. Dhar: "High-power laser light source for near-field optics and its application to high-density optical data storage," *Appl. Phys. Lett.* **75**, 1515 (1999)
39. T. Yatsui, M. Kourogi, K. Tsutsui, M. Ohtsu, J. Takahashi: "High-density-speed optical near-field recording- reading with a pyramidal silicon probe on a contact slider," *Opt. Lett.* **25**, 1279 (2000)
40. Y. Martin, S. Rishton, H.K. Wickramasinghe: "Optical data storage read out at 256 Gbits/in^2," *Appl. Phys. Lett.* **71**, 1 (1997)
41. T. Matsumoto, T. Shimano, S. Hosaka: "An Efficient probe with a planar metallic pattern for high-density near-field optical memory," *Conf. Program. of 6th International Conference on Near-field Optics and Related Techniques (NFO-6)*, (Twente, Netherlands 2000) p. 55
42. E. Oesterschultz, G. Georgiev, M. Mueller-Wiegand, A. Vollkopf, O. Rudow: "Transmission line probe based on a bow-tie antenna," *J. Microscopy* **202**, 39 (2000)
43. S.M. Mansfield, G.S. Kino: "Solid immersion microscope," *Appl. Phys. Lett.* **57**, 2615 (1990)
44. I. Ichimura, S. Hayshi, G.S. Kino: "High-density optical recording using a solid immersion lens," *Appl. Opt.* **36**, 4339 (1997)
45. W.H. Yeh, M. Mansuripur: "Evanescent coupling in magneto-optical and phase-change disc systems based on the solid immersion lens," *Appl. Opt.* **39**, 302 (2000)
46. G.S. Kino: "Fields associated with the solid immersion lens," *Proc. SPIE* **3467**, 128 (1998)
47. J. Guerra, D. Vezenov, L. Thuline, W. Haimberger, P. Sullivan, K. Nelson, E. Glytsis, T. Gaylord: "Embedded nano-optics media for near-field high density optical data storage: modeling, fabrication and performance," *Proc. SPIE* **4342**, 285 (2001)
48. B.D. Terris, H.J. Mamin, D. Ruger, W.R. Studenmund, G.S. Kino: "Near-field optical data storage using a solid immersion lens," *Appl. Phys. Lett.*, **65**, 388 (1994)
49. K. Kurihara, I. Nikolov, S. Mitsugi, K. Nanri, K. Goto: "Design and Fabrication of Microlens Array for Near-Field Vertical Cavity Surface Emitting Laser Parallel Optical Head," *Opt. Rev.* **10**, 89 (2003)
50. C.W. Lee et al: *Tech. Dig. Optical data Storage*, WA4, 137 (1998)
51. K. Ueyanagi, T. Tomono: "Proposal of a Near-Field Optical Head Using a New Solid Immersion Mirror," *Jpn. J. Appl. Phys.* **39** (2000)
52. H. Hatano, T. Sakata, K. Ogura, T. Hoshino, H. Ueda: "Plano-Convex solid Immersion Mirror with a Small Aperture for Near-field Optical Data Storage," *Opt. Rev.* **9**, 66 (2002)

53. K. Konno, M. Okitsu, K. Ogura, H. Hatano: "Design and evaluation of a Solid Immersion Mirror using a dielectric layer stack for near field optical recording," *Optics Japan 2003*, Enhanced Abst. p 124
54. T. Muzuno, K. Sako, T. Noshiro, H. Kato, N. Kojima, T. Hitosugi, S. Yamazaki, K. Watanabe: "An Optical Flying Head for a Near-Field Recording System: Part II," *Tech. Digest of Optical Data Storage 2002*, p 290
55. I. Ichimura, K. Kishima, K. Osato, K. Yamamoto, Y. Kuroda, K. Saito: "Near-Field Phase-Change Optical Recording of 1.36 Numerical Aperture," *Jpn. J. Appl. Phys.* **39**, 962 (2000)
56. I. Ichimura, K. Kishima, K. Saito, K. Yamamoto, Y. Kuroda, A. Iide, S. Masuhara, K. Osato: "Near-field optical recording on a pre-grooved phase-change disc in the blue-violet," *Jpn. J. Appl. Phys.* **40**, 1821 (2001)
57. J. Tominaga, T. Nakano, N. Atoda: "An approach for recording and readout beyond the diffraction limit with an Sb thin film," *Appl. Phys. Lett.* **73**, 2078 (1998)
58. J. Tominaga, H. Fuji, T. Nakano, T. Fukaya, N. Atoda: "Antimony aperture properties on super-resolution near-field structure using different protection layers," *Jpn. J. Appl. Phys.* **38**, 269 (1999)
59. J. Tominaga, T. Nakano, N. Atoda, H. Fuji, A. Sato: "The Characteristics and the Potential of Super Resolution Near-Field Structure," *Jpn. J. Appl. Phys.* **39**, 957 (2000)
60. J. H. Kim, D. Buechel, T. Nakano, J. Tominaga, N. Atoda, H. Fuji, Y. Yamakawa: "Magneto-optical disc properties enhanced by a nonmagnetic mask layer," *Appl. Phys. Lett.* **77**, 1774 (2000)
61. T. Fukaya, J. Tominaga, T. Nakano, N. Atoda: "Optical switching properties of a light-induced pinhole in antimony thin film," *Appl. Phys. Lett.* **75**, 3114 (1999)
62. J. Tominaga, T. Nakano, T. Fukaya, N. Atoda, H. Fuji, A. Sato: "The Near-Field Super-Resolution Properties of an Antimony Thin Film," *Jpn. J. Appl. Phys.* **37**, L1323 (1998)
63. Y. Kasami, K. Yasuda, M. Ono, A. Fukumoto, M. Kaneko: "Premastered disc by superresolution using rea apeture detection," *Jpn. J. Appl. Phys.* **35**, 423 (1996)
64. J. Tominaga, T. Kikukawa, M. Takahashi, T. Kato, T. Aoi: "Optical phase-chamhe disc without bulk laser initialization and a quick bulk initialization structure," *Jpn. J. Appl. Phys.* **36**, 3598 (1997)
65. L.P. Shi: "Investigation of a new structure of super-RENS phase-change optical disc," *Tech. Dig. Int. Super-RENS and Plasmon Sci. & Tech. Symp. 200*, Session 4, Oct. 22–23, 2001, Taipei, Taiwan
66. D.P. Tsai, C.W. Yang, W.C. Lin, F.H. Ho, H.J. Huang, M.Y. Chen, T.F. Teseng, C.H. Lee, C.J. Yeh: "Dynamic Aperture of Near-Field Super Resolution Structures," *Jpn. J. Appl. Phys.* **39**, 982 (2000)
67. Din Ping Tsai, W.C. Lin: "Probing the near fields of the super-resolution near-field optical structure," *Appl. Phys. Lett.* **77**, 1413 (2000)
68. U.C. Fischer, D.W. Pohl: "Observation of Single-Particle Plasmons by Near -Field Optical Microscopy*," Phys. Rev. Lett.* **62**, 458 (1989)
69. U.C. Fischer, M. Zapletal: "The concept of a coaxial tip as a probe for scanning near field optical microscopy and steps towards a realisation," *Ultra Microscopy* **42–44**, 393 (1992)

70. J. Tominaga, S. Haratani, K. Uchiyama, S. Takayama: "New recordable compact disc with inorganic material, AgOx," *Jpn. J. Appl. Phys.* **31**, 2757 (1992)
71. S. Haratani, J. Tominaga, H. Dohi, S. Takayama: "Property change of AgOx recordable compact disc with various dielectric films," *J. Appl. Phys.* **76**, 1297 (1994)
72. J. Tominaga, D. Buechel, T. Nakano, T. Fukaya, N. Atoda, H. Fuji: "Readout characteristics and mechanism of light-scattering-mode Super-RENS-discs," *Proc. SPIE* **4081**, 86 (2000)
73. H. Fuji, H. Katayama, J. Tominaga, L. Men, T. Nakano, N. Atoda: "A Near-Field Recording and Readout Technology Using a Metallic Probe in an Optical Disc," *Jpn. J. Appl. Phys.* **39**, 980 (2000)
74. T. Fukaya, D. Buechel, S. Shinbori, J. Tominaga, N. Atoda, D.P. Tsai, W.C. Lin: "Micro-optical nonlinearity of asilver oxide layer," *J. Appl. Phys.* **89**, 6139 (2001)
75. T. Kikukawa, T. Nakano, T. Shima, J. Tominaga: "Rigid bubble pit formation and huge signal enhancement in super-resolution near-field structure disc with platinum-oxide layer," *Appl. Phys. Lett.* **81**, 4697 (2002)
76. J.H. Kim, I. Hwang, D. Yoon, I. Park, D. Shin, T. Kikukawa, T. Shima, J. Tominaga: "Super-resolution by elliptical bubble formation with PtOx and AgInSbTe layers," *Appl. Phys. Lett.* **83**, 1701 (2003)
77. J. Tominaga, T. Shima, M. Kuwahara, T. Fukaya, A. Kolobov, T. Nakano: "Ferroelectric catastrophe: beyond nanometer-scale optical resolution," *Nanotechnology* **15**, 411 (2004)
78. J. Tominaga, J.H. Kim, D. Buechel, L. Men, H. Fukuda, T. Nakano, T. Fukaya, N. Atoda, H. Fuji, T. Kikukawa, A. Sato, A. Tachibana, Y. Yamakawa, M. Kumagai: "Super-Resolution Near-Field Structure and Signal Enhancement by Surface Plasmons," *Jpn. J. Appl. Phys.* **40**, 1831 (2001)
79. J. Tominaga: "Super-RENS and Plasmon Technology," *Tech. Dig. Int. Super-RENS and Plasmon Sci. & Tech. Symp. 2001, Session 1, Oct. 22–23, 2001*, Taipei, Taiwan.
80. J. Tominaga, J. H. Kim, D. Buechel, C. Mihalcea, T. Shima, T. Nakano, H. Fuji, T. Kikukawa, N. Atoda: "Optical diffraction and surface plasmons over small marks," *Tech. Dig. 3rd Asia Pacific Workshop on Near-field Optics*, Nov. 28–Dec.1, 2001, Melbourne, Australia
81. J. Tominaga, C. Mihalcea, D. Buechel, H. Fukuda, T. Nakano, N. Atoda, H. Fuji, T. Kikukawa: "Local plasmon photonic transistor," *Appl. Phys. Lett.* **78**, (2001) 2417 (2001)
82. J. Tominaga: "The application of silver oxide thin films to plasmon photonic devices," *J. Phys: Condens. Matter* **15**, R1101 (2003)

Index